Dymock, Ross Campbell (2014) *Developing the cosmogenic He chronometer*. MSc(R) thesis.

Developing the cosmogenic He chronometer

Ross Campbell Dymock
BSc (Hons)

Submitted in the fulfilment of the requirements for the Degree of MSc (R)

School of Science & Engineering
College of Geographical & Earth Sciences
University of Glasgow

February, 2014

Abstract

Helium isotopes have found wide use in geoscience research, notably as chronometers of surface exposure. This thesis comprises two distinct components around the theme of cosmogenic He determinations. In the first section (Chapter 3) I test whether cosmogenic ^{3}He can be used to determine short exposure times (<30 ka) in volcanic rocks that are significantly older than the exposure time (~60 Ma). Helium isotopes were measured in olivine, ilmenite and plagioclase from early Tertiary basalts from Isle of Skye, Scotland in order to determine exposure ages. Correction for radiogenic He was made with three different methods. The upper limit of exposure ages are variable, and slightly lower than previously determined by ^{36}Cl (Stone *et al.* 1998).

In the second part of the thesis I report characterisation of the new ThermoScientific HELIX-SFT mass spectrometer then compare performance against the existing MAP 215-50 instrument. The reproducibility of helium isotope determinations using the HELIX-SFT (~0.78%) is significantly better than the MAP 215-50, though not as good as reported elsewhere. The reasons for this are discussed and the potential for further improvements are highlighted.

Developing the cosmogenic He chronometer

Table of contents

- Abstract ii
- Table of contents iii
- List of tables vi
- List of figures vii
- Acknowledgements ix
- Dedication x
- Declaration xi

CHAPTER 1. Introduction

1.1 Overview 1

1.2 Research Aims and approach 1

1.3 Thesis Structure 2

CHAPTER 2. Cosmogenic isotopes; - origins, principles & applications

2.1 Introduction 4

2.2 Origin of cosmogenic radiation 4

2.3 The effect of the Earth's magnetic field and atmosphere 6

2.4 Production rates and scaling factors 8

- 2.4.1 *Physical principles* 8
- 2.4.2 *Irradiation experiments* 8
- 2.4.3 *Calibration with absolute dating techniques* 9
- 2.4.4 *Spallation* 10
- 2.4.5 *Thermal neutron capture* 11
- 2.4.6 *Negative muon capture* 11
- 2.4.7 *Scaling factors* 12

2.5 Helium in minerals 12

- 2.5.1 *Trapped helium* 13
- 2.5.2 *Radiogenic helium* 14
- 2.5.3 *Nucleogenic helium* 14

2.5.4 *Ejection distances and retentivity* 15
2.5.5 *Calculating cosmogenic ^{3}He* 16
2.6 Summary 17

CHAPTER 3. Determination of ^{3}He in Microphenocrysts of old basalts for unravelling 'Recent' Landscape Evolution.

3.1 Introduction 18
3.2 Determining cosmogenic He in old volcanic rocks 18
3.3 Devensian glaciation, Isle of Skye, Scotland: Investigating ice sheet thickness 19
3.4 Geological setting, sampling strategy and sample characterisation 23
3.5 Sample preparation 27
3.6 Analytical techniques 28
3.7 Results 28
3.7.1 Exposure ages calculated assuming radiogenic He only 29
3.7.2 Exposure ages calculated using ^{3}He/^{4}He of shielded sample 30
3.7.3 Exposure ages calculated with shielded sample ^{3}He concentration 31
3.8 Discussion 31
3.8.1 *Cosmogenic He ages* 31
3.8.2 *Comparison of cosmogenic ^{3}He and ^{36}Cl ages* 35
3.8.3 *Future* 42
3.9 Conclusions 43

CHAPTER 4. Noble Gas Mass Spectrometry: History, principles and applications

4.1 Introduction 44
4.2 Historical perspective 44
4.3 Principles of noble gas mass spectrometry 45
4.3.1 *Introduction* 45
4.3.2 *Electron bombardment ion sources* 46
4.3.3 *Mass separation using sector magnets* 47
4.3.4 *Ion detection* 48
4.4 Gas extraction and purification 49

CHAPTER 5. Initial characterisation of the ThermoScientific HELIX-SFT and comparison with Mass Analyser Products 215-50

5.1 Introduction 55

5.2 HELIX-SFT description 55

5.3 Characterisation of ThermoScientific HELIX-SFT 56

  5.3.1 *Peak shape and ion beam coincidence* 57

  5.3.2 *Isobaric interferences* 58

  5.3.3 *Determining optimum analysis parameters* 59

5.4 Performance comparison 61

  5.4.1 *MAP 215-50 description* 61

  5.4.2 *Analytical procedures* 63

5.5 Results 64

5.6 Discussion 65

5.7 Conclusions 66

CHAPTER 6. Concluding thoughts 67

APPENDICES

APPENDIX 1. Supplementary helium analysis data 68

APPENDIX 2. Petrographic descriptions 69

APPENDIX 3. Supplementary HESJ calibration data 74

REFERENCES 77

List of Tables

2.1 Cosmogenic nuclides and production pathways 10

3.1 Sample localities, Trotternish peninsula, Isle of Skye, UK 24

3.2 Helium isotope data from analysed samples 32-33

3.3 ^{36}Cl exposure age data from Stone *et al.* (1998) 36

3.4 ^{36}Cl ages recalculated from study of Stone *et al.* (1998). 38

3.5 ^{36}Cl ages recalculated with greatest production rates. 39

3.6 Helium contents (atoms) required to yield ages comparable to cosmogenic ^{36}Cl ages 41

5.1 Reproducibility and within-run uncertainty of ^{3}He/^{4}He measurements 64

List of Figures

2.1 Secondary cosmic particle cascade in the atmosphere 5

2.2 Energy spectrum of secondary cosmic particle neutrons at sea-level 6

2.3 Neutron flux at sea-level 7

2.4 Schematic representation of sources of helium within a mineral 13

3.1 Map of the Isle of Skye highlighting major summits and theoretical ice thickness 20

3.2 Schematic cross-section south-to-north along Trotternish peninsula 21

3.3 Schematic plot of ^{3}He and ^{36}Cl concentrations through time 22

3.4 Map of the Trotternish Peninsula, Isle of Skye, Scotland 23

3.5 Map of The Storr showing locations of exposed samples 25

3.6 Map of the Quiraing showing location of shielded sample 26

3.7 A. to E. Photographs of sample outcrops 27

3.8 Plot of cosmogenic ^{3}He exposure ages (calculated with radiogenic correction) against altitude 30

3.9 Cosmogenic ^{3}He exposure ages (calculated with shielded sample ^{3}He/^{4}He) against altitude 30

3.10 Cosmogenic ^{3}He exposure ages (calculated with shielded sample ^{3}He only) against altitude 31

3.11 Plot of ^{4}He concentration of all samples against ^{3}He/^{4}He 34

3.12 ^{3}He concentration of exposed samples in relation to average ^{3}He concentration of the shielded sample 35

3.13 Schematic of ^{36}Cl production pathways with depth below the surface 39

4.1 Simplified schematic of noble gas mass spectrometer 46

4.2 Schematic of Nier type ion source 47

4.3 Schematic of faraday collector 48

4.4 Schematics of A) discrete dynode and B) continuous dynode electron multipliers 49

4.5 Schematic of resistance furnace 51

4.6 Schematic of vacuum pumped laser cell 52

4.7 Schematic of turbo molecular pump 53

4.8 Schematic of an ion sputter pump 54

5.1 SUERC ThermoScientific HELIX-SFT mass spectrometer 55

5.2 Schematic of HELIX-SFT gas purification line 57

5.3 Scan showing peak shapes, separation of HD^+-H_3^+ from $^3He^+$ and coincidence of $^4He^+$ (blue) and $^3He^+$ (red) peaks. 58

5.4 Coincidence of $^{12}C^{3+}$ and $^4He^+$ ion beams on the Faraday detector over 10 minutes during static scan. 59

5.5 $^{12}C^{3+}$ background measured on the SEM after installation of GP50 getter on source block and deactivation of the ion gauge. 59

5.6 Plot of change in internal precision with time of integration. 60

5.7 Plot of change in internal precision with number of data cycles. 61

5.8 SUERC MAP 215-50 mass spectrometer 62

5.9 Schematic of MAP 215-50 gas purification line 62

5.10 Within-run uncertainty and reproducibility of $^3He/^4He$ (HESJ) measurements for both mass spectrometers. 65

Acknowledgments

This thesis represents more than the work carried out over the last eighteen months. It began life as a PhD study in October 2010 but only survived until April of the following year. The fact that it has now made it into print is in no small part due to the efforts of my supervisors Prof. Fin Stuart and Dr. Darren Mark. I would like to thank them both for their kindness, patience and support. They believed in me enough to give me a second chance, and for that I am eternally grateful.

I would also like to thank Fin for guiding me through the sometimes confusing world of cosmogenic helium, sharing his knowledge of noble gas mass spectrometry, his meticulous feedback and for helping me to develop my writing style. I would like to thank Darren for sharing his expertise in all things mass spec related, his feedback and good humour.

I would like to acknowledge the help of Jim Imlach in helping to prepare my samples for analysis, Dr. Dan Barfod for help with calculations and constructive discussions and Dr Luigia di Nicola for invaluable help with calculations.

Long days in the lab and the office have been made infinitely more bearable thanks to the good humour, support and strong cups of coffee provided by my compatriots in the SUERC post-grad room; Sevi, Pete, Tony, Louise, Brett, Domokos and Ana (the last two who I would also like to thank for their assistance during some *very* wet fieldwork!).

I would also like to thank my parents David and Carol; brother Alastair and all my grandparents. I am extremely fortunate to have a loving and supportive family and they all provided immense help through some dark times.

Finally, I would like to thank Diane Calgie whose understanding, guidance, support and efforts made it possible for me to be where I am today.

Dedication

I would like to dedicate this work to two men who throughout my life inspired my love of science and learning. Neither of them will get to see this work, but it is because of them that it has been written at all.

To my Grandfathers who have sadly passed away;

Nelson Dymock   Campbell Wilson

Thank you.

I declare that, except where explicit reference is made to the contribution of others, that this dissertation is the result of my own work and has not been submitted for any other degree at the University of Glasgow or any other institution.

Signature ______________________________

Printed name ______________________________

CHAPTER 1. Introduction

1.1 Overview

Terrestrial cosmogenic nuclide exposure dating techniques have advanced significantly in the last thirty years and are now routinely applied in Earth Sciences. They can be used to reconstruct Quaternary ice mass changes (e.g. Nishiizumi *et al.* 1991; McCarroll and Nesje 1993; Brook *et al.* 1995a; Ballantyne *et al.* 1998), dating of volcanic events (e.g. Cerling 1990; Kurz *et al.* 1990; Staudacher and Allégre 1993; Licciardi *et al.* 1999; Dunai 2001a; Farley *et al.* 2006) and surface uplift and erosion rates (e.g. Brook *et al.* 1995a; Williams *et al.* 2005). These methods can be applied to a wide range of geological settings and lithologies/mineralogies (quartz, plagioclase, pyroxene, olivine, amphibole, Fe-Ti-oxides amongst others). Of all the available techniques, cosmogenic ^{3}He is one of the more commonly used. It is a rare isotope of a rare element which makes it ideal for applications in Earth surface science. The majority of studies that utilise $^3He_{cos}$ focus on relatively young surfaces and rocks (<100 ka). This is due to the method of calculation of cosmogenic ages and their complication by several components of ^{3}He and ^{4}He within minerals.

1.2 Research aims & approach

This study has two main focuses. The first is to assess the applicability of cosmogenic ^{3}He exposure dating techniques to young surfaces in old volcanic rocks. The second is to characterise the ThermoScientific HELIX-SFT mass spectrometer and compare it with its predecessor the MAP 215-50.

For the first focus, the following questions were addressed:

- Is it possible to measure cosmogenic ^{3}He concentrations in microphenocrysts (olivine and ilmenite) of young surfaces in geologically old volcanic rocks?
- Do the data obtained provide further clarity on the contention of the existence of an englacial thermomechanical boundary within the Skye Ice Dome during the Devensian glaciation?

In order to answer these questions, precise and accurate ^{3}He concentration measurements from both exposed and shielded samples obtained from The Isle of Skye, Scotland were made. This involved sampling exposed basalt lavas from The Storr, Isle of Skye, Scotland, both above and below the altitude of the glacial/periglacial boundary (~540 – 550 m) (Ballantyne *et al.* 1998). Then shielded basalt lava samples from a quarry at the Quirang and a road-cut along the A855 route were obtained. All samples were analysed by laser fusion and analysed on the MAP 215-50 mass spectrometer at SUERC.

The second focus addressed the following questions:

- Are the levels of uncertainty for precision and accuracy of He gas analyses lower for the HELIX-SFT mass spectrometer than the MAP 215-50 mass spectrometer?
- Would the quality of the data from the analyses in the first study be improved if performed on the HELIX-SFT rather than the MAP 215-50?

The first question was answered by obtaining high quality He calibration data of gas analyses from both the MAP 215-50 and HELIX-SFT mass spectrometers. This involved construction of an UHV gas handling and purification line for the HELIX-SFT. Following initial installation and set-up, several experiments were carried out in order to characterise the performance of the instrument. Optimal running parameters were determined and then analyses of calibration He gas HESJ (Matsuda *et al.* 2002) were carried out. Identical analyses were performed on the pre-existing MAP 215-50 mass spectrometer (Stuart *et al.* 1995). The data obtained from each dataset were compared and levels of uncertainty in precision and accuracy used to gauge relative performance.

The second question is answered by comparing the size of the uncertainties obtained from analyses. All samples analysed were ~100 – 200 mg and were exposed for ~3.5 – 20.5 ka. This equates to ~0.4 – 2.4 x 10^6 a g^{-1} of $^3He_{cos}$ within each sample. The analytical uncertainties associated with these gas amounts were compared between the MAP 215-50 and HELIX-SFT in order to assess whether uncertainties would be decreased if analysed on the latter.

1.3 Thesis structure

This thesis is divided into six chapters

Chapter 2 introduces terrestrial cosmogenic nuclide (TCN) production. It reviews current practices in cosmogenic He exposure dating and summarises the constraints on expanding the technique to geologically old environments.

Chapter 3 gives a brief overview of the geology and glacial history of the Isle of Skye with emphasis on the ice mass extent during the Devensian glaciation. I present new cosmogenic He data from samples from The Storr and review implications for the ice masses extent as well as assessing the suitability of cosmogenic He for determining exposure duration in old volcanic rocks.

In chapter 4, I review noble gas mass spectrometry with emphasis on up-to-date practices.

Chapter 5 presents characterisation of performance of the HELIX-SFT and the results of a comparative study with the MAP 215-50 mass spectrometer.

In chapter 6, I synthesise both studies and address the potential of the HELIX SFT to provide cosmogenic He data with greater precision and accuracy than the MAP 215-50.

CHAPTER 2. Cosmogenic isotopes; - Origins, principles & applications

2.1 Introduction

The use of terrestrial cosmogenic nuclides (TCN) is a powerful geochronological technique for Earth. In this study I attempt to use cosmogenic ^{3}He to determine relatively short exposure duration of early Tertiary (~60 Ma) volcanic rocks.

This chapter gives an overview of the production and use of *in-situ* TCN focussing on ^{3}He. It begins by exploring the origin of the cosmic ray flux and the resulting secondary cosmogenic particle cascade on Earth. The effects of the Earth's atmosphere and magnetic field on cosmogenic particles are explained, then followed by descriptions of how scaling factors account for these effects and the implications for determining production rates. Finally I review the different sources of helium in minerals with emphasis on how to distinguish cosmogenic He in old minerals.

2.2 Origin of cosmic radiation

The existence of radiation penetrating the Earth's atmosphere from space was first proposed by CTR Wilson in 1905 (Blackett 1960). Initial experiments carried out by Victor Hess (Hess 1912) using gold-foil electrometers indicated a rapid increase in ionization with altitude. Studies performed throughout the 1930s to late 1950s led to the discovery of subatomic particles and laid the foundations for the understanding of this radiation for the use in Earth surface science (Grosse 1934; Libby *et al.* 1949; Davis and Schaffer 1955; Powell *et al.* 1959).

Cosmic rays are high-energy, charged particles that impact the Earth from all directions. The bulk of these are protons, but they also include electrons, positrons and other subatomic particles (Masarik and Reedy 1995). Current understanding is that cosmic ray particles obtain their energy from supernova explosions that occur roughly once every 50 years in our Galaxy (Diehl *et al.* 2006). Cosmic ray particles with a range of energies from 100 MeV to 10 GeV, are located within our Galaxy (Eidelman *et al.* 2004) and the mean cosmic-ray energy spectrum and integrated flux are believed to have remained constant over the last 10 Ma (Leya *et al.* 2000). A cosmic ray particle with sufficient energy to penetrate the Earth's magnetic field collides with particles in the upper atmosphere, generating an intricate cascade of nuclear interactions that propagate through the atmosphere. The secondary particles collide with nuclei creating three components; nucleonic, mesonic and electromagnetic (Lal and Peters 1967). The nucleonic component dominates the cosmogenic nuclide production at Earth's surface and the mesonic component dominates production at depth in the subsurface. The electromagnetic component has little to no relevance with regards to Earth surface science applications (Lal and Peters 1967). The primary reaction that takes place within the atmosphere is spallation. It causes neutrons to be sputtered off the impacted nucleus whilst mostly retaining the direction of the impacting particle. These sputtered neutrons then go on to cause further spallation reactions in other nuclei, inducing the nuclear cascade (Figure 2.1).

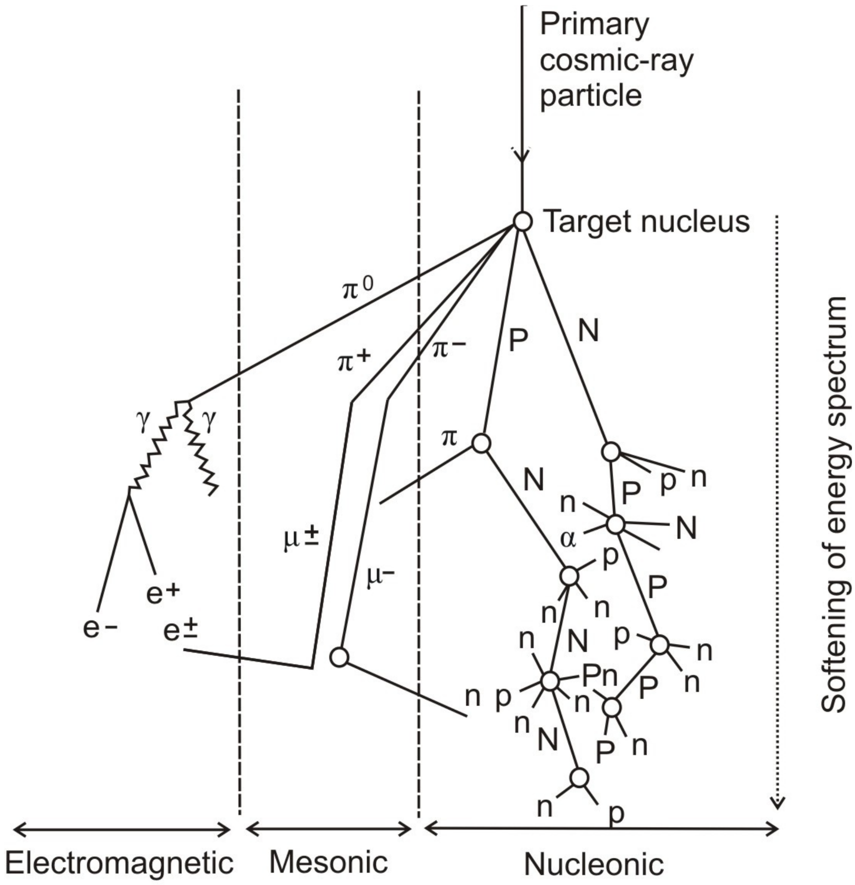

Figure 2.1 Secondary cosmic particle cascade in the atmosphere. Key, n = neutron, p = proton (Capital letters indicate particles carrying on the nuclear cascade), α = alpha particle, $e^{\pm}$ = electron or positron, γ = gamma-ray photon, π = pion, μ = muon. Modified from Allkofer and Grieder (1984).

As neutrons do not suffer ionization loss (unlike protons) they dominate the cascade. At sea-level neutrons account for ~98% of the cosmic-particle flux (Masarik and Beer 2009). There is a concomitant decrease in energy of the particle flux. At sea-level, the energy spectrum of the nucleonic component has 3 peaks, these occur at 100 MeV, 1 – 10 MeV and <1 MeV (Figure 2.2).

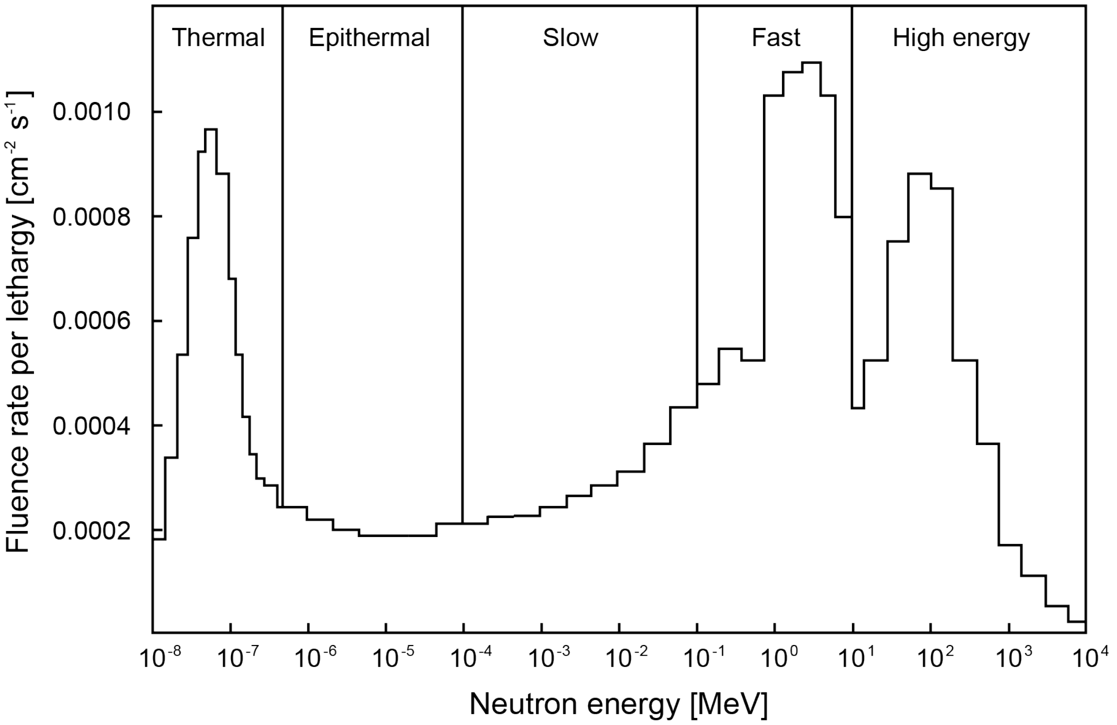

Figure 2.2. Energy spectrum of secondary cosmic particle neutrons at sea level. Lethargy is the natural logarithm of energy. After Goldhagen *et al.* (2002.)

2.3 The effect of the Earth's magnetic field & atmosphere

The charged primary cosmic ray protons are subject to the effects of magnetic and electrical fields of the Sun and the Earth. The electrical fields accelerate or decelerate the particles in the direction of the field. The Lorentz force in a magnetic field accelerates charged particles radially which in turn causes them to curve perpendicularly to both their initial incidence path and the direction of the magnetic field. The deflecting force increases as the angle between the incidence path and direction of the magnetic field increases. The slower the incident particle is moving the larger the deflecting force (Smart *et al.* 2000).

The flux of primary incident particles with energies below 10 GeV are subjected to modulation by the solar wind and the Sun's 11-year 'sunspot' cycle (Lal and Peters 1967; Eidelman *et al.* 2004). If this modulation cause's the particles energy to drop below 0.6 GeV then it does not penetrate the Earth's magnetic field. This phenomenon, known as 'cut-off rigidity', describes the momentum per unit charge of a particle (Michel et al. 1996; Masarik and Beer 2009; Usoskin et al. 2005; Wiedenbeck et al. 2005). Particles with near-vertical incident trajectories dominate the cosmic-ray flux near the Earth's surface, however; there is an imbalance in the flux due to the dipole characteristics of the Earth's magnetic field. At the equator incident particles travel perpendicular to the field and require cut-off rigidities in excess of 10 GeV to reach the Earth's surface (Dorman *et al.* 1999). At the poles the particles travel parallel to the field and almost all protons are able to reach the surface.

Solar modulation means that protons require >0.6 GeV to penetrate the magnetic field (Dorman *et al.* 1999). Solar modulation also results in non-uniform flux from the equator to the poles and results in a latitude 'knee', where the change in flux is greatest (Dunai 2000) (Figure 2.3). The particles that penetrate the field are at a maximum flux towards the geomagnetic poles and at a minimum flux at the geomagnetic equator. The 'knee' lies approximately at 60° magnetic latitude (Dunai 2000). Additionally, particles that impact the geomagnetic field with energies close to the solar modulation threshold do not create a secondary particle cascade.

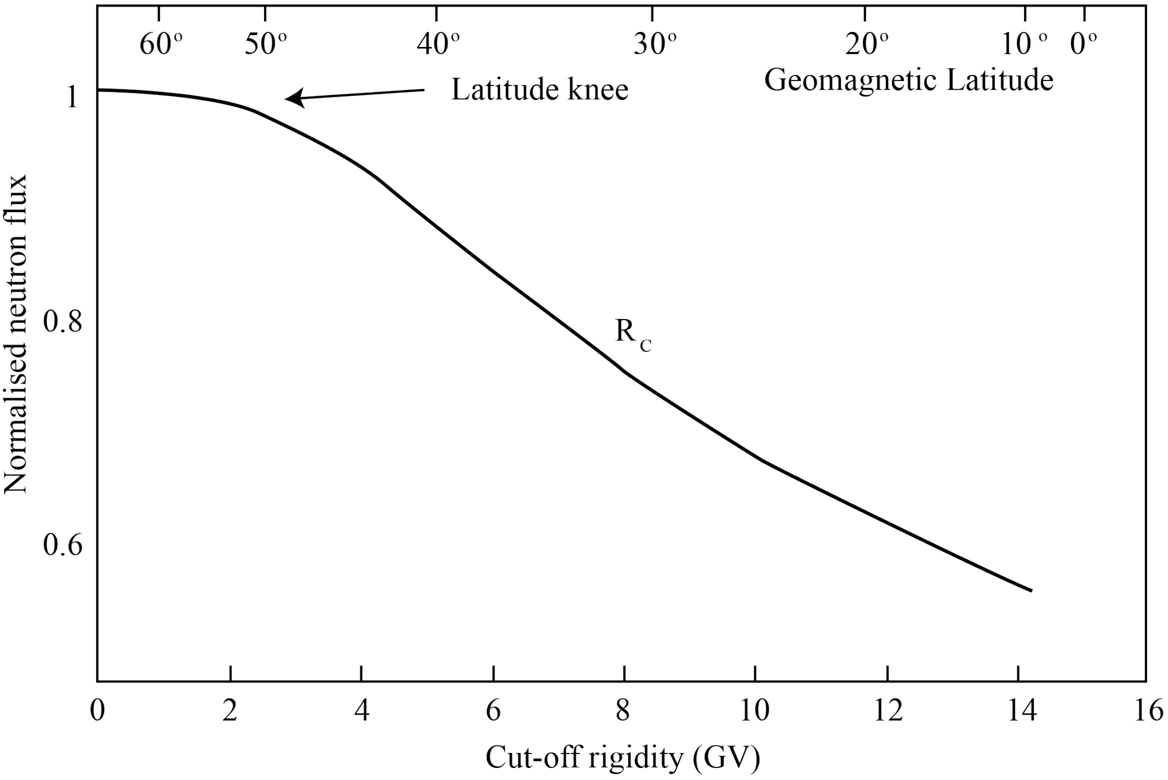

Figure 2.3. The neutron flux at sea-level varies as a function of cut-off rigidity. R_c represents the flux in a dominant dipole field (>70%) as derived by Dunai (2000, 2001). The cut-off rigidity is related to geomagnetic latitude calculated for modern day field strength and should be used as a rough guide only.

It is possible, therefore, to calculate the cosmic ray flux at points on the Earth for both dipole and non-dipole elements of the field (Dunai 2001; Lal 1991; Lifton *et al.* 2005). The main emphasis is on dipole elements as >70% of the field takes this form, non-dipole regions account for ~15%.

The flux of muons that have energies greater than 0.3 GeV are not as sensitive to electromagnetic fields and the flux varies by less than 10% from the equator to the poles. Muons with energies greater than 20 GeV are not affected by Earth's magnetic field (Stone *et al.* 1998).

The secondary particles within the nuclear cascade are subject to attenuation via spallation collisions with nuclei in the atmosphere. The neutron energy within the cascade halves every 1500 m; this is known as the attenuation length. It varies due to geomagnetic latitude, cut-off rigidity and altitude (Lal 1991; Dunai 2001). Muon attenuation follows the same behaviour but have longer lengths due to their increased energies. Despite the attenuation effects some secondary radiation reaches and penetrates the upper few metres of the Earth's surface (Lal and Peters 1967).

Consequently TCN production rate at the Earth's surface varies as a function of both latitude and altitude

2.4 Production rates and scaling factors

Accurate TCN production rates are essential for calculating exposure ages and/or erosion rates. Scaling factors are the mathematical description of how production rates vary with the latitude and altitude. Production rates have been derived in three different ways; (1) physical principles (e.g. Masarik and Reedy 1994), (2) irradiation experiments (e.g. Leya *et al.* 1998) and (3) calibration with absolute dating techniques (e.g. Kurz *et al.* 1990).

2.4.1 Physical principles

Numerical simulations of cosmic ray flux and reaction cross-section data can be used to model the cosmic ray flux in the atmosphere and its interaction with the Earth's surface (Masarik & Reedy 1994; 1995; and 1996; Masarik & Beer 2009). However approximations that were required to complete the simulations have uncertainties of ~25%. Therefore application of this method to *in situ* applications is limited.

2.4.2 *Irradiation experiments*

Pure elements or compounds can be irradiated by artificial muon, neutron or proton beams or by environmental cosmic rays. Experiments carried out by Leya *et al.* (1998), Heisinger *et al.* (2002a), Heisinger *et al.* (2002b), Sisteron (2005) and Nishiizumi *et al.* (2009) allows for detailed descriptions of how production rates vary with altitude and latitude (Brown *et al.* 2000; Vermeesch *et al.* 2008). Data from Muon-beam experiments are currently the most widely used to determine the contribution from muons on cosmogenic production rates (Heisinger *et al.* 2002a; Heisinger *et al.* 2002b). The key issue in using irradiation experiments in order to derive cosmogenic nuclide production rates is that they are performed over very short timescales. Due to modulation of the cosmic ray flux by solar activity over an 11 year period estimations have to be made in order to derive a long-term production rate that is applicable to geological samples (Nishiizumi *et al.* 2009).

2.4.3 C*alibration with absolute dating techniques*

The most commonly applied method of calculating TCN production rates is provided by determining nuclide concentrations in natural surfaces of known age. This requires surfaces that have suffered no significant erosion, prior exposure and/or intermittent burial (Niedermann 2002). Independent ages are obtained by a number of methods depending on the nature of the surface. These include radiocarbon (Kurz *et al.* 1990; Cerling and Craig 1994a; Kubik *et al.* 1998; Licciardi *et al.* 1999; Licciardi *et al.* 2006), Ar/Ar dating (Dunai and Wijbrans 2000), dendrochronology and varve chronology (Balco and Schaefer 2006).

In the case of cosmogenic radionuclides it is necessary to correct the data for decay. However, if samples reach saturation, the decay rate of the nuclide is identical to that of the accumulation rate; therefore the production rate can be relatively simple to calculate (Nishiizumi *et al.* 1989; Jull *et al.* 1992; Brook *et al.* 1995b; Lifton 2008). Local production rates are normalised to sea-level and high-latitude (SLHL) and are consequently dependent on scaling factors.

TCN are produced at the Earth's surface by secondary particles, primarily neutrons with subordinate production from muons. The neutron flux has energy peaks for spallation, thermal neutron capture and negative muon capture. The probability of the type of reaction taking place depends on the energy of the incident particle and the reaction cross-section (Masarik and Reedy 1994; Reedy and Masarik 1994; Heisinger *et al.* 2002a; Heisinger *et al.* 2002b). Spallation is the most important reaction for production of TCN (Lal and Peters 1967). Relevant cosmogenic nuclides and their production reactions are shown in Table 2.1.

Isotope	Primary spallation reactions	Thermal neutron capture	Negative muon capture
^{3}He ^{3}H(β-^{3}He)	On all elements heavier than H, reactions of the type; (n, x^{3}He) or (n, x^{3}H) with x being any other particle or none	^{6}Li(n,α)^{3}H(β-^{3}He)	On all elements heavier than H; reactions of the type; (μ-,^{3}He) or (μ-, ^{3}H).
^{10}Be	^{16}O(n, ^{3}Heα)^{10}Be or ^{16}O(n, ^{4}p3n)^{10}Be ^{28}Si(n, x)^{10}Be	^{9}Be(n, γ)^{10}Be	^{16}O(μ-, αpn)^{10}Be ^{28}Si(μ-, x)^{10}Be
^{14}C	^{16}O(n, 2pn)^{14}C ^{28}Si(n, x)^{14}C	^{17}O(n, α)^{14}C ^{14}N(n, p)^{14}C	^{16}O(μ-, pn)^{14}C
^{21}Ne	^{23}Na(n, ^{3}H)^{21}Ne ^{24}Mg(n, α)^{21}Ne ^{27}Al(n, α^{3}H)^{21}Ne ^{28}Si(n, 2α)^{21}Ne		^{23}Na(μ-, 2n)^{21}Ne ^{24}Mg(μ-, ^{3}H)^{21}Ne ^{27}Al(μ-, α2n)^{21}Ne
^{22}Ne	^{23}Na(n, pn)^{22}Ne ^{25}Mg(n, α)^{22}Ne ^{27}Al(n, αpn)^{22}Ne ^{29}Si(n, 2α)^{22}Ne		^{23}Na(μ-, n)^{22}Ne ^{24}Mg(μ-, pn)^{22}Ne ^{27}Al(μ-, αn)^{22}Ne
^{26}Al	^{28}Si(n, 2np)^{26}Al		^{28}Si(μ-, 2n)^{26}Al
^{36}Cl	^{39}K(n, α)^{36}Cl ^{40}Ca(n, αn)^{36}Cl	^{35}Cl(n, γ)^{36}Cl ^{39}K(n, α)^{36}Cl	^{39}K(μ-, ^{3}H)^{36}Cl ^{40}Ca(μ-, α)^{36}Cl
^{53}Mn	^{54}Fe(n, pn)^{53}Mn ^{56}Fe(n, 3np)^{53}Mn		^{54}Fe(μ-, n)^{53}Mn

Table 2.1. Cosmogenic nuclides and production pathways

2.4.4 *Spallation*

Impacts of high-energy neutrons fragment atomic nuclei into lighter nuclei and a few neutrons and protons (Masarik and Beer 2009). Target elements that have masses closest to the cosmogenic nuclide being produced contribute the most. This sputtering of neutrons creates an intranuclear cascade in which a series of independent nucleon-nucleon collisions occur (Serber 1947; Filges *et al.* 2001). Depending on the manner of collision three reactions may occur. If the impact is peripheral, the nuclei may release several neutrons that will retain much of the impactor's energy. This will allow the cascade to continue. A central impact will distribute the impactor's energy across the nuclei and if this energy is ~7-9 MeV, then a sub-sequent de-excitation reaction will take place producing further neutrons (Serber 1947; Masarik and Beer 2009). The third possibility also depends on a central impact and involves the emission of an α-particle as well as a neutron, (n, α). This is due to the large binding energy of α-particles (28.3 MeV) that often prevents them from being retained within the nucleus.

2.4.5 *Thermal neutron capture*

Approximately 98% of neutrons in the nuclear cascade occur in the thermal energy range; these thermal neutrons can cause the same reactions as the cosmogenic thermal neutrons (CTN) (Phillips *et al.* 2001). These are neutrons that have had their energy levels moderated by inelastic collisions with nuclides in the atmosphere and rocks (Dunai *et al.* 2007). Thermal neutrons are not exclusive to the atmospheric nuclear cascade and are also produced in the subsurface by (α, n) reactions (Andrews and Kay 1982). The shallow sub-surface CTN production outweighs the (α, n) component. However the production of stable cosmogenic nuclides, such as ^{3}He, the (α, n) produced thermal neutrons can be significant when exposure dating old rocks (>50 – 100 ka) (Farley *et al.* 2006; Dunai *et al.* 2007).

2.4.6 *Negative muon capture*

Muons interact weakly with matter; consequently they are able to penetrate further into the subsurface. The penetration depth depends on the muon energy on entering the subsurface (Lal 1988). Cross-sections for negative muon capture reactions are much smaller than those for neutrons, therefore the contributions to TCN production is low compared to spallation (Table 2.1). A minor proportion of the TCN produced at earth's surface are produced via negative muon capture. For the mean energy at earth's surface the muogenic contribution reaches a peak at 8m where it dominates the cosmogenic production (Eidelman *et al.* 2004). Calculated production rates for muons account for approximately 2% of ^{10}Be, 2.1% of ^{26}Al and 10% of ^{14}C (SLHL) (Heisinger *et al.* 2002a).

2.4.7 *Scaling factors*

Several scaling factor schemes have been proposed which take into account various sources of uncertainty (Lal 1991; Stone 2000; Dunai 2000; Desilets and Zreda 2003; Lifton *et al.* 2005; Lifton *et al.* 2008; Desilets *et al.* 2006).

The most frequently used scaling model is that of Lal (1991). It is termed on a third-degree polynomial function which in itself is scaled to the nuclear disintegration curves of Lal and Peters (1967). It accounts for differences in geomagnetic latitude and altitude. It does not account for any effects of non-dipole magnetic fields or variations in the atmospheric structure.

Stone (2000) was the first to give an in-depth consideration to the effects of atmospheric scaling. Up to this point all scaling models utilised the Standard Atmosphere model which is used to approximate mean annual conditions at mid-latitudes. It cannot represent extremes in the global atmospheric pressure. Stone (2000) introduced altitude dependant scaling factors that account for regional differences in mean annual pressure in areas of persistent high or low pressure.

Dunai (2000) introduced a model which takes into account the non-dipole component of the magnetic field. This is most important when considering low-latitude sites. Desilets and Zreda (2003) considered thermal neutron and spallation reactions and the differing energies and attenuation lengths involved. They also considered the effects of temporal and spatial changes in the atmospheric structure on mass shielding depth. Lifton *et al.* (2005; 2008) concentrated on the variations in the magnetic field and solar modulation and their effects on the cosmic-ray flux.

2.5 Helium in minerals

Cosmogenic ^{3}He (^{3}He$_{cos}$) is predominantly produced by spallation reactions at the earth's surface and can be produced on all elements present within a mineral, with the exception of hydrogen. Production rates for ^{3}He in silicates is of the order 100-120 atoms g^{-1} a^{-1} (SLHL) (Dunai 2001a; Farley *et al.* 2006; Licciardi *et al.* 1999; Licciardi *et al.* 2006; Cerling and Craig 1994a; Goehring *et al.* 2010; Blard *et al.* 2005; Balco *et al.* 2008; and Dunai and Wijbrans 2000) and 63-78 atoms g^{-1} a^{-1} (SLHL) for Fe-Ti-oxides (Bryce & Farley 2002; Margerison *et al.* 2005; and Masarik 2002).

Cosmogenic He is produced with a $^{3}He/^{4}He$ of 0.2 – 0.3 (Wieler 2002). This is enriched in ^{3}He by 10^{4} – 10^{7} times compared to terrestrial He (mantle, crust and air) and forms the basis for the resolution of $^{3}He_{cos}$ from any potential interference from terrestrial components. Consequently cosmogenic helium is ideal for use as a tool in Earth science. Almost all cosmogenic helium studies are carried out on minerals obtained from volcanic rocks as they contain the majority of minerals which are able to quantitatively retain He.

There are several other sources of He that may be present within a mineral (Figure 2.4). Quantifying $^{3}He_{cos}$ requires knowledge of these so that they are accurately accounted for.

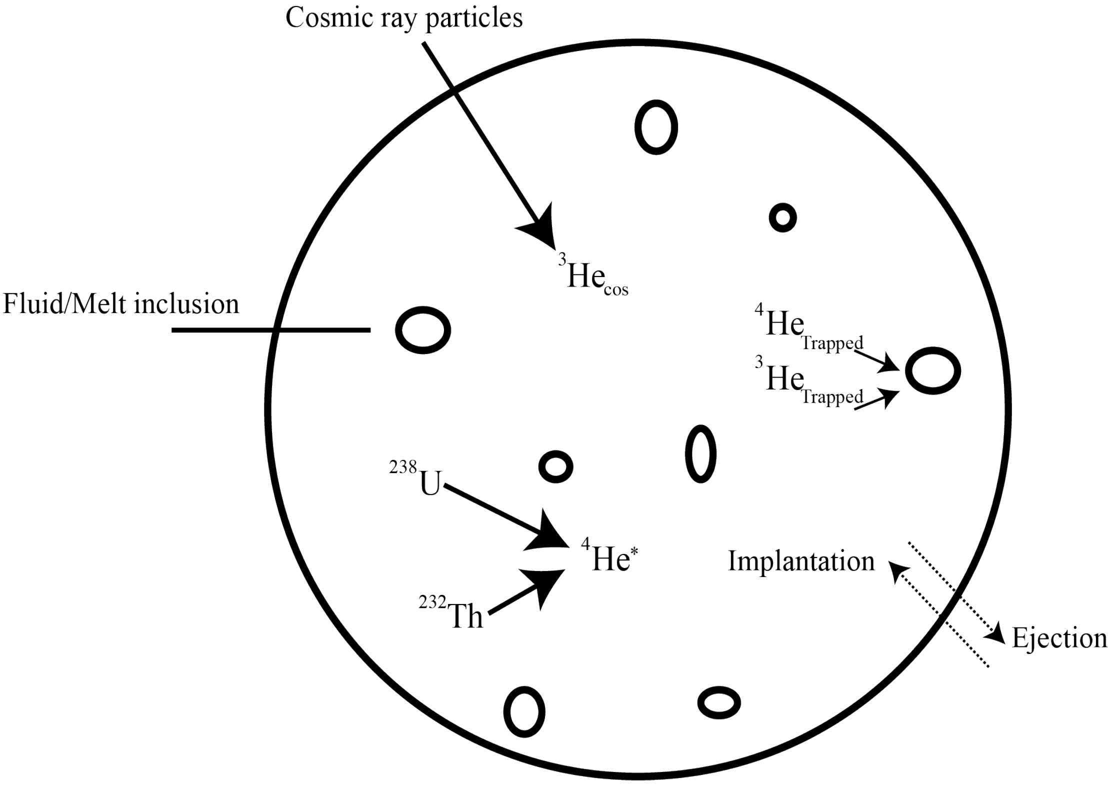

Figure 2.4. Schematic representation of sources of helium within a mineral which has been exposed to cosmic ray particles. $^{3}He_{cos}$ = cosmogenic 3 helium, $^{4}He^{*}$ = radiogenic 4 helium. See text for explanation. Nucleogenic production of ^{3}He has not been shown.

2.5.1 *Trapped helium*

Helium from the mantle, crust or atmosphere that resides in the crystal lattice or in fluid or melt inclusions is referred to as “trapped”. It may originate from gas present within the mantle upon crystallization (magmatic), from air or water during eruption or from fluid interaction during metamorphism (Niedermann 2002).

2.5.2 *Radiogenic helium*

Radiogenic He ($^4He^*$) is produced by the *in situ* decay of U and Th (Andrews 1985). U and Th concentrations in basaltic olivine, pyroxene and Fe-Ti-oxides are typically low enough that $^4He^*$ production can be considered negligible (Dunai and Wijbrans 2000). However, contribution from surrounding U- or Th- rich phases can be important in cases of intermediate to felsic rocks (Dunai and Wijbrans 2000). Ignoring $^4He^*$ leads to an underestimation of the $^3He_{cos}$ concentration, by overestimating the magmatic ^4He and therefore magmatic ^3He (Blard and Farley 2008). In cases when contribution is significant a correction factor must be applied. This is done by calculating the production rate of $^4He^*$ (P_4) using the method of Blard and Farley (2008):

$$P_4 = I_4 \times [1 - 1.5 \times (S/D) + 0.5 \times (S/D)^3] + M_4 \times [1.5 \times (S/D) - 0.5 \times (S/D)^3] \qquad (2.1)$$

where, I_4 is the *in situ* $^4He^*$ production rate (at g^{-1} a^{-1}) in the phenocryst, M_4 is the $^4He^*$ production rate (at. g^{-1} a^{-1}) in the surrounding groundmass, S (µm) is the α-particle stopping distance, and D (µm) is the diameter of the phenocryst, this assumes a spherical geometry. Implanted $^4He^*$ can be reduced by chemically etching or physically abrading the outer ~20 µm of the mineral phenocrysts so that implantation of $^4He^*$ can be assumed to be zero. Therefore all $^4He^*$ is due to *in situ* production (Min *et al.* 2006; Aciego *et al.* 2007; Blackburn *et al.* 2007; Gayer *et al.* 2008; and Ammon *et al.* 2009).

2.5.3 *Nucleogenic helium*

Nucleogenic production of ^3He ($^3He_{nuc}$) comes from interactions of thermalized neutrons with ^6Li. There are two sources of thermalized neutrons; those produced by (α, n) reactions within the rock and those from the cosmic ray cascade (Dunai *et al.* 2007). Traditionally thermalized cosmogenic neutrons were not considered. The thermal neutron flux produced by (α, n) reactions in the rock are a result of U- and Th-decay which induce reactions in lighter elements, and to a lesser degree spontaneous fission of ^{238}U. These neutrons dissipate their energy by scattering until they reach thermal equilibrium. The effectiveness of this process, and therefore, thermal neutron flux are strongly dependant on rock chemistry (Dunai *et al.* 2007).

It has been discovered however that the contribution of thermal neutrons from the cosmic ray cascade can be 10-200 times higher than the thermal neutron flux produced by (α, n) reactions in the rock matrix, although the exact values depend on chemistry and geographic location (Dunai *et al.* 2007). The thermal neutron capture reaction: (^{6}Li(n, α)^{3}H(β)^{3}He) can be responsible for between 5-50% of ^{3}He$_{cos}$ production in minerals that have ^{6}Li >5 ppm. In some cases however depending on the Li content and distribution and petrography of the rock it can vary between ≈0 to ≈100%. However in basaltic lavas, such as those used in this study, the contribution of this reaction is much lower (1.5-6%) (Dunai *et al.* 2007). Most cosmogenic helium studies disregard the ^{3}He$_{nuc}$ component where rock ages are <100 ka (Farley *et al.* 2006). However, if the cosmogenic neutron flux is less than or equal to 200 times the (α, n) neutron flux then any rock which has a rock age greater than 200 times the exposure age (such as those used in this study), the contribution from thermal neutrons will be more significant than from cosmogenic thermal neutrons.

Within basalts the majority of Li is located within the matrix with an abundance of ~5 ppm, at SLHL this equates to ~1.5 atoms g^{-1} a^{-1}. The ^{3}H nucleus is ejected with energy of 2.7 MeV which equates to a distance of ~30 μm (Dunai *et al.* 2007). This would not be hugely significant as ^{3}He$_{cos}$ is typically analysed in phenocrysts of olivine and pyroxene. In this study, however, grains of 75-125 μm are used and therefore implantation of ^{3}He$_{nuc}$ may be important. As this is the case either the component must be corrected or quantified. Therefore if Li content is significant (>5 ppm) or if the target minerals grainsize is comparable to the ejection distance of ^{3}He$_{nuc}$ then its production can be significant (Lal 1987; Dunai *et al.* 2007).

2.5.4 *Ejection distances and retentivity*

The retentivity of helium in minerals varies greatly because of its inability to engage in chemical bonds in the natural environment. Because of this, it can diffuse relatively easily via structural channels or defects within a crystal (Trull *et al.* 1991; McDougall and Harrison 1999; and Farley 2007). However at Earth-surface conditions, many minerals have been shown to quantitatively retain helium; olivine (Trull *et al.* 1991), and pyroxene (Lippolt and Weigel 1988) being among them.

The ejection distances of radiogenic ^{4}He (11-34 μm), nucleogenic ^{3}He (~30 μm) and cosmogenic ^{3}He can affect distribution in minerals (Dunai and Wijbrans 2000; Farley *et al.* 2006; Dunai *et al* 2007; and Blard and Farley 2008). This is most apparent in grains with dimensions similar to the ejection distances (Farley *et al.* 1996; Farley *et al.* 2006) and the rims of larger crystals (Dunai and Wijbrans 2000; Dunai *et al.* 2007). Cosmogenic ^{3}He and ^{3}H have no strict upper energy limit. In olivine (Fo$_{80}$), at median energies for ^{3}He$_{cos}$ and ^{3}H the ejection distances range from 54 – 170 μm and 70 – 200 μm, respectively (Ziegler *et al.* 2008). As ejection distances are similar to the mineral grain sizes utilised in this study, a significant amount of the ^{3}He measured may have been implanted. Similarly ^{3}He or ^{3}H produced in the mineral may come to rest in the surrounding host rock (Farley *et al.* 2006). Gains by implantation and losses due to ejection are difficult to quantify due to a limited knowledge of the energy spectrum of particles emitted and of the spallogenic production ^{3}H/^{3}He ratio (Masarik 2002; Kober *et al.* 2005). If the difference in production rates between host rock and mineral grains are small then the relative effects on apparent mineral production rates will also be small (Farley *et al.* 2006).

2.5.5 *Calculating cosmogenic ^{3}He*

It is necessary to discriminate between trapped ^{3}He and cosmogenic ^{3}He. Trapped ^{3}He is contained within fluid– and melt-inclusions and cosmogenic ^{3}He is produced within the mineral lattice. To distinguish the different components, two stages of gas extraction are typically undertaken. *In vacuo* crushing extracts the magmatic helium from melt/fluid inclusions. The resulting powder is then melted and the ^{3}He$_{cos}$ concentration calculated using;

$$^3\mathrm{He}_{cos} = (^3\mathrm{He}/^4\mathrm{He}_{melt} - {}^3\mathrm{He}/^4\mathrm{He}_{crush}) * {}^4\mathrm{He}_{melt} \qquad (2.2)$$

where the subscripts crush and melt refer to *in vacuo* crushing and melting (Kurz 1986). Care must be taken during the crush step in order to avoid the release of matrix-sited helium. If crushing is prolonged or too intense then this release, (via thermal diffusion), can lead to an underestimated value of ^{3}He$_{cos}$ (Blard *et al.* 2006; Blard *et al.* 2008). To avoid these problems, brief crushing and techniques that do not reduce samples to fine powders are utilised (e.g. Stuart *et al.* 2003).

As it is not possible to distinguish the source of ^{4}He, this method assumes that no radiogenic He is released by crushing. In geologically old rocks, (~60 Ma), this is not the case and calculated values for ^{3}He$_{cos}$ can be significantly underestimated. This can be corrected for by determining the U and Th present within the analysed phenocrysts and surrounding whole-rock (Dunai & Wijbrans 2000; Blard & Farley 2008). A way of avoiding this complication is to chemically etch, or physically abrade, the phenocrysts.

This removes the implanted ^{4}He from the surrounding whole-rock, which is relatively enriched compared to the phenocrysts (Blard and Farley 2008).

2.6 Summary

Use of cosmogenic He for exposure dating in young volcanic rocks is now routine and the technique well established. What has been detailed in this chapter is that the application of cosmogenic He in old volcanic rocks is possible and with care can also become routine. The following chapter details a study designed to assess the applicability of the cosmogenic He exposure dating technique on young surfaces in old rocks and to answer questions about recent landscape evolution to prove the validity of the technique.

CHAPTER 3. Determination of cosmogenic ^{3}He in microphenocrysts of old basalts for unravelling recent landscape evolution

3.1 Introduction

Cosmogenic ^{3}He is routinely used for determining the eruption age of young basaltic lavas (~1 – 100 ka) (Cerling 1990; Kurz *et al.* 1990; Staudacher and Allégre 1993; Licciardi *et al.* 1999; Dunai 2001a; Ammon *et al.* 2009 Foeken *et al.* 2009; 2012). These studies tend to concentrate on the analysis of mafic phenocrysts where the only significant non-cosmogenic He source is magmatic in origin, trapped in melt or CO_2–rich inclusions. This conventional cosmogenic He dating technique is complicated by the presence of radiogenic/nucleogenic He, either when dating young surfaces in old rocks (e.g. Williams *et al.* 2005) or where the exposed volcanic rocks have high U and Th concentrations (e.g. Blard & Farley 2008). Resolving the contribution of non-cosmogenic He is complicated and, in the case of old rocks, long exposure periods are required to beat the combined contribution of radiogenic/nucleogenic and magmatic He (e.g. Schäfer *et al.* 1999; Margerison *et al.* 2005). In this chapter I seek to extend the work of Williams *et al.* (2005) by determining cosmogenic ^{3}He concentration in minerals from old volcanic rocks that have been exposed for short periods.

3.2 Determining cosmogenic He in old volcanic rocks

Cosmogenic ^{3}He concentrations ($^{3}He_{cos}$) in olivine and pyroxene phenocrysts from basalt rocks are calculated from;

$$^{3}He_{cos} = (^{3}He/^{4}He_{melt} - {}^{3}He/^{4}He_{mag}) * {}^{4}He_{melt} \qquad (3.1)$$

where $^{4}He_{melt}$ and $^{3}He/^{4}He_{melt}$ are the ^{4}He concentration and He isotopic composition released by melting. $^{3}He/^{4}He_{mag}$ is the isotopic composition of the magmatic He contained within melt/volatile inclusions that is usually released by *in vacuo* crushing (Kurz 1986).

Where rocks are significantly older than the exposure age, or have critical levels of U, Th and Li, the ingrowth of radiogenic and nucleogenic He may be significant. The release of this He by melting, along with magmatic and cosmogenic He, rule out the use of equation 3.1. The analysis of minerals that do not contain significant amounts of magmatic He, e.g.

microphenocrysts or groundmass minerals, may eliminate this problem (Williams *et al.* 2005). In this case the amount of $^3He_{cos}$ can be calculated from:

$$^3He_{cos} = (^3He/^4He_{melt} - {}^3He/^4He_{rad}) * {}^4He_{melt} \qquad (3.2)$$

where $^3He/^4He_{rad}$ is the isotopic composition of the radiogenic He. The radiogenic $^3He/^4He$ can be calculated from the mineral and whole rock chemical composition and using production rate equations from Morrison and Pine (1955) and Andrews (1985). $^3He/^4He_{rad}$ ranges from 0.005 to 0.015 R_a, with basaltic rocks typically being at the low end of this range (Ozima and Podosek 2002).

This scheme is only valid where the contribution of magmatic He is negligible. The analysis of samples of the same lithology that have been completely shielded from cosmogenic He production allows the total radiogenic and magmatic He concentration to be determined (e.g. Margerison *et al.* 2005). In this case the amount of $^3He_{cos}$ is calculated from:

$$^3He_{cos} = (^3He/^4He_{melt} - {}^3He/^4He_{sh}) * {}^4He_{melt} \qquad (3.3)$$

where $^3He/^4He_{sh}$ is the isotopic composition of He in shielded sample. Once correction for magmatic and radiogenic He is made, the surface exposure age is calculated from the ^3He concentration using the standard equation;

$$\text{Exposure age} = {}^3He_{cos} / P_{cos} \qquad (3.4)$$

where P_{cos} is the $^3He_{cos}$ production rate (atoms g^{-1} a^{-1}).

In the rest of this chapter I present the results of a study that aims to test whether the technique can be used to determine short exposure times (<50 ka) in Tertiary volcanic rocks of Skye, western Scotland.

3.3 Devensian glaciation, Isle of Skye, Scotland: Investigating ice sheet thickness

The last glacial stage in Britain, termed the Devensian, began at approximately 116 ka (Ballantyne 2010). An ice sheet centred in the Highlands and Southern Uplands of

Scotland expanded to cover most of Britain reaching over 1 km in thickness (Ballantyne 1990).

The Isle of Skye supported a locally fed ice mass known as the Skye Ice Dome (SID), which deflected the westward moving mainland ice sheet (Dahl *et al.* 1996). The configuration of the SID was broadly asymmetrical as mainland ice prevented its expansion to the northeast, east and south. It was therefore only able to extend across the centre of the island and the northern peninsulas of Duirinish, Waternish and Trotternish (Dahl *et al.* 1996) (Figure 3.1).

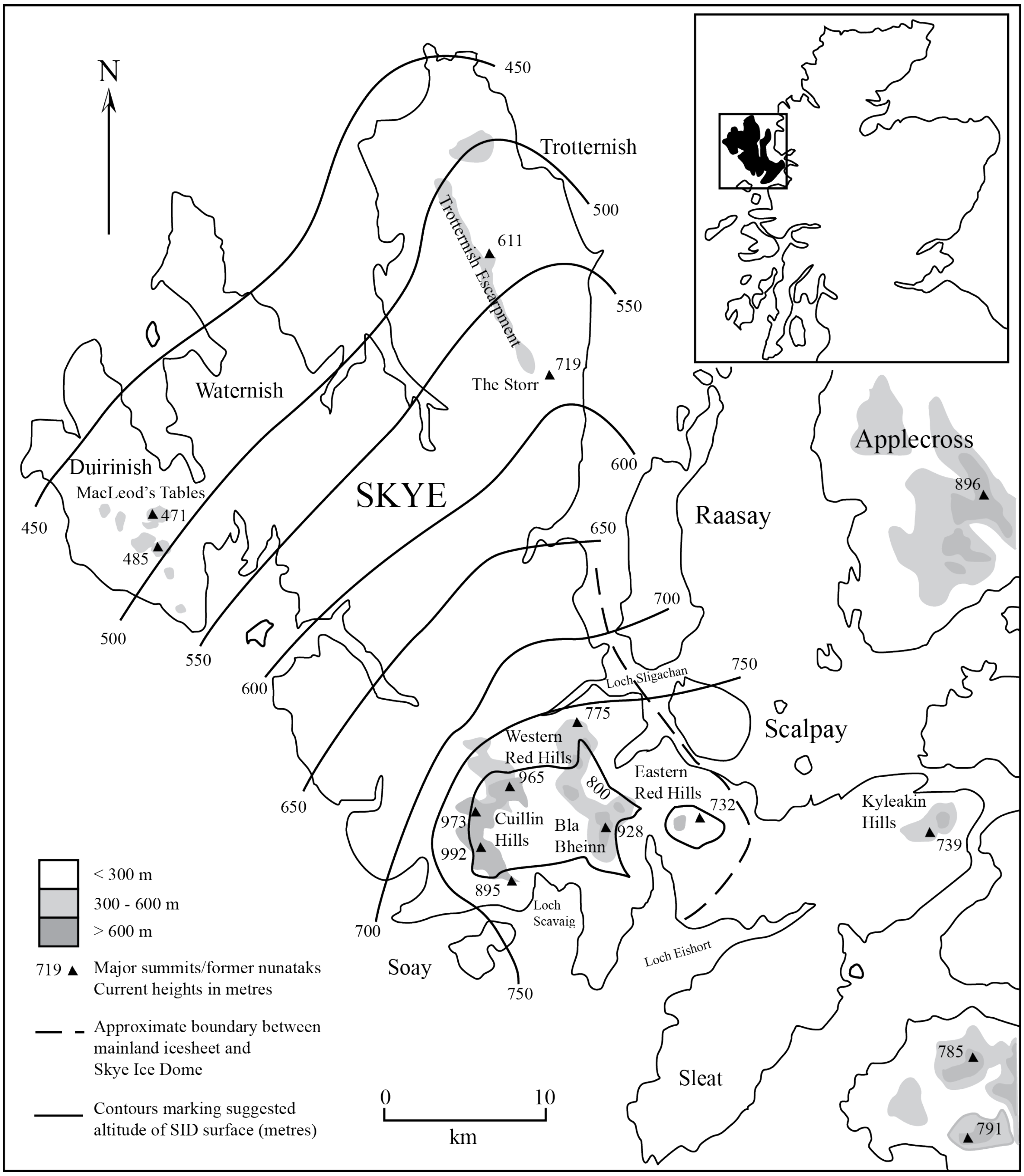

Figure 3.1. Map of the Isle of Skye highlighting locations of major summits and suggested former nunataks. Contours show the suggested thickness of the Skye Ice Dome. Dashed contour shows suggested boundary between the mainland ice sheet and the Skye Ice Dome (after Dahl *et al.* 1996).

Although the approximate extent of the SID has been established there remains debate concerning its maximum thickness. Harker (1901) originally suggested that at its maximum it completely covered the mountains of Skye. In their 1966 study Anderson and Dunham noted a lack of evidence to support the passage of ice on the upper parts of the Trotternish Escarpment and suggested that the mountain summits had remained above the surface of the ice as nunataks (Anderson and Dunham 1966). Ballantyne (1990) reported that the SID moved northwards across the Trotternish peninsula and that all the peaks above 500 m support a layer of *in situ* weathered regolith. He noted that the transition from glacially scoured bedrock to slopes covered by frost-shattered debris occurs over a distance of ~30 m, (580 - 610 m at its southern limit and 440 - 470 m at its northern limit) (Figure 3.2). He supported his interpretation of the existence of a glacial/periglacial boundary with five lines of evidence: (1) joint-depth and Schmidt hammer measurements; (2) the presence of gibbsite in the soils above the boundary; (3) cosmogenic isotope exposure dating; (4) the sharpness of the limit at certain sites; and (5) shear stress calculations (Ballantyne *et al.* 1998).

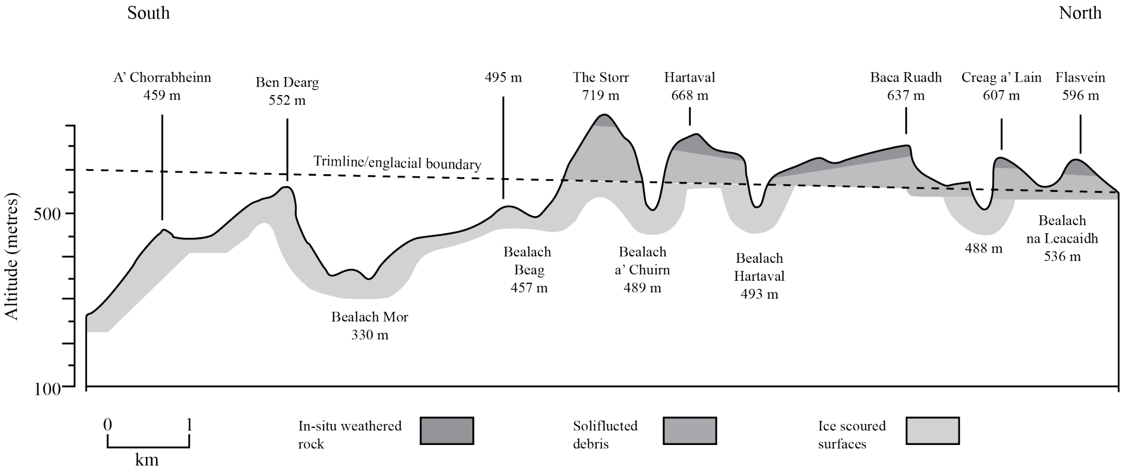

Figure 3.2. Schematic cross-section south to north transect along the Trotternish peninsula. The position of the glacial/periglacial boundary is shown and the change in weathering patterns highlighted. After Ballantyne (1990).

An alternative explanation is that the glacial/periglacial boundaries represent an englacial thermomechanical transition between passive cold-based ice above, and erosive warm-based ice below (Brook *et al.* 1996; Klemen and Borgström 1990). Stone *et al.* (1998) performed analyses of cosmogenic ^{36}Cl in samples from The Storr on the Trotternish peninsula. These results show that the rocks exposed above the glacial/periglacial boundary have significantly higher cosmogenic ^{36}Cl concentrations ($3.7 - 5.3 \times 10^5$ a g^{-1}), and therefore older exposure ages, than those below ($1.17 – 1.18 \times 10^5$ a g^{-1}) (Stone *et al.* 1998). While the cosmogenic ^{36}Cl ages are consistent with the existence of nunataks, they do not preclude the possibility that the upper parts of the Trotternish peninsula were preserved under cold-based ice and contain cosmogenic ^{36}Cl produced prior to being covered by ice. These surfaces have been subjected to weathering since the retreat of the ice-sheet, therefore the ^{36}Cl concentration represents the minimum time since the ice retreated and not an absolute age of the surface.

Stone *et al.* (1998) measured cosmogenic ^{26}Al and ^{10}Be in three bedrock surfaces on An Teallach, Wester Ross, Scotland. Due to the different decay-rates of these two isotopes, a period of prolonged surface burial would produce ^{26}Al/^{10}Be ratio that is lower than the production ratio (Ballantyne *et al.* 1998; Brook *et al.* 1996). ^{26}Al/^{10}Be from above the boundary is indistinguishable from the production ratio, nominally supporting the nunatak theory. However, the ^{26}Al measurements were low precision, resulting in ~10% uncertainty which could mask burial for up to 250 ka (Brook *et al.* 1996).

Coupling a pair of cosmogenic isotopes where one has a short half-life is a potentially more conclusive test. Combining cosmogenic ^{3}He (stable) and ^{36}Cl ($t_{1/2} = 3 \times 10^5$ ka) offers this opportunity. At its simplest, the burial of bedrock under ice will result in differences in ^{3}He and ^{36}Cl concentrations that reflect burial duration (Figure 3.3). One of the main obstacles to routine application of this is currently our inability to precisely determine the cosmogenic He in old rocks.

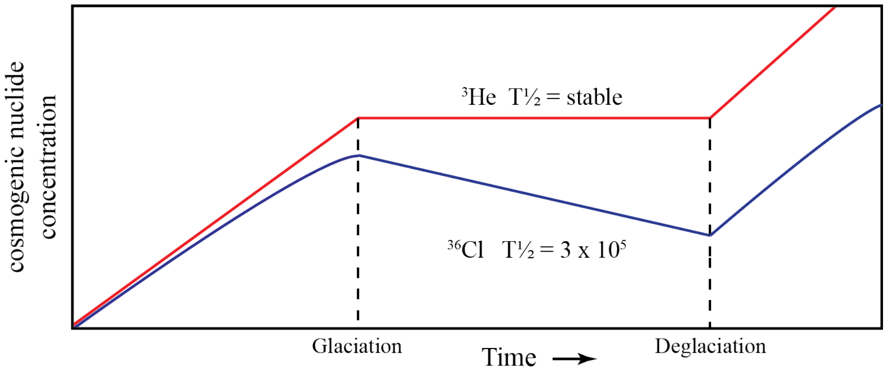

Figure 3.3. Schematic plot of cosmogenic ^{3}He (red) and ^{36}Cl (blue) concentration through time in exposed samples. When exposed the two nuclides accumulate in the upper rock surface. When the surface is covered by > 10 m of ice, the concentration of ^{36}Cl will decrease due to decay while ^{3}He concentration remains constant. Once the ice sheet is removed the cosmogenic nuclides once again accumulate but with an offset that reflects the period of burial under the cold-based ice.

3.4 Geological setting, sampling strategy and sample characterisation

The Trotternish peninsula is the northern most part of the Isle of Skye, NW Scotland. It is dominated by a 23 km long ridge that runs the length of the peninsula from Ben Dearg (522 m) in the south to Meall na Suiramach (543 m) in the north (Figure 3.4). The escarpment contains eight other peaks over 500 m in height with Storr being the highest at 719 m (Ballantyne 1990). It is made up of west dipping tertiary basalts of the Beinn Edra group (Ballantyne 1990), that overlie Jurassic deposits of Kimmeridge Clay, Oxford Clay and Corallian Limestone (Ballantyne 1990). The eastern slopes of the escarpment form an almost continuous cliff up to 250 m high, the result of subsidence of the underlying sedimentary rocks. The western slopes dip shallowly towards the west following the structure of the lavas (Ballantyne 1990).

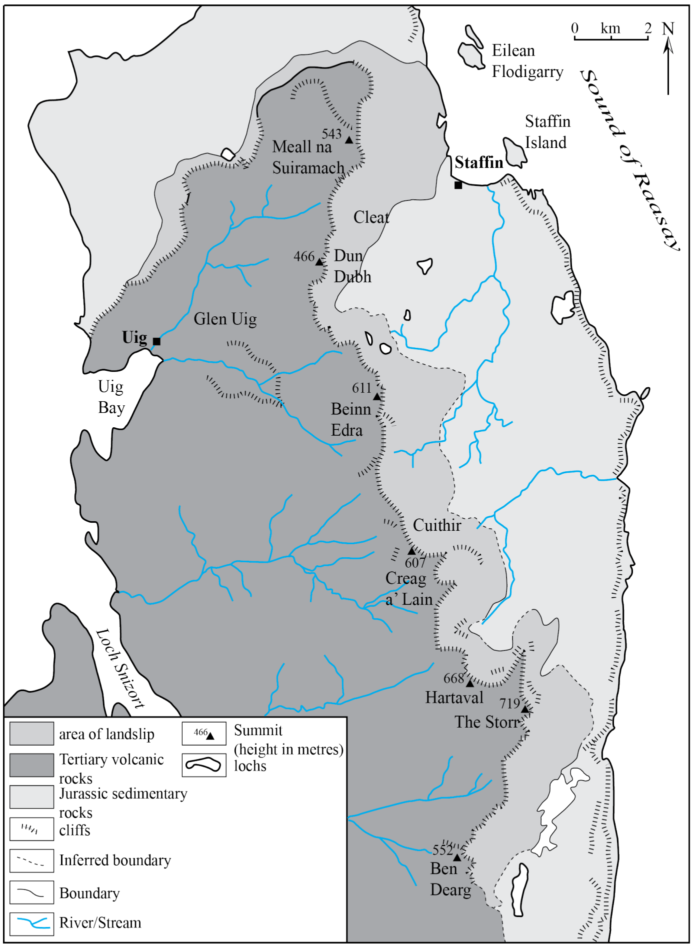

Figure 3.4 Map of the Trotternish peninsula, Isle of Skye, Scotland.

Samples that were collected for cosmogenic ^{3}He analysis are Beinn Edra group basalts (Anderson and Dunham 1966). They were collected from above (TS-1, TS-2) and below (TS-4 and TS-5) the glacial/periglacial boundary (540 - 550 m) on The Storr (Table 3.1, Figures 3.5 and 3.7 A. to D.). Samples were collected from outcrops that were as close as possible in location to those collected by Stone *et al.* (1998) (Table 3.3, Figure 3.5). At each sample site, altitude and latitude/longitude were recorded. Prominent, exposed rock features were targeted to minimise the likelihood of intermittent cover by snow or soil. The uppermost 5 cm of each sample were taken from flat lying surfaces with negligible landscape shielding. It was also ensured that there was no coverage by any material that may have inhibited accumulation of $^{3}\mathrm{He}_{\mathrm{cos}}$ (lichen, moss, soil, etc.).

Location	**Sample**	**Rock type**	**Altitude (m)**	**Latitude/Longitude**	
				N	W
The Storr	TS-1	mugearite	666	57.5110	-6.1861
	TS-2	mugearite	691	57.5092	-6.1848
	TS-4	olivine basalt	441	57.5003	-6.1946
	TS-5	olivine basalt	443	57.4993	-6.1944
Quirang	QR-1	olivine basalt	259	57.6286	-6.2890

Table 3.1. Sample localities, Trotternish, Isle of Skye, UK. Reference datum WGS84. Mean annual atmospheric pressure = 1008 hPa. Densities estimated to be ~3.00 g cm^{3}.

No depth correction was performed as all samples were collected from the uppermost 5 cm of rock in which the production rate of cosmogenic nuclides is assumed to be constant (Masarik and Reedy 1995). Correction for self-shielding were not required as all samples were collected from surfaces inclined at less than 5^{o} (Dunai and Stuart 2009). The latitude/altitude scaling factors of Dunai (2000) have been used to calculate production rates. Composition correction was calculated using the theoretically calculated production rates based on elemental compositions of Masarik (2002). Erosion rate correction has not been applied.

In order to quantify the concentration of non-cosmogenic He in the exposed basalts a shielded sample was collected from a quarried rock face 2.29 m below the top at the Quiraing (Table 3.1, Figures 3.6 and 3.7 E.).

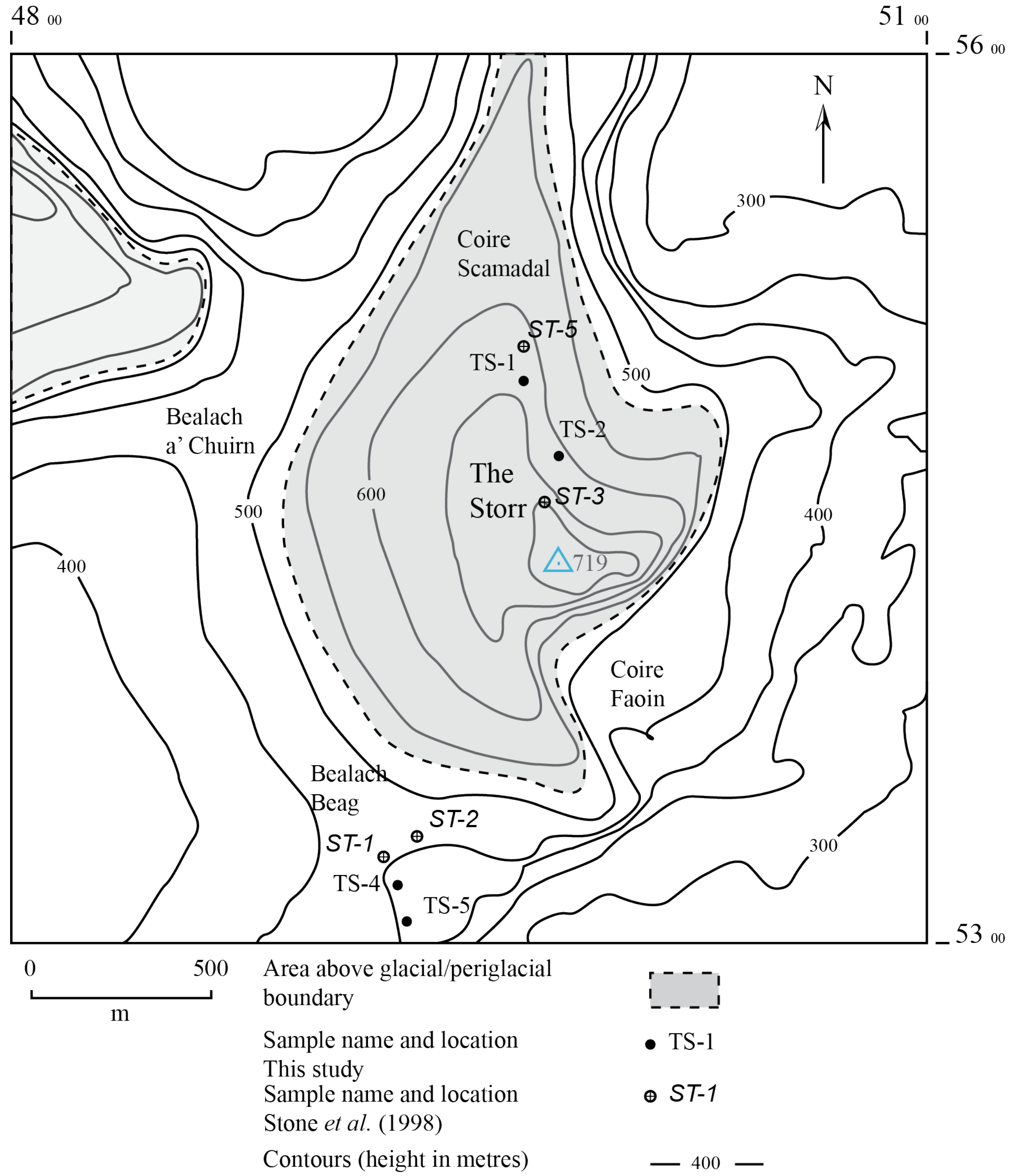

Figure 3.5. Map of the Storr showing the location of exposed samples collected for this study and those collected by Stone *et al.* (1998), and the altitude of the glacial trimline (Ballantyne *et al.* 1998).

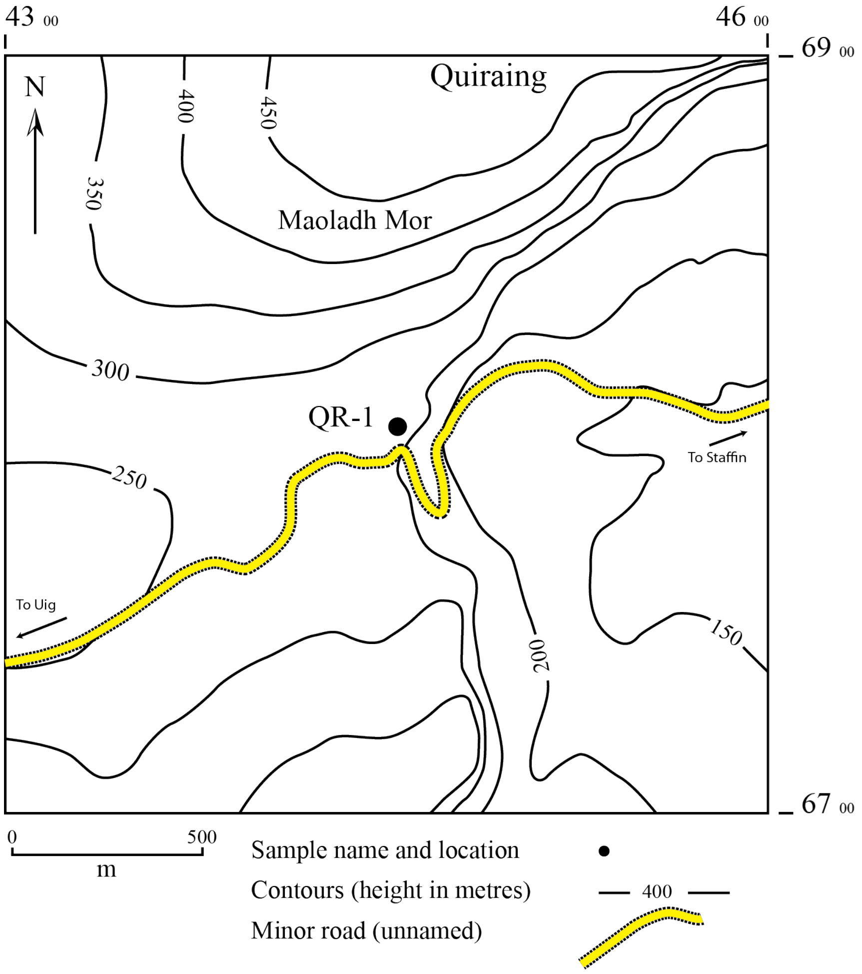

Figure 3.6. Map of the Quiraing showing the location of the shielded sample.

The exposed samples TS-1 and TS-2 are aphyric mugearite basalts. TS-4, TS-5 and QR-1 are olivine basalts (Anderson and Dunham 1966). Petrographic descriptions are given in Appendix 2.

Figure 3.7 A to E. Photographs from sampling sites on The Storr and The Quiraing. A. TS-1, B. TS-2, taken from above the glacial periglacial boundary on The Storr. C. TS-4, D. TS-5 taken from below. E. QR-1 shielded sample taken from the Quiraing.

3.5 Sample preparation

Olivine, ilmenite and plagioclase grains (75–125 µm) were separated from crushed samples using a Frantz magnetic barrier separator. The non-magnetic minerals, largely plagioclase, were removed initially. Moderately pure olivine and ilmenite concentrates were separated by altering the magnet current. The concentrates were cleaned in distilled water, with final purification being done by hand-picking under a binocular microscope. The pure separates were then ultrasonically cleaned in deionised water and analar acetone.

The purity of the mineral fractions was checked under a binocular microscope. The olivine samples (TS-1 ol, TS-2 ol, TS-4 ol, TS-5 ol) typically contained less than 5% ilmenite.

The ilmenite separates (TS-1 ilm, TS-2 ilm) contained on average < 5% olivine. No plagioclase was present in any separate. The plagioclase separates were >95% pure.

3.6 Analytical techniques

Helium was extracted from multiple aliquots of each sample. Approximately 100 - 200 mg wer loaded into a square shaped 'well' in a copper pan and covered with a quartz glass cover. The pan was placed in a stainless steel laser cell with a sapphire glass window then pumped and baked for more than 12 hours. The samples were degassed for 10 minutes with a 25 W, 808 nm diode laser operated at ~75% power (Foeken *et al.* 2009). Degassed pyroxene grains were added to the olivine and plagioclase concentrates to act as a heat flux for the diode laser. The released gas was purified by exposure to a SAES® GP-50 getter operated at 250°C for 10 minutes to remove all active gas species followed by 10 minutes exposure to a liquid-N_2 cooled charcoal cold-finger (77 K) to adsorb heavy noble gases. A cold GP50 getter included in the mass spectrometer source volume minimised the partial pressure of residual gases during analysis. Helium isotope abundances and ratios were determined using a MAP 215-50 mass spectrometer (see section 5.4.1 for description). All isotopes were measured in 10 cycles by peak jumping up mass over a period of ~1 hour. Helium concentrations and isotope compositions were calculated by comparison to HESJ calibration gas (Matsuda *et al.* 2002). The ^{3}He and ^{4}He blanks of the melting process averaged $3.9 \pm 4.6 \times 10^3$ and $1.1 \pm 1.7 \times 10^8$ atoms respectively. Calibrations of the mass spectrometer were performed every five analyses. Calibrations used 1.8×10^{11} atoms ^{4}He in order to approximate the amount of gas released from the samples and eliminate pressure dependence effects within the source. Two samples (TS-2 and TS-4) were reheated, in both cases ^{3}He concentration was indistinguishable from blank level.

3.7 Results

Helium isotope data from all samples and exposure ages are presented in Table 3.2. All measured ratios (R) have been normalised to the ^{3}He/^{4}He of air (R_a: 1.39×10^{-6}) (Figure 3.8). The two plagioclase separates yielded no significant cosmogenic He, consistent with complete diffusive loss (e.g. Margerison *et al.* 2007). They will not be discussed further.

Cosmogenic ^{3}He ages are calculated using three different methods and displayed in Table 3.2. The first uses equation 3.2 and assumes that there is no magmatic He in the samples and assumes radiogenic ^{3}He/^{4}He = 0.01 R_a. The second method also uses equation 3.2 but uses the $^3He/^4He$ measured in the olivine from shielded sample to account for all the non-cosmogenic He. The third method uses the ^3He concentration of the shielded olivine to correct for the radiogenic and magmatic He contribution. Ages calculated from all methods are plotted against altitude in Figures 3.8, 3.9 and 3.10.

Cosmogenic ^3He was measured from olivine in all samples and ilmenite in two samples (TS-1 and TS-2). In both samples, olivine $^3He_{cos}$ ($2.8 – 5.2 \times 10^6$ atoms g^{-1}) is higher than the ilmenite ($1.9 – 3.9 \times 10^6$ atoms g^{-1}). The olivine from samples TS-4 and TS-5 have lower ^3He concentrations than TS-1 and TS-2, ranging from $2.1 – 2.9 \times 10^6$ atoms g^{-1}.

In TS-1 and TS-2 the $^3He/^4He$ of ilmenite (0.28 – 0.57 R_a) is slightly lower than olivine (0.48 – 0.99 R_a). Olivine from TS-2 has a markedly higher $^3He/^4He$ (0.93 – 0.96 R_a) than that of TS-1 (0.48 – 0.52 R_a), which is more in line with the values from the ilmenites. The $^3He/^4He$ of TS-4 and TS-5 olivines range from 0.93 to 1.66 R_a overlapping TS-2 olivine. The ^3He concentrations determined from olivine from the shielded sample (n=2) range $1.47 - 1.53 \times 10^6$ atoms g^{-1}, and $^3He/^4He$ of 0.62 – 0.75 R_a. The concentration from the two aliquots of shielded sample overlap within uncertainty.

3.7.1 Exposure ages calculated assuming radiogenic He only

Exposure ages calculated using radiogenic He correction are shown in Table 3.2 (denoted $^3He/^4He_{rad}$) and Figure 3.9. They are systematically older than those calculated via the other two methods as it effectively assumes that all ^3He is cosmogenic. Age ranges are typically larger than the uncertainty on individual age determinations. Despite this, several observations can be made. The samples from above the trimline yield ages ranging from 16 to 33 ka and those from below range from 12 to 16 ka. The average age of the olivine and ilmenite from TS-1 overlap but those from TS-2 do not. The ages of the olivine from below the trimline (TS-4 and TS-5) do not overlap. They do, however, overlap with the lower range of TS-2 olivine.

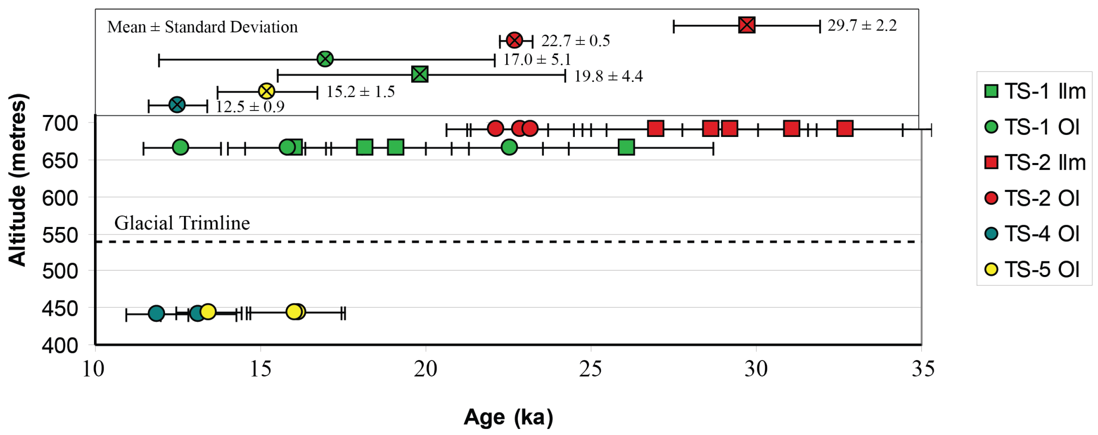

Figure 3.8. Plot of ^{3}He$_{cos}$ exposure ages (calculated from radiogenic He correction) against altitude. Symbols with crosses are average age. All uncertainties are 2σ.

3.7.2 Exposure ages calculated using ^{3}He/^{4}He of shielded sample

Exposure ages calculated using the ^{3}He/^{4}He of the shielded sample are shown in Table 3.2 (denoted ^{3}He/^{4}He$_{sh}$) and Figure 3.9. The exposure ages of ilmenite from TS-1 and TS-2, and TS-1 olivine are negative as the ^{3}He/^{4}He is lower than that of QR-1. The remaining samples yield positive exposure ages ranging from 3 – 7.5 ka. Average ages for both mineral types in samples TS-1 and TS-2 do not overlap. The ages from the olivines below the trimline overlap with TS-2 olivine.

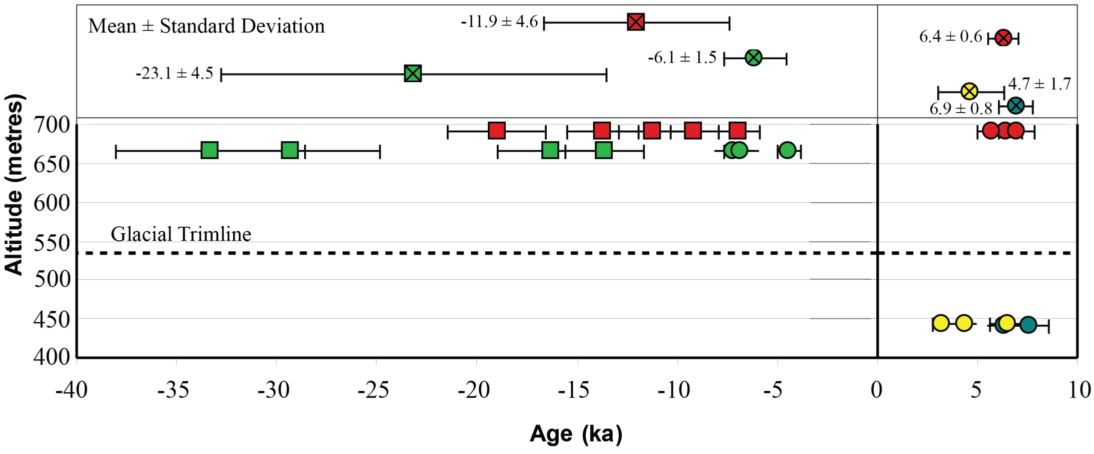

Figure 3.9. Plot of ^{3}He$_{cos}$ exposure ages (calculated from shielded sample ^{3}He/^{4}He correction) against altitude. Symbols are the same as Figure 3.8.

3.7.3 Exposure ages calculated with shielded sample ^{3}He concentration

Exposure ages calculated using the ^{3}He concentration of the shielded sample are shown in Table 3.2 and Figure 3.10. Samples from above the trimline yield ages ranging from 3 to 20 ka and are older on average than those collected from below 3 to 8 ka. There is no systematic behaviour in the ages calculated from the different mineral concentrates. The TS-1 ilmenite age range (3.4 – 14.0 ka) overlaps, but are slightly younger than, TS-1 olivine (6.0 – 16.1 ka). TS-2 ilmenite ages overlap but are slightly older (14.8 – 20.6 ka) than TS-2 olivine (15.7 – 16.7 ka).

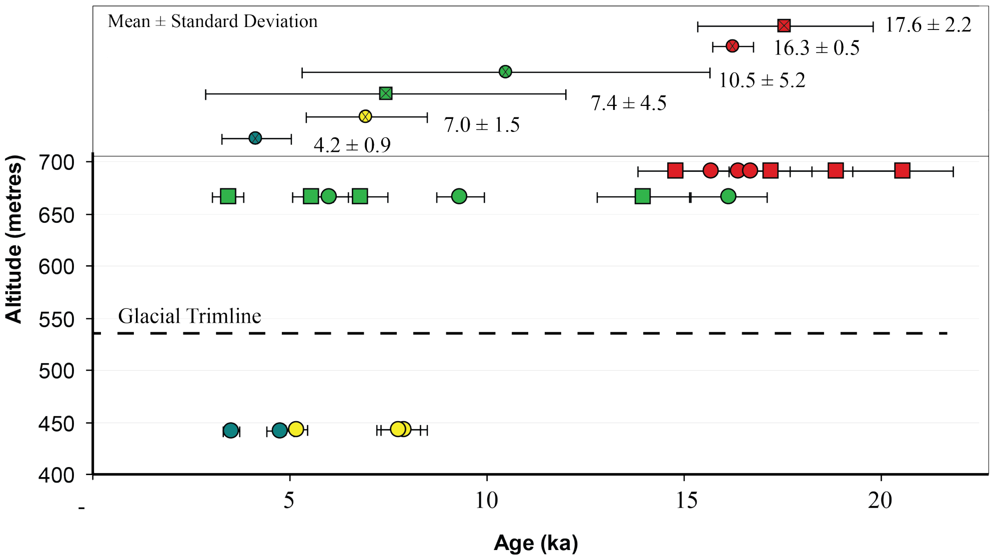

Figure 3.10. $^3He_{cos}$ exposure ages (calculated from shielded sample ^{3}He correction) against altitude of sample. Symbols are the same as Figure 3.8. All uncertainties are 2σ.

3.8 Discussion

3.8.1 Cosmogenic He ages

Correction for radiogenic $^3He/^4He$ assumes the samples contain negligible magmatic He. However, the high $^3He/^4He$ of olivine from the shielded sample suggests magmatic ^{3}He is present. This is consistent with the olivine separate representing fragments of rare phenocrysts (see Appendix 2). Despite the fact that they are closest to the ^{36}Cl ages of Stone *et al.* 1998, they should be treated as upper limits.

			Production rate	^{3}He		^{3}He/^{4}He		^{3}He$_{cos}$		Age (ka)		Age (ka)		Age (ka)	
Sample	Mineral	Weight (g)	a g^{-1} yr^{-1}	10^{6} a g^{-1}	±	R/R$_{a}$	±	10^{6} a g^{-1}	±	^{3}He/^{4}He$_{rad}$	±	^{3}He/^{4}He$_{sh}$	±	^{3}He$_{sh}$	±
TS-1-1	Ilmenite	0.1005	114.0	2.28	0.23	0.28	0.04	0.78	0.08	19.14	2.18	-29.29	-4.48	6.81	0.69
TS-1-2	Ilmenite	0.0939	114.0	3.09	0.26	0.31	0.03	0.39	0.05	26.12	2.56	-33.31	-4.71	13.98	1.17
TS-1-3	Ilmenite	0.1005	114.0	1.89	0.22	0.35	0.05	1.59	0.13	16.04	2.05	-16.30	-2.67	3.44	0.40
TS-1-4	Ilmenite	0.1216	114.0	2.13	0.19	0.40	0.05	0.63	0.05	18.16	1.82	-13.64	-1.95	5.55	0.48
TS-1-1	Olivine	0.1050	217.2	3.52	0.23	0.48	0.05	2.02	0.13	15.84	1.31	-7.17	-0.94	9.32	0.60
TS-1-2	Olivine	0.0951	217.2	5.01	0.30	0.53	0.05	3.51	0.21	22.55	1.77	-6.81	-0.88	16.14	0.96
TS-1-3	Olivine	0.1100	217.2	2.81	0.22	0.52	0.06	1.31	0.10	12.63	1.19	-4.40	-0.61	6.02	0.48
TS-2-1	Ilmenite	0.1040	116.6	3.51	0.22	0.42	0.04	2.01	0.12	29.24	2.33	-18.99	-2.46	17.20	1.05
TS-2-2	Ilmenite	0.0880	116.6	3.42	0.34	0.50	0.06	1.92	0.19	28.65	3.18	-11.19	-1.68	16.47	1.62
TS-2-3	Ilmenite	0.0910	116.6	3.90	0.25	0.54	0.05	2.40	0.15	32.70	2.63	-9.14	-1.19	20.56	1.27
TS-2-4	Ilmenite	0.0936	116.6	3.70	0.35	0.57	0.07	2.20	0.21	31.09	3.34	-6.93	-1.03	18.87	1.79
TS-2-5	Ilmenite	0.1400	116.6	3.22	0.21	0.46	0.05	1.73	0.11	26.97	2.23	-13.72	-1.80	14.80	0.97
TS-2-1	Olivine	0.0941	222.0	5.14	0.26	0.96	0.08	3.64	0.18	22.86	1.61	6.44	0.79	16.39	0.79
TS-2-2	Olivine	0.1043	222.0	5.20	0.32	0.99	0.09	3.71	0.23	23.17	1.84	6.98	0.90	16.69	1.01
TS-2-3	Olivine	0.1141	222.0	4.98	0.24	0.93	0.08	3.48	0.16	22.16	1.53	5.74	0.71	15.69	0.72

Sample	Mineral	Weight (g)	Production rate a g^{-1} yr^{-1}	^{3}He 10^6 a g^{-1}	±	^{3}He/^{4}He R/R$_a$	±	^{3}He$_{cos}$ 10^6 a g^{-1}	±	Age (ka) ^{3}He/^{4}He$_{rad}$	±	Age (ka) ^{3}He/^{4}He$_{sh}$	±	Age (ka) ^{3}He$_{sh}$	±
TS-4-1	Olivine	0.1978	177.7	2.13	0.13	1.51	0.14	0.628	0.04	11.88	0.93	6.37	0.82	3.53	0.21
TS-4-2	Olivine	0.1954	177.7	2.35	0.17	1.66	0.17	0.848	0.06	13.12	1.15	7.56	1.02	4.77	0.34
TS-5-1	Olivine	0.2421	178.0	2.91	0.22	0.93	0.1	1.41	0.1	16.13	1.45	4.34	0.59	7.91	0.58
TS-5-2	Olivine	0.2020	178.0	2.88	0.10	1.18	0.12	1.38	0.1	16.03	1.42	6.49	0.88	7.76	0.56
TS-5-3	Olivine	0.2229	178.0	2.42	0.13	0.93	0.08	0.92	0.05	13.44	0.99	3.23	0.41	5.19	0.28
QR-1-1	Olivine	0.2035	-	1.53	0.15	0.75	0.09	-	-	-	-	-	-	-	-
QR-1-2	Olivine	0.2165	-	1.47	0.19	0.62	0.09	-	-	-	-	-	-	-	-
TS-1-1	Plagioclase	0.4038	-	0.04	0.02	1.08	0.68	-	-	-	-	-	-	-	-
TS-2-1	Plagioclase	0.2581	-	0.01	0.01	0.65	0.68	-	-	-	-	-	-	-	-

Table 3.2. Data of He analyses of exposed samples from The Storr and shielded sample from the Quiraing. Ages displayed were calculated using; Eq. 3.2 with ^{3}He/^{4}He$_{rad}$ (calculated ^{3}He/^{4}He of radiogenic contribution), Eq. 3.2 with ^{3}He/^{4}He$_{sh}$ (measured ^{3}He/^{4}He from shielded sample) and Eq. 3.3 with ^{3}He$_{sh}$ (measured ^{3}He concentration of the shielded sample). Production rates calculated via Dunai (2000) version 1.1.9.11.2001. All uncertainties are 2σ.

The negative and low exposure ages calculated by correction using the ^{3}

the ratios relatively high value. This is most easily understood as resul

in the amount of magmatic and radiogenic He in samples. Figur

concentrations of all samples against ^{3}He/^{4}He. All the samples that

have ^{4}He concentrations that are higher than QR-1. This is likely to be

TS-2 are a different lithology (aphyric mugearite basalt). This highlight

obtaining a shielded sample from exactly the same lithology as the expo

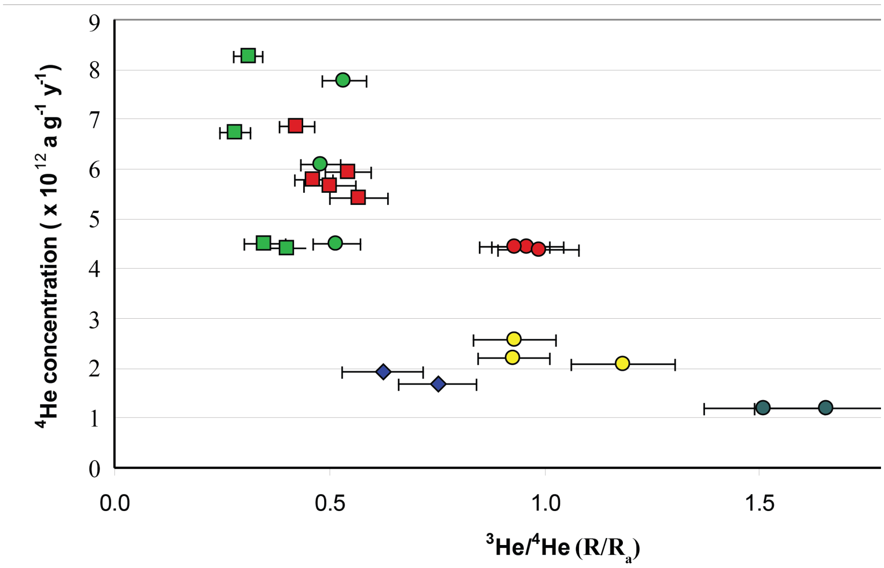

Figure 3.11. ^{4}He concentration plotted of each sample against ^{3}He/^{4}He. S
Figure 3.8. Blue diamonds represent shielded sample QR-1.

In order to remove the effect of variable non-cosmogenic He on ^{3}He/

are calculated using only the ^{3}He of the shielded sample. Figure 3.12

samples have variably higher concentrations of ^{3}He than the shielded

ages calculated using this method are lower limits as there remains the

shielded sample contains a small volume of cosmogenic He.

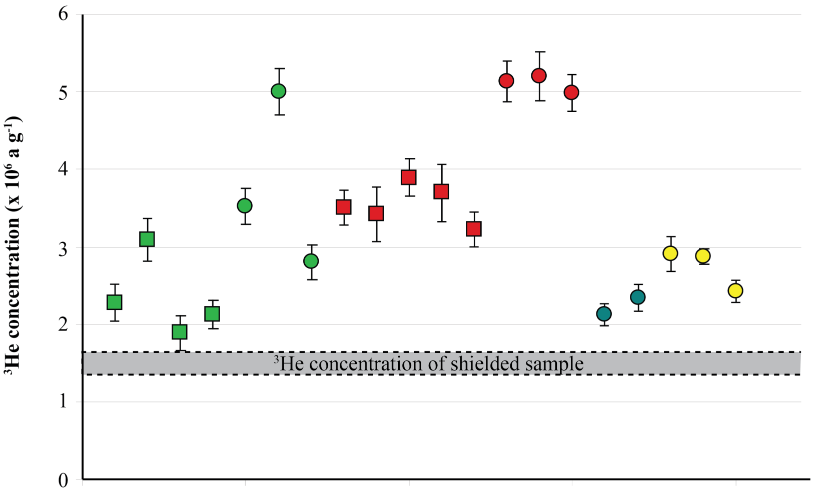

Figure 3.12. ^{3}He concentrations of exposed samples in relation to the average concentration from the shielded sample. Uncertainties are 2σ.

3.8.2 Comparison of cosmogenic ^{3}He and ^{36}Cl ages

The average $^3He_{cos}$ exposure ages of surfaces above the trimline are broadly older than those from below (Table 3.2; Figure 3.10). However, they are systematically younger than the ^{36}Cl exposure ages determined by Stone *et al.* (1998) (Table 3.3). For example, the maximum cosmogenic He age of surfaces from above the trimline (22.2 - 32.7 ka; TS-2, calculated with radiogenic correction) is significantly less than the age determined from ^{36}Cl. If the trimline of Ballantyne *et al.* (1998) is an englacial thermomechanical boundary, the $^3He_{cos}$ ages would be expected to be older than ^{36}Cl ages, due to the presence of $^3He_{cos}$ inherited from earlier exposure (Figure 3.3). The upper limit of the cosmogenic He age of surfaces from below the trimline (13.4 – 16.1 ka; TS-5, calculated with radiogenic correction) is less than the age determined from ^{36}Cl (~17.5 ka).

On the assumption that the surfaces sampled here record a similar exposure history to that recorded by those sampled in the previous study, there are several possible explanations for the apparently low $^3He_{cos}$ ages.

Sample	Grid	Altitude	Cl	^{36}Cl	±	Exposure	±
	Reference	(m)	(ppm)	$\times 10^5$ a g^{-1}		age (ka)	
Samples below boundary							
ST-1	NG 491 532	450	6 ± 2	1.18	0.08	17.4	1.3
ST-2	NG 491 532	445	2 ± 1	1.17	0.08	17.6	1.4
Samples above boundary							
ST-3	NG 495 542	700	11 ± 2	5.31	0.31	>70.3	5.1
ST-5	NG 494 546	640	3 ± 1	3.71	0.19	>50.2	3.3

Table 3.3. ^{36}Cl exposure age data from Stone *et al.* (1998). Samples are basalt of the Beinn Edra group and were collected from The Storr, Isle of Skye, Scotland. All analyses were carried out on whole rock groundmass.

Stone *et al.* (1998) carried out their study while the ^{36}Cl technique was in its infancy. Several studies in the intervening fifteen years have refined the production rates used in the calculation of ^{36}Cl exposure ages (e.g. Philips *et al.* 2001; Licciardi *et al.* 2008; Schimmelpfennig *et al.* 2009) therefore there is scope to review the production rates used. The spallation production rates for K and Ca of Stone *et al.* (1998) appear to be in broad agreement of those in a more recent study of Schimmelpfennig *et al.* (2009) but the thermal neutron capture is not. To adequately quantify this requires knowledge of the flux of thermal neutrons at the surface/atmosphere boundary, which is complex and sensitive to the presence of water and snow cover (Philips *et al.* 2001; Schimmelpfennig *et al.* 2009). Knowledge of the most important chemical elements (H, Li, B, Sm, and Gd) that scatter and absorb low-energy thermal neutrons must be obtained. This is because the distribution of thermal neutrons below the first few metres of the rock surface, are influenced by the concentrations of these elements. Stone *et al.* (1998) used a neutron flux of $P_f(0) = 590 \pm 40$ $g^{-1}a^{-1}$ for neutron capture in their study. Using a similar neutron flux Schimmelpfennig *et al.* (2009) noted an overestimation of exposure ages in a whole rock basalt sample from Mount Etna that was caused by an excess of ^{36}Cl that did not originate from atmospheric, magmatic or radiogenic sources. They have proposed that the low-energy thermal neutron capture reaction is underestimated and conclude that a neutron flux of 1166 g^{-1} a^{-1} for "hydrous" samples (previously calculated by Swanson and Caffee 2001), may be more suitable for external moisture and snow cover conditions. Stone *et al.* (1998) may have underestimated the ^{36}Cl production from thermal neutron capture reaction. In order to quantify these potential changes in the determination of exposure ages they have been recalculated using the method described in Schimmelpfennig *et al.* (2009) and are presented in Table 3.4. The recalculated exposure ages below the boundary are younger and those above are older than those previously calculated by Stone *et al.* (1998).

Table 3.5 shows the differences between the ^{3}He and ^{36}Cl ages expressed as a percentage. Despite these changes the newly calculated ^{36}Cl exposures ages still do no reflect the results from this study and remain older than the ^{3}He exposure ages. If the greatest production rates calculated from previous studies are used (i.e. P_{ca} = 76 ± 5 $(_g\text{Ca})^{-1}$ a^{-1} (Zreda *et al.* 1991), P_K = 228 ± 18 $(_g\text{K})^{-1}$ a^{-1} (Swanson and Caffee 2001) and P_{Fe} = 6.75 $(_g\text{Fe})^{-1}$ a^{-1} (Masarik 2002)) the ages still do not reflect those determined in this study. These results are shown in Table 3.5. The exception is that ST-1 and ST-2 overlap TS-1 within uncertainty (both olivine and ilmenite). These samples were however collected from different altitudes, ST-1 = 450 m, ST-2 = 445 m and TS-1 = 666 m, from either side of the boundary. No data is available on the U and Th content of the samples of Stone *et al.* (1998) therefore in order to quantify the radiogenic contribution a range of theoretical values were applied from 0 – 20 ppm. Even with the maximum values applied the recalculated ages decreased by less than 1%.

Sample	Grid Reference	Altitude (m)	Thickness (correction) (g.cm-2)	CaO (wt%)	K_2O (wt%)	TiO_2 (wt%)	Fe_2O_3 (wt%)	Cl (ppm)	^{36}Cl $\times 10^5$ a g^{-1}	±	Exposure age (ka)	±	% Difference
Samples below boundary													
ST-1	NG 491 532	450	1.4 (0.956)	7.28	0.315	1.42	22.28	6 ± 2	1.18	0.08	16.3	1.8	-6.8
ST-2	NG 491 532	445	1.4 (0.956)	7.33	0.34	1.42	22.28	2 ± 1	1.17	0.08	16.9	1.7	-4.15
Samples above boundary													
ST-3	NG 495 542	700	0.9 (0.973)	6.91	0.191	1.42	22.28	11 ± 2	5.31	0.31	75.8	8.0	6.0
ST-5	NG 494 546	640	2.2 (0.935)	7.74	0.174	1.42	22.28	3 ± 1	3.71	0.19	55.7	5.7	9.3

Table 3.4. ^{36}Cl ages recalculated from study of Stone *et al.* (1998). Chemical data for bulk rock taken from Thomson *et al.* (1972). Production rates at SLHL: $P_{Ca} = 48.8 \pm 3.4$ $({}_{g}Ca)^{-1}$ a^{-1} (Stone *et al.* 1996). $P_K = 162 \pm 24$ $({}_{g}K)^{-1}$ a^{-1} (Evans *et al.* 1997). $P_{Ti} = 13 \pm 3$ $({}_{g}Ti)^{-1}$ a^{-1} (Fink *et al.* 2000). $P_{Fe} = 1.9$ $({}_{g}Fe)^{-1}$ a^{-1} (Stone 2005). Slow negative muon capture = 190 μ g^{-1} a^{-1} (Heisinger *et al.* 2002). Total low-energy neutron capture $P_f(0) = 1166$ g^{-1} a^{-1} (Swanson and Caffee 2001). Apparent fast neutron attenuation coefficient Λ_f = 177 g cm^{-2}. Scaling factors for nucleogenic and spallogenic reactions calculated with cosmocalc (Vermeesch 2007), using the scaling method of Dunai (2000); $S_{el,s}$, $S_{el,n}$ = 1.48 and $S_{el,\mu}$ = 1.24 for all samples.

Sample	Grid Reference	Altitude (m)	Exposure age (ka)	±
Samples below boundary				
ST-1	NG 491 532	450	10.3	1.1
ST-2	NG 491 532	445	10.6	1.1
Samples above boundary				
ST-3	NG 495 542	700	47.2	4.7
ST-5	NG 494 546	640	34.4	3.3

Table 3.5. ^{36}Cl ages recalculated with greatest production rates. All other par to those detailed in Table 3.4.

The production of thermal neutrons increases rapidly in the first few beneath the rock surface (Philips *et al.* 2001; Schimmelpfennig *et a* typically results in a higher ^{36}Cl contribution from thermal neutrons th surface (Figure 3.13).

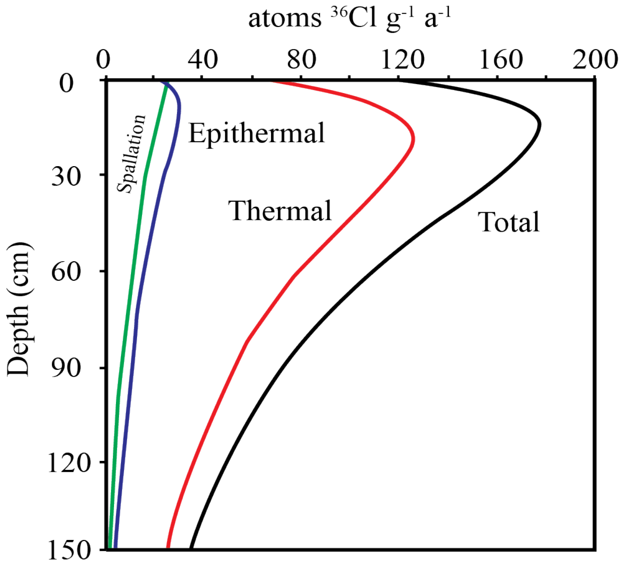

Figure 3.13. Schematic of ^{36}Cl production pathways with depth below the surf

Without knowledge of all relevant chemical elements for scattering thermal neutrons present within the samples, an underestimation c capture production rate could cause different results. Changes in produ for less than 10% of the discrepancy between the ^{36}Cl (Stone *et al* exposure ages determined in this study.

Diffusive loss of He could potentially explain the disparity. Previous studies have shown that He has a very low diffusivity in olivine; 10^{-22} cm^2 s^{-1} at 20°C (Trull *et al.* 1991), not enough to account for loss from large (few mm) grains. However, diffusion rates have been determined on near-gem quality grains of olivine from young volcanic rocks; Trull *et al.* (1991) investigated 2 mm grains from a 500 ka Kula ankaramite and Schuster *et al.* (2003) used spherical ~690 µm grains from a Guadalupe Island olivine megacryst. Although pure, fresh olivine was analysed in this study, there is likelihood that the mineral structure is less coherent, thus He diffusion may be more rapid. The amount of He that would need to diffuse from the grains in order to reduce the exposure ages of Stone *et al.* (1998) is not systematic (Table 3.6). The amount of He needed to diffuse from olivine is one order of magnitude greater than in ilmenite for samples TS-1 and TS-2. The amount of He needed to diffuse from samples TS-4 and TS-5 (olivine) is two orders of magnitude less than the olivine fractions of TS-1 and TS-2. Systematic He loss could be argued for sample TS-2. The amount lost from each aliquot overlaps within uncertainty. For all other samples, however, the amount lost from each aliquot varies by up to 20%. It was assumed that ~100 mg sample was homogenous and all concentrations should be indistinguishable. This does not appear to be the case however and further study of the diffusion in the olivine and ilmenite analysed here is worthy of further study.

	^{3}He content required for 55.7 ka	^{3}He content required for 75.8 ka	^{3}He content measured	Difference 55.7 ka	Difference 75.8 ka	% Difference for 75.8 ka	% Difference for 55.7 ka
TS-1-1 Ol	1.21E+07	1.65E+07	3.52E+06	8.58E+06	1.29E+07	64.77%	54.92%
TS-1-2 Ol	1.21E+07	1.65E+07	5.01E+06	7.09E+06	1.15E+07	53.34%	41.43%
TS-1-3 Ol	1.21E+07	1.65E+07	2.81E+06	9.29E+06	1.37E+07	70.84%	62.30%
TS-1-1 Ilm	6.01E+06	8.64E+06	2.28E+06	3.73E+06	6.36E+06	58.25%	44.98%
TS-1-2 Ilm	6.01E+06	8.64E+06	3.09E+06	2.92E+06	5.55E+06	47.32%	32.07%
TS-1-3 Ilm	6.01E+06	8.64E+06	1.89E+06	4.12E+06	6.75E+06	64.11%	52.14%
TS-1-4 Ilm	6.01E+06	8.64E+06	2.13E+06	3.88E+06	6.51E+06	60.45%	47.65%
TS-2-1 Ol	1.17E+07	1.68E+07	5.14E+06	6.56E+06	1.17E+07	53.20%	38.95%
TS-2-2 Ol	1.17E+07	1.68E+07	5.20E+06	6.50E+06	1.16E+07	52.79%	38.46%
TS-2-3 Ol	1.17E+07	1.68E+07	4.98E+06	6.72E+06	1.18E+07	54.33%	40.29%
TS-2-1 Ilm	6.14E+06	8.84E+06	3.51E+06	2.63E+06	5.33E+06	43.15%	27.29%
TS-2-2 Ilm	6.14E+06	8.84E+06	3.42E+06	2.72E+06	5.42E+06	44.20%	28.49%
TS-2-3 Ilm	6.14E+06	8.84E+06	3.90E+06	2.24E+06	4.94E+06	38.77%	22.35%
TS-2-4 Ilm	6.14E+06	8.84E+06	3.70E+06	2.44E+06	5.14E+06	40.98%	24.83%
TS-2-5 Ilm	6.14E+06	8.84E+06	3.22E+06	2.92E+06	5.62E+06	46.59%	31.23%

	^{3}He content required for 16.3 ka	^{3}He content required for 16.9 ka	^{3}He content measured	Difference 16.3 ka	Difference 16.9 ka	% Difference for 16.3 ka	% Difference for 16.9 ka
TS-4-1 Ol	2.90E+06	3.00E+06	2.13E+06	7.67E+05	8.73E+05	15.25%	17.01%
TS-4-2 Ol	2.90E+06	3.00E+06	2.35E+06	5.47E+05	6.53E+05	10.42%	12.20%
TS-5-1 Ol	2.90E+06	3.01E+06	2.91E+06	-8.60E+03	9.82E+04	-0.15%	1.66%
TS-5-2 Ol	2.90E+06	3.01E+06	2.88E+06	2.14E+04	1.28E+05	0.37%	2.18%
TS-5-3 Ol	2.90E+06	3.01E+06	2.42E+06	4.81E+05	5.88E+05	9.05%	10.84%

Table 3.6. Helium contents (atoms) required to yield ages comparable to cosmogenic ^{36}Cl ages, the actual amount measured and the differences expressed as both amounts and percentages.

3.8.3 Future

Clearly in order to better quantify the exposure history of the sampl study, analysis of a shielded sample of the same lithology as TS-1 and T uncertainties introduced by variation in magmatic and radiogenic He, ar be used for $^3He_{cos}$ exposure age determination.

More generally, several lines of investigation need to be groundmass/microphenocryst phases will be suitable for exposure datin

Diffusion rates of cosmogenic He in representative minerals are poorly understanding of the extent of this effect will require measurement in a (see previous section).

Given the grain size of the minerals analysed, ejection and implantati considered. The ejection distances of radiogenic ^{4}He (11-34 μm), nu μm) and cosmogenic ^{3}He affect distribution in minerals (Dunai and Wi *et al.* 2006; Dunai *et al* 2007; Blard and Farley 2008). In olivine (Fo_{80}), for $^3He_{cos}$ and ^{3}H the ejection distances range from 54–170 μm respectively (Ziegler *et al.* 2008). As ejection distances are similar t sizes utilised in this study a significant proportion of the cosmogenic ^{3}H in the surrounding host rock (Farley *et al.* 2006). Gains by implantatio ejection are difficult to quantify due to a limited knowledge of t spectrum and the spallation $^3H/^3He$ production ratio (Masarik 2002; That said, the low production rate of He in ilmenite relative to oli plagioclase means a significant proportion may be implanted.

The chemical composition of the basalt lavas used in this and the Stone need to be measured in order to quantify the degree to which the calcul responsible for the discrepancy in results. Further, despite my best eff possibility that the surfaces sampled in this study have a different expos sampled by Stone *et al.* (1998).

3.9 Conclusions

Helium isotopes were measured in olivine, ilmenite and plagioclase from early Tertiary basalts from The Storr, Isle of Skye, Scotland. Correction for radiogenic He was performed using three different methods. The samples quantitatively retain cosmogenic ^{3}He but yield variable exposure ages that are lower than previously determined ^{36}Cl by (Stone *et al.* 1998). The lines of investigation outlined in the previous section certainly merit pursuit as the potential remains for reductions in disparity between ages. This is particularly so through analysis of a shielded sample of the same lithology as TS-1 and TS-2 and a greater understanding of the cosmogenic ^{36}Cl production.

Chapter 4. Noble gas mass spectrometry: History, principles and applications

4.1 Introduction

Advances in mass spectrometry over the last 65 years have allowed the routine application of the noble gas isotopes as geological tools (e.g. Aldrich and Nier 1948b; Reynolds 1956; Lynch and Kay 1981; Sano and Wakita 1987; Stuart *et al.* 2003; Sano *et al.* 2008). Many of these applications pertain to constraining the timing or duration of geological events. Vast amounts of fundamental information regarding the Earth and Solar System can be obtained via these methods. Advances have now made obtaining insightful data possible for the non-specialist, propelling their usefulness. This chapter aims to provide a historical perspective of noble gas mass spectrometry, highlighting some key advances and how they have contributed to the current level of knowledge. This will be followed by a review of current practices.

4.2 Historical perspective

Development of mass spectrometry began before the Second World War (Thomson 1913; Dempster 1918; Alvarez and Cornog 1939) but, arguably, the most important advances in technology and performance began in the late 1940's. A. O. Nier designed and built a mass spectrometer that first incorporated an electron impact source on which many modern designs are based (Nier 1947). This landmark development allowed the first studies into the isotopes of the noble gases; Xe (Reynolds 1956; Reynolds and Lumpkin 1980), Ar (Reynolds 1956; Takaoka 1976) and Ne (Takaoka 1976) among other isotopes as well as into the variation of ^{3}He/^{4}He ratios of natural materials (Aldrich and Nier 1948b).

Reynolds (1956) developed techniques necessary for static mass spectrometry, where the mass spectrometer is isolated from the pumps during analysis. This was required for isotopic analysis of noble gas isotopes in rocks and minerals, to achieve this the valve had to be both leak proof and able to withstand high bakeout temperatures (Alpert 1951). In the late 1970's a new electron impact source was developed by Baur and Signer which had improved mass discrimination with respect to pressure than Nier-type sources. This was used by Hohenberg (1980) in a mass spectrometer that also incorporated a 17-stage Allen-type electron multiplier operated in pulse counting mode. This led to improved mass discrimination and higher levels of sensitivity but despite these capabilities usage of this type of source is uncommon. Lynch and Kay (1981) further refined this design and described the performance of their Micromass 3000 dual collector mass spectrometer for simultaneous measurement of ^{3}He and ^{4}He. They reported improvements in attainable mass resolution of 2000 but were limited to an operating resolution of 600-1000. This allowed resolution of $^3He^+$ from HD^+-H_3^+ doublet without need for interference corrections.

Sano and Wakita (1987) used the VG 5400 dual collector mass spectrometer to make high precision measurements of helium isotopes in terrestrial rocks and minerals. It is an all-metal, 27 cm radius 90^o extended geometry mass spectrometer. They reported detection limits for ^{3}He of 3 x 10^{-14} ccSTP which was 25 times lower than previous systems. Stuart and Turner (1992) used a MAP 215-50 dual collector mass spectrometer, introduced in 1987, to make high precision abundance and isotopic composition measurements of noble gases in ancient terrestrial fluids. It is an all-metal, 15 cm radius 90^o extended geometry magnetic sector mass spectrometer equipped with a Faraday and an electron multiplier detector. They reported precision of ± 1% and reproducibility of ± 2.5% (at 1σ) of the He isotopic ratio, which was a significant improvement over previous systems (for definitions and further discussion of precision and reproducibility see sections 5.5 and 5.6). Since then these two machines have produced the majority of noble gas isotope analyses of minerals and fluids.

In 2009 - 2011, new multicollector noble gas mass spectrometers were introduced; HELIX-SFT (GV instruments, then ThermoScientific) and Noblesse (Nu instruments) (Sano *et al.* 2008; Coble *et al.* 2011). This has led to, among other things, improvements in measuring He isotopes in sample sizes three orders of magnitude smaller than the original instruments. Sano *et al.* (2008) reported high sensitivity and high precision measurements of helium isotopes on 2 x 10^{-7} ccSTP HESJ with an estimated uncertainty of 0.3% at 2σ.

4.3 Principles of noble gas mass spectrometry

4.3.1 Introduction

Noble gas mass spectrometers typically consist of three components; (1) an ion source, (2) a mass filter (magnet), and (3) a collector (Figure 4.1) (Herbert and Johnstone 2003). The standard configuration consists of an electron impact source, a magnetic sector filter, and detection using Faraday cups and/or secondary electron multipliers (SEM) (Reynolds

1956, Hohenberg 1980, Lynch and Kay 1981, Sano and Wakita 1987, Sano *et al.* 2008). The analyser is kept at ultra-high vacuum (1 x 10^{-9} torr) using combinations of turbomolecular and ion pumps. Control of the ion source and multiplier sources is achieved via a software/hardware interface.

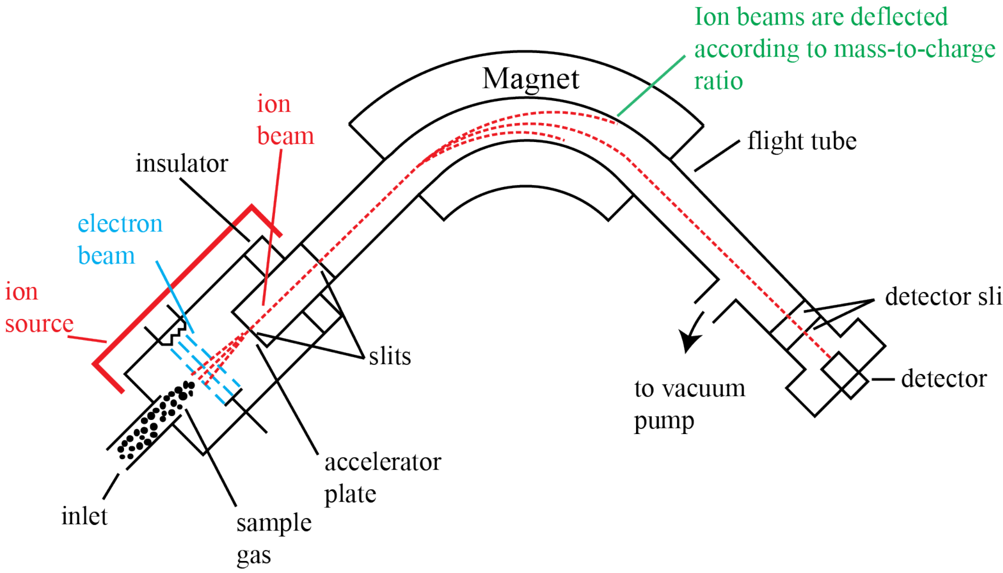

Figure 4.1. Simplified schematic of a noble gas mass spectrometer layout showing details of the three individual components; (1) the ion source, (2) the magnetic analyser and (3) the ion collector (detector) and the path of the ion beam.

Analysis is usually performed in *static* mode where all gas vacuum pumps are isolated prior to analysis (Reynolds 1956), dramatically increasing sensitivity and allowing for analysis of smaller samples. The strength of the magnetic field is monitored by a Hall probe and magnet field control for peak jumping and data collection is typically done via dedicated software.

4.3.2 Electron bombardment ion sources

Ionization in a Nier-type ion source occurs when accelerated electrons pass close to, or through a neutral atom, causing another electron to eject from its electron cloud. This is due to large fluctuations in the electric field around the neutral molecule, which induces ionization and fragmentation (Robinson *et al.* 2005). The electrons are produced by thermionic emission via a tungsten filament operated at ~2.5 A (~3000°C). The electron beam passes through the ionization volume towards a trap that controls the emission of electrons from the filament. Two small magnets of opposite polarity are fixed around the filament and electron trap creating a small magnetic field, which causes the electrons to spiral towards the trap and contains them within a beam. The filament current is varied in order to maintain constant intensity and therefore not effect sensitivity and mass discrimination (Nier 1947). An ion repeller plate positioned behind the electron beam, and a series of focussing plates, then accelerate the ions from the ionisation region and focus them into a collimated ion beam. (Figure 4.2) The electron beam intensity within the source is monitored by the trap current, and is typically kept between 10 and 800 μA (Nier 1947).

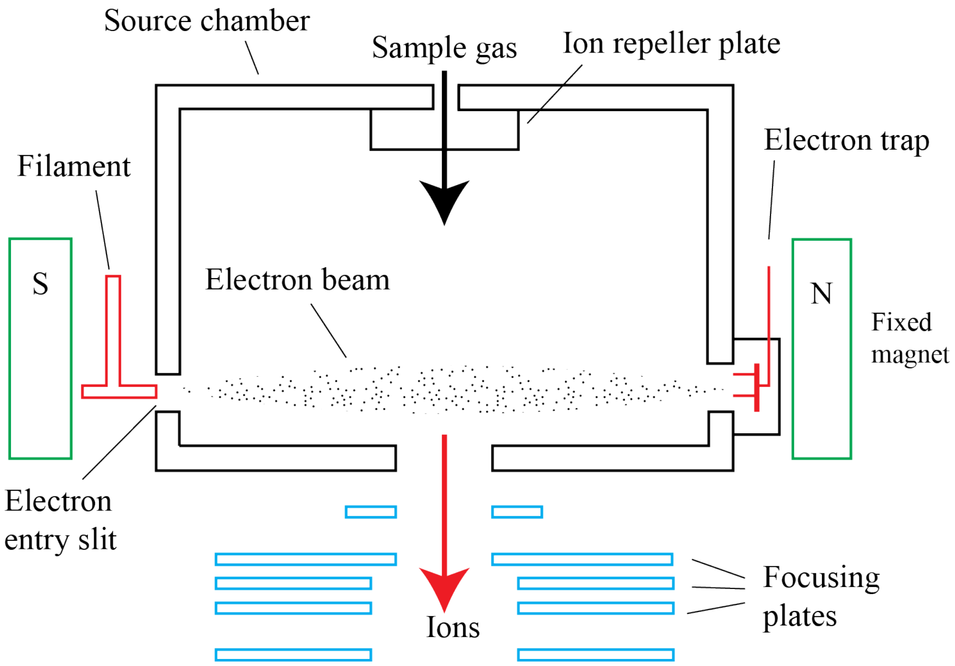

Figure 4.2. Schematic of a Nier-type ion source showing the sample gas inlet, electron beam flow and direction of ion beam exit.

4.3.3 Mass separation using sector magnets

The magnetic sector of the mass spectrometer separates ions according to mass-to-charge (m/z) ratio. Most ions attain a single positive charge during ionization and have the same kinetic energy because they were accelerated with the same potential voltage. This is exploited by the electromagnet to separate ions. The pole pieces of the magnet are carefully constructed and positioned in order to create a homogeneous magnetic field with lines that lie perpendicular to the flight path of the ions (Herbert and Johnstone 2003). Consequently ion flight paths are deflected and the direction of travel becomes circular rather than linear. The degree of deflection depends on m/z and the strength of the magnetic field. Simply, heavier ions are deflected less than lighter ions. The field strength of the magnet is altered in order to ‘steer’ the ion beam of the desired mass in to the detector(s) (Herbert and Johnstone 2003) (Figure 4.1).

4.3.4 Ion detection

Faraday and electron multiplier detectors, (operated in analogue or ion counting mode), are utilised in the measurement of helium isotopes. ^{3}He is typically 10^5 - 10^8 times lower in abundance than ^{4}He in terrestrial gases and therefore requires greater signal amplification (Hohenberg 1980; Ozima and Podosek 2002). Faraday detectors (Nier 1947) are used for ^{4}He and consist of a metallic cup which is located behind a collector slit (Figure 4.3). Ion beams pass through the collector slit and impinge upon the cup. The ions are neutralised by electrons that travel from a ground state to the cup via a resistor. The resulting voltage difference is measured.

Electrostatic analysers (ESA) act as filters that only allow ions with fixed m/z to pass. This narrows the measurement range and ensures that potential interferences are eliminated (Herbert and Johnstone 2003).

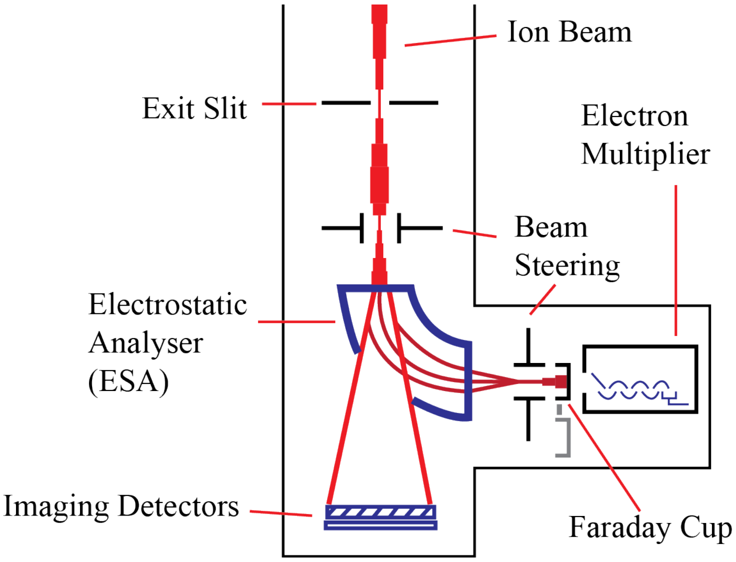

Figure 4.3. Faraday collector schematic showing direction and focussing of ion beam onto faraday cup.

Electron multipliers may be discrete dynode (e.g. Balzers SEV-217) or continuous dynode (e.g. Photonis Channeltron®) which can be operated in pulse counting or continual counting mode. In each case an ion-counting electron multiplier detector consists of surfaces which when struck by incoming ions emits several electrons in a process called secondary emission. An electrical potential is applied between each dynode or along the entire surface of the continuous dynode which causes the emitted electrons to accelerate, impact and release yet more electrons. As this process is repeated a cascade of electrons are emitted, and amplified signals are ultimately detected by an anode (Allen 1939, 1947) (Figure 4.4).

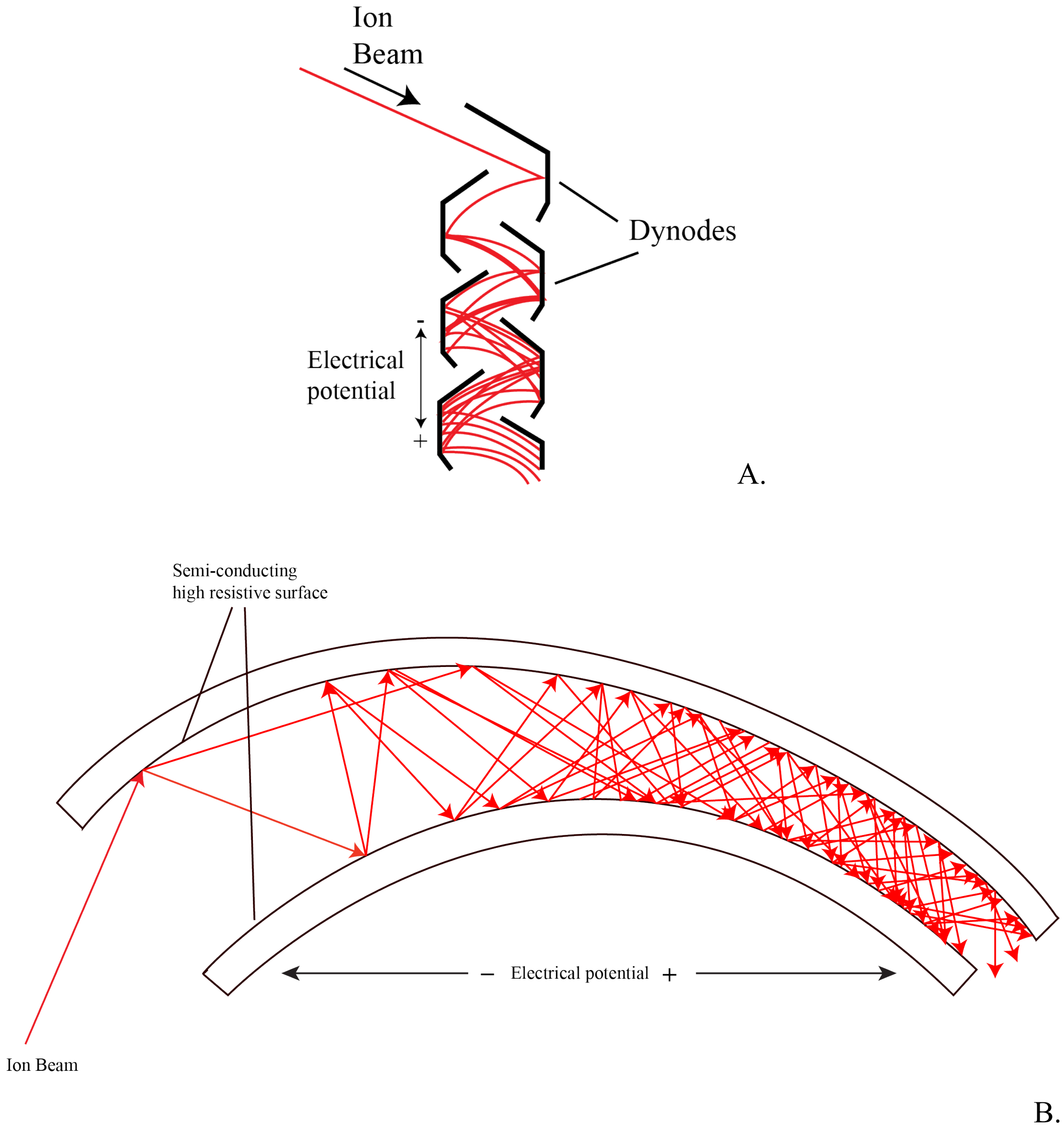

Figure 4.4. A. Discrete dynode model of electron multiplier. B. A continuous dynode model in which the entire inner surface is coated with a semi-conducting high resistive material. In both cases an incident ion beam strikes the multiplier which then emits secondary electrons which accelerate towards the next stage causing further emission. The signal is multiplied as the electrons cause a cascade.

4.4 Gas extraction and purification

The method of extraction of He from minerals depends on the origin of the gas and the purpose of the study. Helium in melt/fluid inclusions is extracted by *in vacuo* crushing. Gas in mineral lattices is released via heating, either by a resistance furnace or by a laser.

There are several different designs of *in vacuo* crusher. All are made 'in-house' rather than being manufactured to a standard design (e.g. Kurz 1982; Staudacher *et al.* 1986). Crushing involves loading sample grains into a vessel, (e.g. stainless-steel pot), which is housed in a sealed high vacuum chamber. The grains are then crushed using a piston, or stainless-steel ball bearing (Staudacher *et al.* 1986; Stuart *et al.* 1995; Scarsi 2000). The released gases are introduced directly into the purification line. Care has to be taken to avoid releasing any matrix sited gas by over-crushing (Blard *et al.* 2008).

Furnace heating of samples is typically performed in a radiatively-heated crucible manufactured from molybdenum or tantalum (e.g. Zimmerman *et al.* 2012). The samples are loaded into packets of metal foil which are housed in a suitable holder. They are dropped individually into a tantalum liner tube which sits inside the crucible. The samples can be heated incrementally from temperatures of ~400 ^{o}C to ~1800 ^{o}C in order to progressively release gas from different sites within the rock or mineral (Figure 4.5).

Laser heating has long been used in geochemistry, (e.g. Megrue 1967), and is becoming increasingly common for several reasons; smaller sample amounts are required, blank levels are lower and total heating time is smaller all compared to resistance furnaces and are target specific.

The type of laser employed for heating depends on the aim of the experiment and of mineral type. Several designs of laser exist each with differing wavelengths. The main types are; diode- (808nm), CO_2- (10.6 μm), Nd:YAG (1064 nm) and excimer (variable), (e.g. Colin *et al.* 2013; Foeken *et al.* 2006; House *et al.* 2000; Barfod *et al. in press*).

Sample heating is done in a laser cell kept at UHV conditions. Sample grains can be prepared for heating in several ways but the two most common are; loaded as monogranular layers into wells in a copper pan with a protective cover slip made of suitable material (e.g. KBr for CO_2 laser or quartz glass for diode laser), and placed on top or contained within packets constructed of thermally conductive foil such as Pt, Pd or Nb (House *et al.* 2000; Reiners *et al.* 2002; 2003). The laser light is transmitted through a window into the laser cell with the window material dependant on the wavelength of laser. Nd:YAG, excimer and other near visible lasers use silica glass and Diode lasers typically use sapphire glass. The light emitted from CO_2 lasers couples with oxygen bonds and so neither silica nor sapphire are suitable, therefore ZnSe or ZnS windows are required

(McIntosh and Heizler 1994). In all cases grains are heated to their melting point when the crystal lattice breaks down and the gases are released (Figure 4.6).

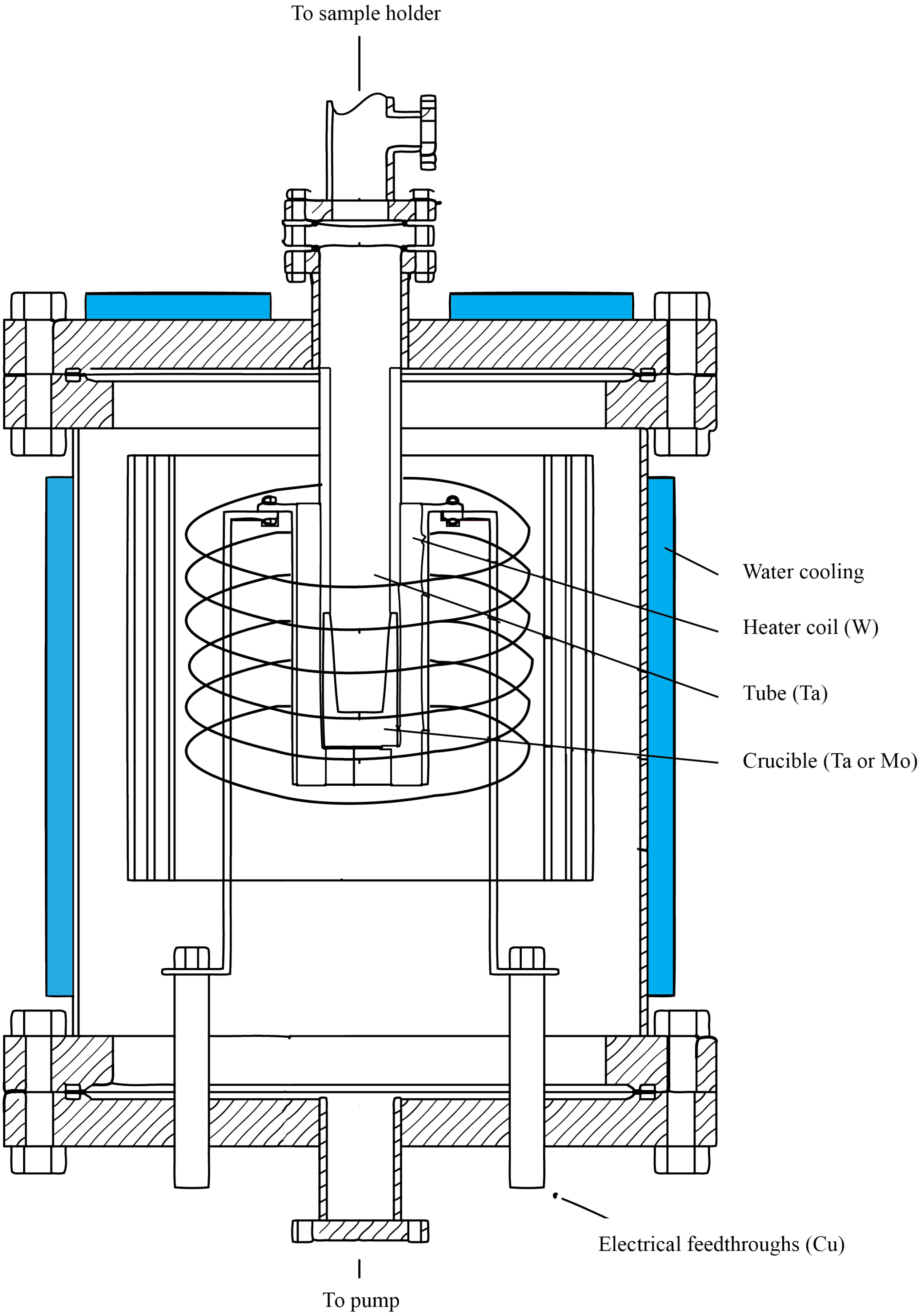

Figure 4.5. Schematic of resistance furnace. Sample wrapped in metal foil is dropped from a sample holder

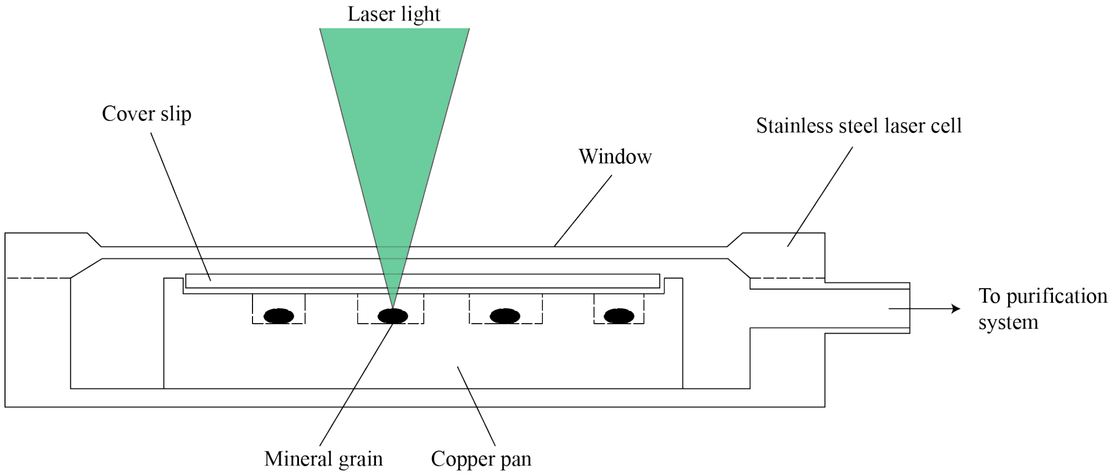

Figure 4.6. Vacuum pumped laser cell containing a copper planchette loaded with sample grains. As the grain is melted by the incoming laser light it releases all gas which travels to the purification system.

Noble gases are typically purified in a stainless steel UHV line (e.g. Takaoka 1976). The extracted gases are exposed to ZrAl alloy getters (SAES® GP50). In order to trap active gas species, (CO, CO_2, N_2, O_2, water and hydrocarbons) they are operated at 250 ^oC, whereas getters operated at room temperature trap hydrogen. A Liquid-N_2 cooled (-196 ^oC) charcoal finger is also used to trap heavy species of noble gas (Ar, Kr and Xe).

Extraction lines are kept at UHV by employing two types of pumps; turbo molecular (turbo) and sputter-ion pumps (ion pumps).

Usually turbomolecular pumps, backed-up with ion, diaphragm or rotary pumps, are used to achieve UHV conditions (10^{-7} mbar) (Hablanian 1990). Turbo pumps have multiple stages of compression consisting of several rotor/stator pairs mounted in series (Figure 4.7). Gas molecules captured at the inlet stage are forced into the lower stages and successively compressed to the level of the diaphragm or rotary pump pressure. The rotors have angled blades which impact the molecules which are adsorbed to the surface. After a finite length of time the molecules leave with transferred kinetic energy. This momentum carries the molecules through the holes in the stators which in turn lead to the next pair and further collision/adsorbtion. Eventually the molecule arrives at and leaves via the back-up pump outlet (Harris 1997). Turbomolecular pumps are effective at pumping heavy gas species (CO_2, CO, CH_4, Ar) but are less efficient at pumping light species (H, N, He). This is due to the average speed of these molecules at STP conditions. For example a rotor travelling at 60,000 rpm with a blade diameter of 7.5 cm equates to the blade tip travelling at 236 ms^{-1}. The average speed of a N molecule at STP is 470 ms^{-1} and H under the same conditions is 1900 ms^{-1} (Harris 1997). This means that lighter molecules will pass through the rotor/stator pairs without being struck and increases the probability of back-diffusion of the gas into the extraction system (Harris 1997).

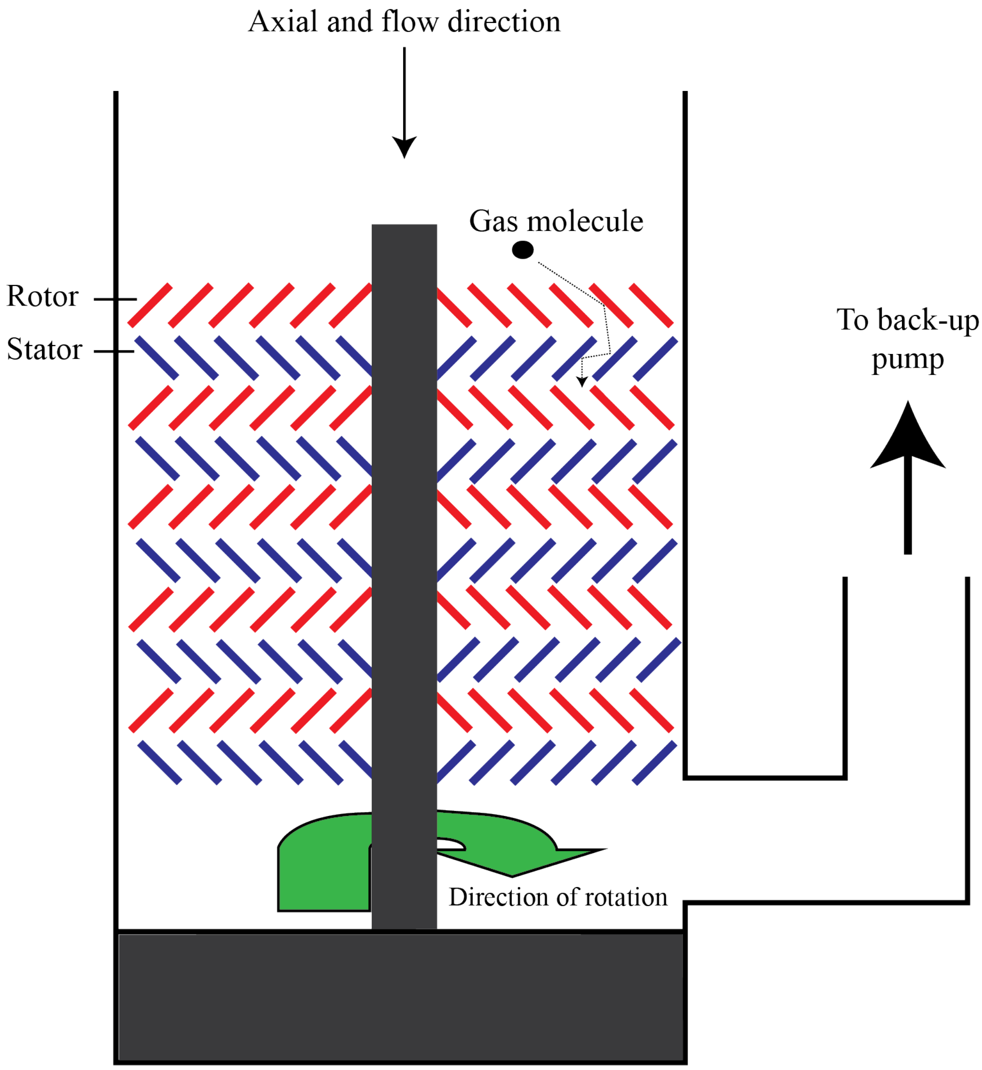

Figure 4.7. Schematic of a turbo molecular pump. The gas molecule enters via an inlet and travels along the axial/flow direction before being struck by a rotor blade. The molecule continues downward being successively compressed by each rotor/stator pair before finally being evacuated to the back-up pump.

Ion pumps typically consist of two flat rectangular cathodes constructed of titanium with a stainless steel anode between them made up of several open-ended tubes (this configuration is known as a Penning trap) (Harris 1997) (Figure 4.8). This is positioned inside the pump body and is surrounded by a magnetic field. The anode can be provided with an electrical potential of 3 to 7 kV and the cathodes kept at ground potential. Electrons are produced which ionise the incoming gas molecules which in turn are accelerated towards the cathodes where they become embedded or sputter titanium onto the pump walls. This sputtered titanium acts as a getter which removes the gas via chemisorption and physisorption (Hablanian 1990). In this way the ion pump is able to effectively evacuate light gas species such as H, He and N. Under ideal conditions ion pumps are capable of reaching pressures as low as 10^{-11} mbar.

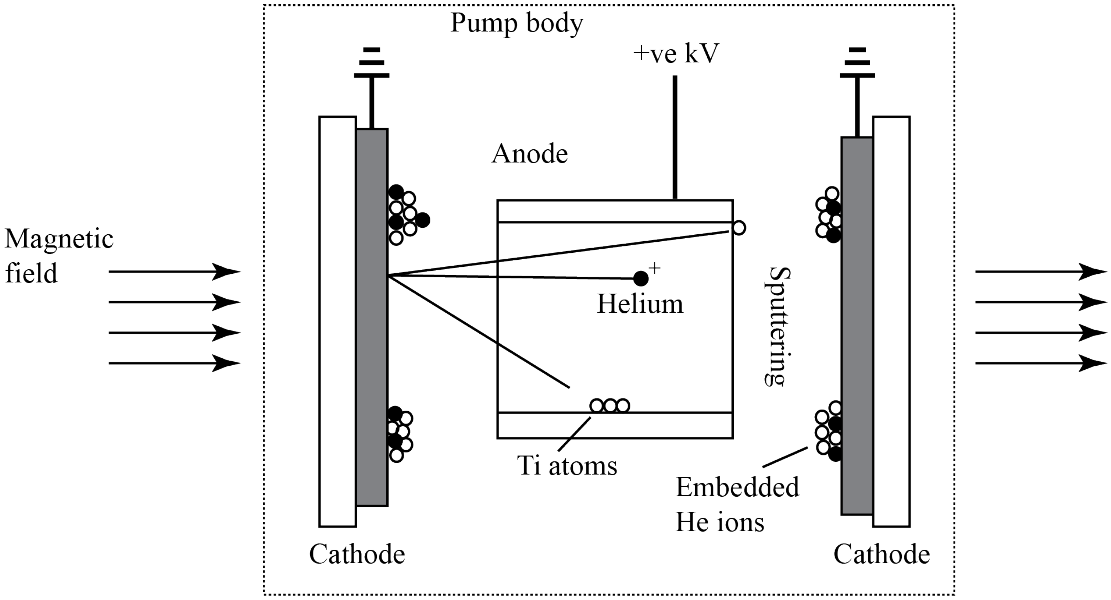

Figure 4.8. Schematic of an ion pump. Helium atoms become ionised and are embedded in the cathode.

In Triode ion pumps the cathodes are slotted which increases inert gas pumping speeds. These slots increase the amount of sputtering that occurs due to an increase of glancing incidence of ions so that gases such as Ar are more likely to be permanently buried (Harris 1997).

Chapter 5. Initial characterisation of ThermoScientific HELIX-SFT and comparison with Mass Analyser Products 215-50

5.1 Introduction

This chapter describes the ThermoScientific HELIX-SFT mass spectrometer and presents data detailing its performance. It is compared with its predecessor the Mass Analyser Products (MAP) 215-50 in order to determine the extent that it provides more precise and reproducible He isotope data.

5.2 HELIX-SFT description

The HELIX-SFT (Figure 5.1) is a static vacuum mass spectrometer specifically designed for *simultaneous collection* of helium isotopes. It is an all-metal, 35 cm radius 120° extended geometry magnetic sector mass spectrometer. The geometry combines ion optic performance with two-direction focusing and high dispersion. It has an internal volume of ~1376 cc. It is evacuated to ultra-high vacuum (UHV) (~10^{-10} mbar) using a 40 L/s ion pump and a 70 L/s turbo molecular pump supported by a two stage diaphragm pump.

Figure 5.1. SUERC ThermoScientific HELIX-SFT mass spectrometer.

It is equipped with a Nier-type electron bombardment bright source with *y* and *z* focussing with a reported sensitivity for He of 2 × 10^{-4} A/Torr at 800 μA trap current. All source parameters (HV, focus, electron volts, ion repeller, trap and y & *z* steering) are driven by MAT 253 electronics and controlled by ThermoScientific Imhotep software. It was delivered with a SAES® NP10 mounted on the source in order to capture active gas species.

The electromagnet pole pieces are fabricated from high purity (minimum 99.9%) soft iron. This produces a homogeneous magnetic field and low residual field memory. The control loop for the field comprises a temperature controlled Hall probe.

A Balzers SEV-217 copper beryllium ion counting discrete dynode electron multiplier is positioned for low mass. A 90° energy filter is used to improve abundance sensitivity, which is the measure of the contribution of the peak “tail” of a major isotope with a certain mass-to-charge (m/z) ratio to an adjacent m/z ratio. Ultimately this contribution is dependant on the resolving power of the instrument (Inczédy *et al.* 1997). The high mass analyser is an electrically suppressed Faraday cup with an amplifier circuit equipped with a 10^{11} Ω resistor. The magnet, data acquisition and collector are driven by ThermoScientific TRITON electronics.

To date there is only one detailed published description of the instruments’ performance (Sano *et al.* 2008) and one conference abstracts (Mabry *et al.* 2010) that report the reproducibility of isotope ratio determinations.

5.3 Characterisation of ThermoScientific HELIX-SFT

An all-metal gas line for purifying aliquots of standard He (HESJ, Matsuda *et al.* 2002 and Standard Air) was constructed. It is based around an eight-port manifold (Figure 5.2). Eight Varian® (9515014) valves allow isolation of any part of the system. It has inlets for both air and HESJ calibration bottles (each is 5 L in volume and equipped with 0.1 cc pipette), a 70 L/s Pfeiffer HiCube turbomolecular pump and a 30 L/s triode ion pump and two SAES® GP50 getters and a liquid N_2-cooled charcoal finger which are used to purify the gas before inlet into the mass spectrometer.

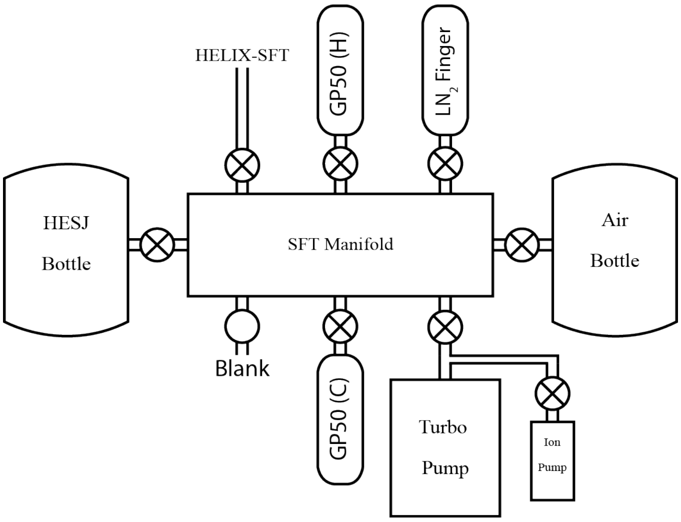

Figure 5.2. Schematic of the gas purification line used as part of the HELIX-SFT system.

5.3.1 Peak shape and ion beam coincidence

Initial effort was put into optimising the $^4He^+$ peak shape on the high mass Faraday detector and the $^3He^+$ peak shape on the low mass Secondary Electron Multiplier (SEM). Manually altering the position of the sector magnet pole pieces and fine-tuning the source parameters achieved this. Figure 5.3 shows the peak shapes and coincidences of ^4He (Faraday) and ^3He (SEM).

Initially short-term peak drift was an issue. Movement of peak positions did not correlate directly with laboratory temperature fluctuations (18.5 – 21.5°C). However, airflow from the laboratory air conditioning unit, across the Hall probe did have some effect. The Hall probe was insulated and this reduced the mass scale drift to 0.002 to 0.004 mass units over a 24 hour period.

The position of the sector magnet was monitored relative to the flight tube of the instrument. It was discovered that magnet was not level and required repositioning. Once complete, mass shifts were reduced to 0.001 mass units and negligible movement of beam coincidence was observed over 24 hour periods.

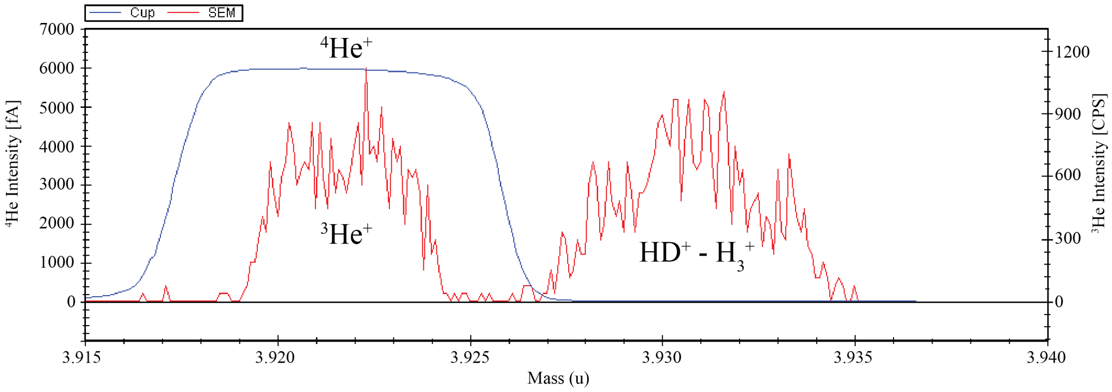

Figure 5.3. Scan showing peak shapes, separation of HD^+-H_3^+ from $^3He^+$ and coincidence of $^4He^+$ (blue) and $^3He^+$ (red) peaks. Intensity of ^4He in fA is shown in the left Y-axis, ^3He in CPS is shown on the right. 0.3cc HESJ was used; 1.4×10^{12} atoms of ^4He and 3.2×10^7 atoms of ^3He were present in the mass spectrometer.

5.3.2 Isobaric interferences

Precise and accurate ^3He measurements require the ability to separate $^3He^+$ and HD^+ (Figure 5.3). The ability to distinguish two peaks of slightly different mass-to-charge ratios, is the resolving power (R):

$$R = m/\Delta m \qquad (5.1)$$

where Δm is the minimum peak separation that allows the distinction of two ion species. The HELIX-SFT has a nominal resolution of >400 for the Faraday detector and >700 for the multiplier, both calculated at 10% valley (http://www.thermoscientific.com/ecomm/servlet/Productsdetail_11152_L10676_98068_12811542_-1). After tuning for maximum sensitivity the resolution was calculated to be 286 for the Faraday detector at 95% peak and 635 for the multiplier at 95% peak. Figure 5.3 shows how this allowed the complete separation of $^3He^+$ from the HD^+-H_3^+ doublet.

Initial scans at mass 4 demonstrated that $^{12}C^{3+}$ (4.0 amu) formed an isobaric interference at $^4He^+$ (4.002 amu) (Figure 5.4). The initial level of $^{12}C^{3+}$ was ~5 fA and was not resolvable from $^4He^+$ on the multiplier.

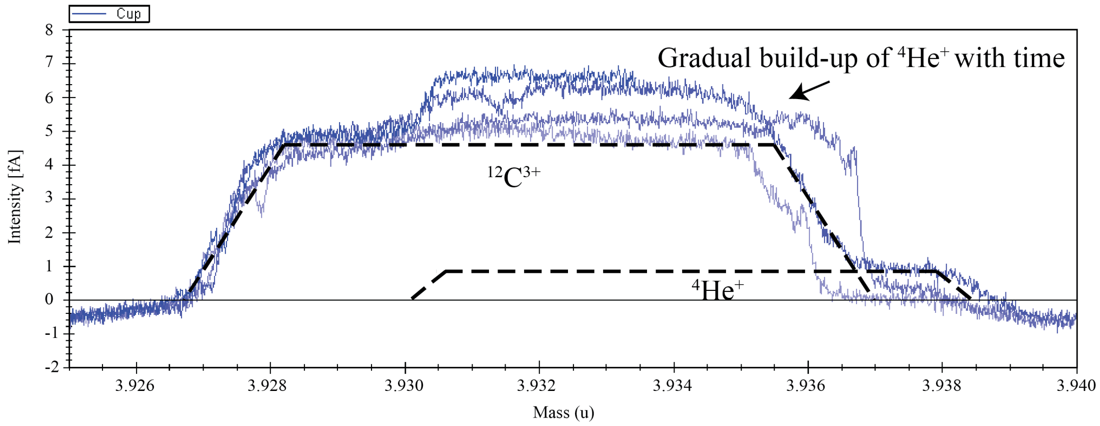

Figure 5.4. The coincidence of $^{12}C^{3+}$ and $^{4}He^{+}$ ion beams on the Faraday detector over 10 minutes during static scan.

The pumping capacity of the SAES® NP10 getter on the mass spectrometer source block was not sufficient to remove the $^{12}C^{3+}$. A SAES® GP50 getter was added to the static volume of the instrument. Operating the NP10 getter at 125°C and the GP50 at room temperature, $^{12}C^{3+}$ was reduced from 5 to 2 fA. The Brooks Micro-ion® 355 ion gauge, fitted to the pump manifold of the instrument was discovered to be the source of $^{12}C^{3+}$. The gauge was deactivated and the level of $^{12}C^{3+}$ dropped to ~0.0125 fA and had to be measured on the SEM (Figure 5.5).

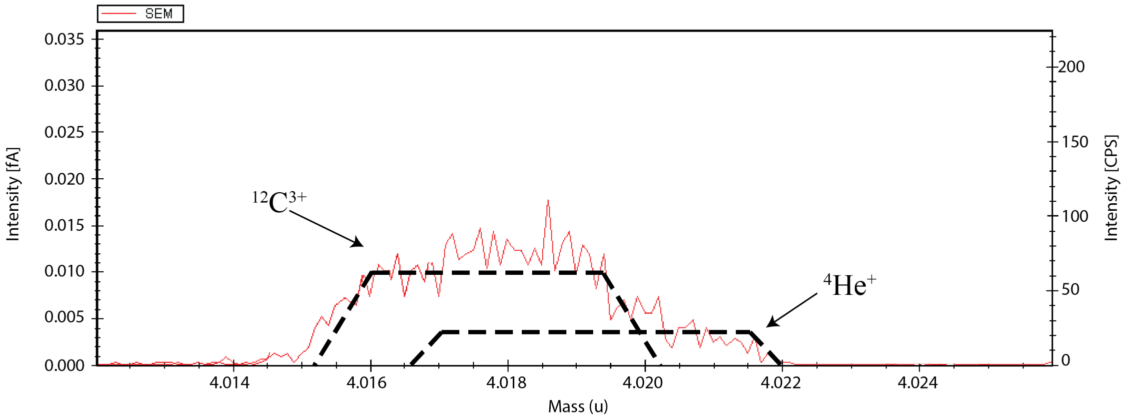

Figure 5.5. $^{12}C^{3+}$ background measured on the SEM after installation of GP50 getter on source block and deactivation of the ion gauge.

5.3.3 Determining optimum analysis parameters

The final phase of the mass spectrometer set-up was to establish the optimum parameters for measuring He isotopes. Two parameters had the largest effect on the quality of the data; integration time and the number of measurement cycles. The integration time is the period over which the ion beam intensity is measured. The number of cycles determines how many times this measurement is made with short pauses (5 ms) in between. The number of cycles equates to the number of data points that will be collected and used to extrapolate back to time of gas inlet (t=0).

The Imhotep software allows the selection of pre-set integration times. The maximum selectable time is 67.11 seconds. It resulted in the lowest within-run uncertainty for both He isotopes. Reducing the integration time has a more significant effect on the uncertainty associated with ^{3}He measurements than ^{4}He. Integration time of 33.55 seconds results in a ~2-fold increase of both the within-run uncertainties, (~1%) and reproducibility uncertainty (~0.95%) (Figure 5.6; Appendix 3, Table A3.2).

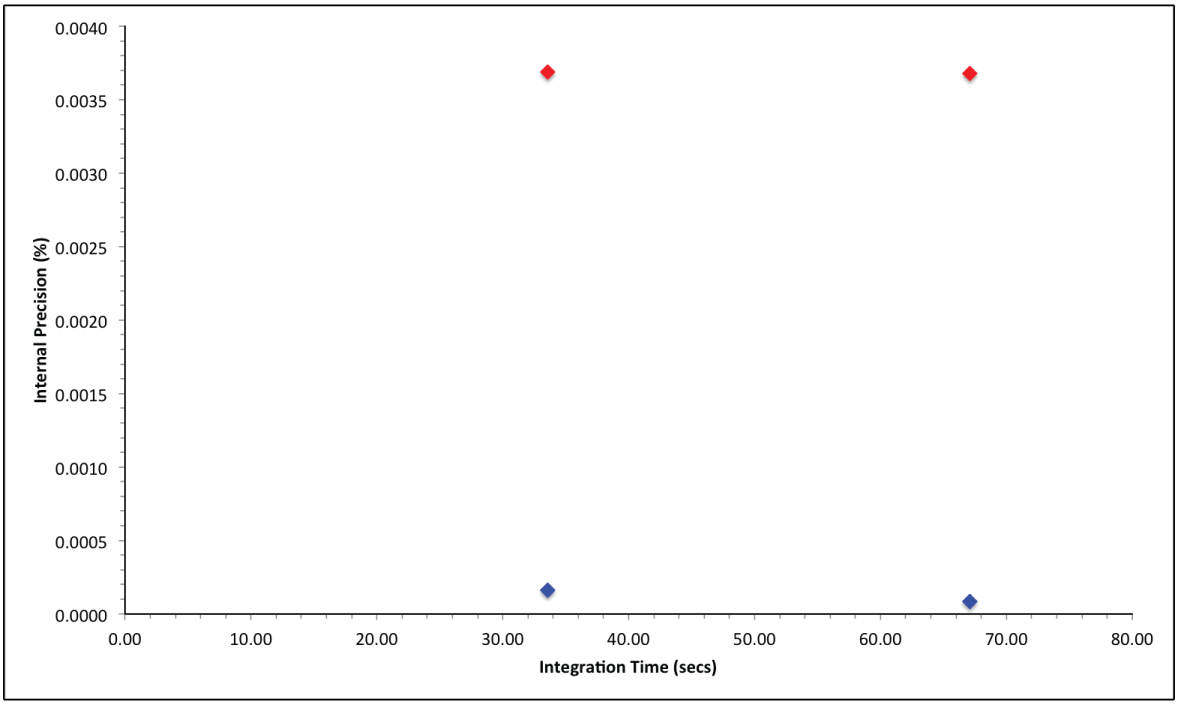

Figure 5.6. Plot of change in internal precision with time of integration. All measurements were performed over 20 cycles. Red diamonds represent ^{3}He, blue diamonds represent ^{4}He. All uncertainties are 2σ.

To determine the optimal number of collection cycles, data was collected from a set of 100 cycle experiments (Figure 5.7). The last data points were sequentially deleted and the uncertainty at inlet time was recalculated. In general increasing the number of cycles improves the uncertainty of the ^{3}He measurement. As the ^{3}He measurement exerts the largest influence on the uncertainty of the ^{3}He/^{4}He and a balance of uncertainty and analysis time must be struck, it was decided that the optimal number of cycles was 20. Beyond 50 cycles the uncertainty in ^{4}He measurement increases to a point where it affects the uncertainty of the ^{3}He/^{4}He.

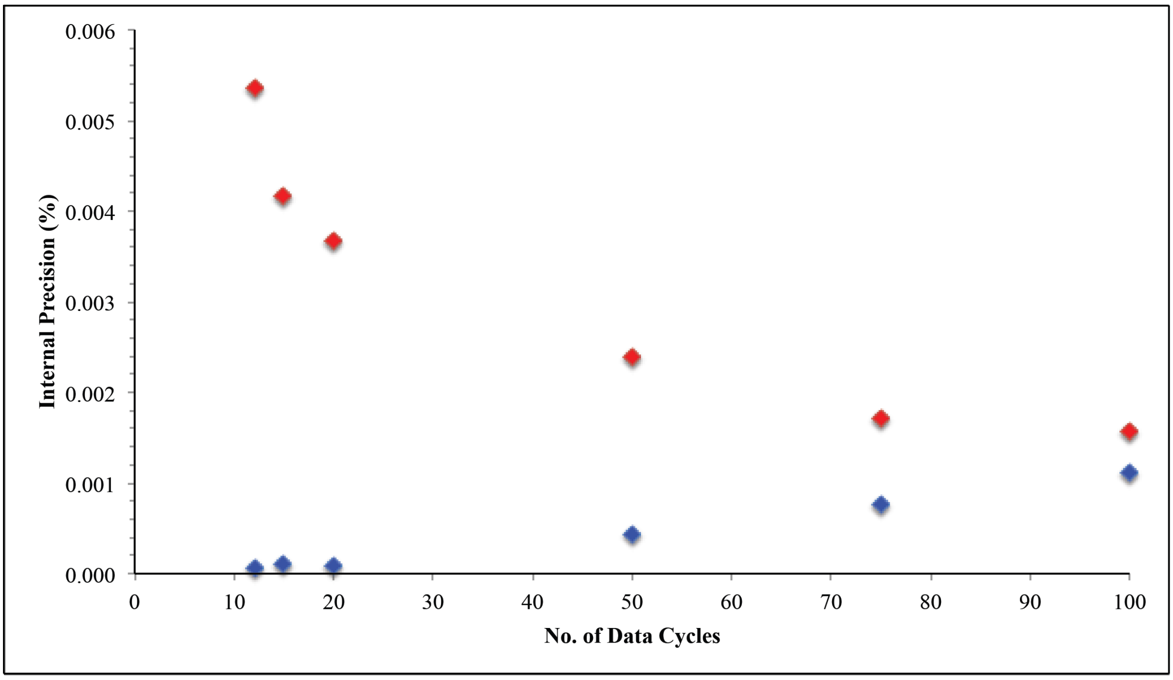

Figure 5.7. Plot of change in internal precision with number of data cycles. All measurements were carried out with an integration time of 67.11 seconds. Red diamonds represent ^{3}He, blue diamonds represent ^{4}He. Uncertainties reported are 2σ.

5.4 Performance comparison

In order to compare the HELIX-SFT with the MAP 215-50 I undertook a series of measurements of the HESJ (Helium Standard of Japan) (^{3}He/^{4}He = 20.63 ± 0.10 R_a) (Matsuda *et al.* 2002).

5.4.1 MAP 215-50 mass spectrometer

The MAP 215-50 (Figure 5.8) is a dual collector static vacuum mass spectrometer designed to be operated in *peak jumping* mode. It is an all-metal, 15 cm radius 90^o extended geometry magnetic sector mass spectrometer. It has an internal volume of ~1300 cc. UHV conditions are obtained by a 30 L/s triode ion pump.

It is equipped with a Nier-type electron bombardment ion source with *y* steering and a reported sensitivity for He of 5 x 10^{-5} A/Torr. The source is equipped with a SAES® GP50 getter pump and a liquid-N_2 cooled charcoal finger. All source parameters (HV, focus, electron volts, ion repeller, trap and *y*-bias), are driven via GV Instruments® electronics and controlled by GV instruments® Noble Ion Vantage software.

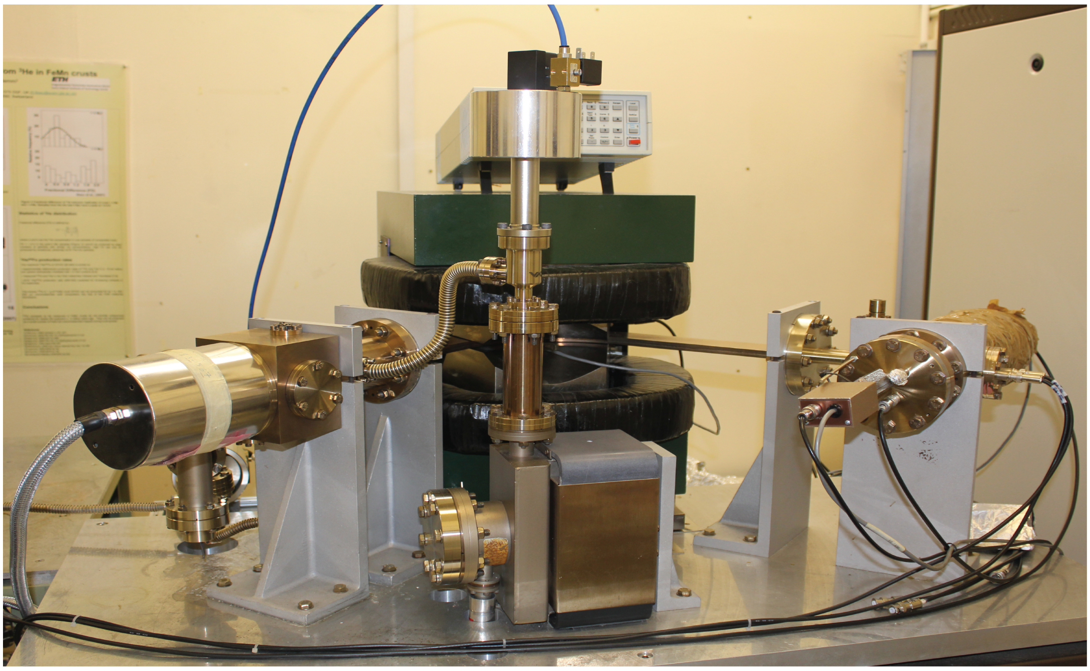

Figure 5.8. MAP 215-50 mass spectrometer at SUERC.

The electromagnet is fabricated from high purity (minimum 99.9%) soft iron. The control loop for the field comprises a temperature controlled Hall probe. The mass spectrometer is fitted with a low mass analyser Photonis Channeltron® electron multiplier operated in pulse counting mode. An adjustable slit is used to achieve a resolution of 600 at 10% valley to allow separation of interferences on $^3He^+$ of HD^+, necessary for ^3He measurement. The high mass analyser is a Faraday cup with a 10^{11} Ohm resistor. It has abundance sensitivity several orders of magnitude higher than that of the SFT. It is connected to a gas purification-inlet line shown in Figure 5.9.

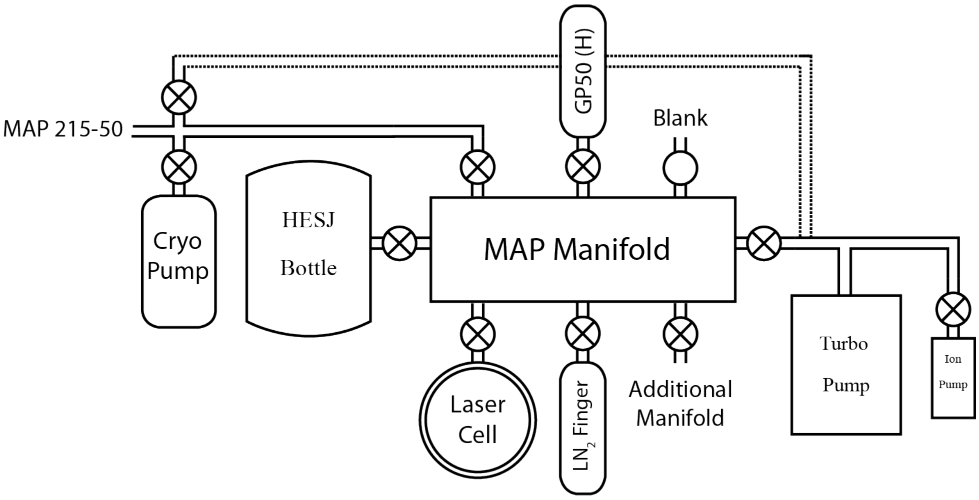

Figure 5.9. Schematic of the gas purification line on the MAP 215-50 system. During purification of aliquots of HESJ the laser cell, second manifold, cryogenic pump and pumps are isolated.

5.4.2 Analytical procedures

Analyses on the HELIX-SFT were made on aliquots of 4.86×10^{11} atoms of ^{4}He. Helium isotopes were measured simultaneously in 20-cycles. An equilibration time of 30 seconds was allowed prior to data collection. Each data collection cycle had an integration time of 67.11 seconds with a settling time of 5 seconds between cycles. Baselines were determined in separate experiments with integrations of 67.11 seconds and the offset was manually entered into the detector set-up parameters. This baseline measurement is then applied to all consequent measurements. The total time for data collection was ~1500 seconds. All parameters of analysis and data regression were controlled via an embedded PC running ThermoScientific Imhotep software. All data was regressed back to inlet time.

The analyses on the MAP 215-50 were made on 1.85×10^{11} atoms of ^{4}He from HESJ. Helium isotopes were measured in peak jumping mode for 10-cycles. As with the HELIX-SFT an equilibration time of 30 seconds was allowed prior to each analysis. Each data and baseline collection cycle comprised of ten 10 seconds integrations, with a settling time of 15 seconds between cycles. The total time for data collection was ~ 3600 seconds and includes a 5-cycle run of ^{20}Ne data collection and measurements of baselines. All analysis parameters were controlled via an embedded PC operating National Instruments® Labview software and data regression is performed on the same PC using in-house ‘Regression’ software.

Analyses of HESJ He on the HELIX-SFT were carried out over a period from late February to mid-March 2011 with the aim of achieving the best within-run uncertainty and run-to-run reproducibility. The parameters that gave the best quality of data were as described above. In order to make as direct a comparison as possible the running parameters of the MAP 215-50 were altered in order to match those of the HELIX-SFT. A set of analyses (n = 11), were carried out in January 2013 with the MAP 215-50 with integration times changed to ten 6.711second measurements per cycle. This demonstrated that the uncertainties did not change significantly from the standard (ten 10 second measurements per cycle) analysis parameters and so it was decided to use analyses performed with the typical integration times. These analyses (n = 16) were carried out from early September to early October 2012.

5.5 Results

Reporting of the uncertainties associated with the measurements of each isotope, and ^{3}He/^{4}He, allows a direct comparison between mass spectrometers. Here I focus on the reproducibility and within-run uncertainty. The reproducibility of multiple measurements is used to quantify how well the mass spectrometer is able to replicate measurements of the same amount of He. Within-run uncertainty is a measure of the precision of a single measurement. Both have bearing on the precision of cosmogenic ^{3}He age determinations (see section 6.2).

The reproducibility and within-run uncertainties for the HELIX-SFT and MAP 215-50 is summarised in Table 5.1 and Figure 5.10. The complete datasets are presented in Appendix 3 (Tables A3.1 and A3.3). All uncertainties for both instruments were calculated from the raw data transferred to Excel. The reproducibility of each measurement was calculated from the average values and standard deviation of all data. Within-run uncertainties were calculated from average values of all data. The HELIX-SFT has significantly lower within-run uncertainties associated with ^{4}He, ^{3}He and the ratio compared to the MAP 215-50 (Table 5.1).

HELIX-SFT	^{3}He/^{4}He	^{4}He	^{3}He
Reproducibility	0.78%	0.27%	0.78%
Within-run uncertainty	0.37%	0.01%	0.37%
MAP 215-50			
Reproducibility	3.60%	3.18%	2.65%
Within-run uncertainty	2.11%	0.37%	2.03%

Table 5.1. Reproducibility and within-run uncertainties (2σ) of He isotope measurements from HELIX-SFT (n=23) and MAP 215-50 (n=16) reported as %. See text for explanation.

Figure 5.10 displays the within-run uncertainty and the reproducibility of normalised ^{3}He/^{4}He on each instrument. It demonstrates quite clearly that the HELIX-SFT has a better reproducibility and within-run uncertainty than the MAP 215-20. Some data points do not overlap the mean value suggesting that individual ratio uncertainties may be slightly underestimated.

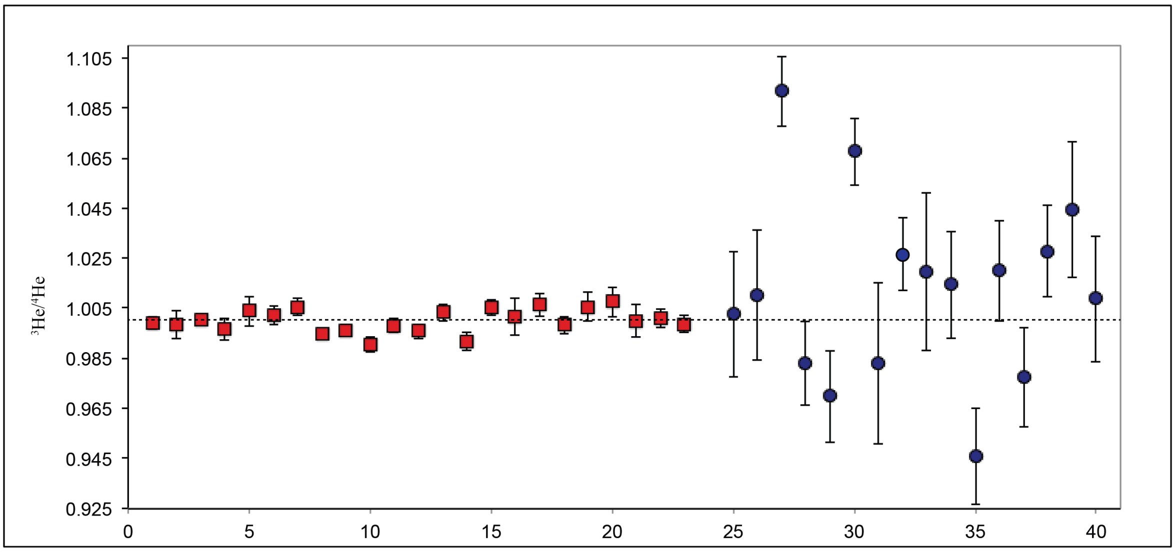

Figure 5.10. Within-run uncertainty and reproducibility of $^3He/^4He$ (HESJ) measurements for both mass spectrometers. $^3He/^4He$ have been normalised. Red squares represent HELIX-SFT data, blue circles represent MAP 215-50 data. All uncertainties are 2σ.

5.6 Discussion

The reproducibility of $^3He/^4He$ measurements of 4.86 × 10^{11} atoms of ^4He using the HELIX-SFT is much better, than the MAP 215-50. For measurements of HESJ standard gas, Sano *et al.* (2008) reported precision of 0.1–0.2% (2σ) for individual measurements and reproducibility of multiple measurements of 3‰ (2σ). The within-run uncertainty (0.52%) and reproducibility (0.78%) of measurements of HESJ reported here is worse than reported by Sano *et al* (2008). However, Sano *et al.* (2008) measured ~5.4 × 10^{12} atoms of ^4He which is an order of magnitude greater than the measurements made here. However there are aspects of the HELIX-SFT He isotope determinations reported here that are worthy of comment.

Peak stability can affect the level of uncertainty of a $^3He/^4He$ measurement. It can be seen in Figure 5.3 that small drift of mass scale within-run may subtly change ^3He ion beam intensity but not affect ^4He as it would remain on the peak top. Persistent problems with peak stability were encountered during instrument set up and never fully resolved. At the time of analysis shifts of 0.002 amu were observed. The problem may be exacerbated by sub-optimal peak shape. The resolution of the multiplier (635) is lower than specification. Consequently the amount of peak flat without isobaric interferences may be less than necessary to achieve higher levels of precision.

It is possible that environmental factors have played a role in governing the precision of measurements. The air temperature adjacent to the HELIX-SFT fluctuated from 18.5 to 21.5°C over the course of a day, with fluctuations on the time scale of individual sample/calibration measurements (25 minutes) being on the order of 0.5°C. This was a function of the location of the instrument adjacent to a large window and a wall-mounted air conditioning unit. Although there was no apparent correlation with $^{3}He/^{4}He$, the temperature range was higher, and change was more rapid, than hoped at the outset of experiments (and the MAP 215-50 laboratory). The air conditioning unit blows across the instrument. Although the Hall probe was insulated against air flow using packing sponge, it is conceivable that air flow across the detector housings and cables had a subtle affect on peak intensities. High precision noble gas isotope analysis using the SUERC HELIX-SFT will require that environmental factors are addressed.

5.7 Summary

The new HELIX-SFT at SUERC has been set up to measure small concentrations of He isotopes. Traditionally the amount of He gas used to calibrate a mass spectrometer is one order of magnitude higher than was done in this study. This is due to the desire to calibrate at similar volumes than will be measured in samples with short exposure durations. It provides significantly lower within-run uncertainties for ^{3}He, ^{4}He and $^{3}He/^{4}He$, and greater run-to-run reproducibility than the MAP 215-50. Improvements in the measurement of He isotopes will allow for an improvement in cosmogenic ^{3}He exposure age determinations. Even so, there remains potential for further improvement and with additional work the HELIX-SFT will meet the desired specifications. The recommendations outlined above will provide a starting point.

Chapter 6. Concluding thoughts

In this thesis I have conducted two distinct studies around the theme of cosmogenic He measurements. The first tested whether cosmogenic ^{3}He can be used to determine short exposure times (<30 ka) in volcanic rocks that are significantly older than the exposure time (~60 Ma). The second I reported characterisation of the new ThermoScientific HELIX-SFT and compared its performance against the existing MAP 215-50 instrument.

One question that has not yet been addressed is whether the better precision of the HELIX-SFT would have been important in this cosmogenic ^{3}He dating study? It appears that this is indeed the case. Natural variability in the He concentrations of the samples is considerable and so with superior performance by the HELIX-SFT some improvements can be expected.

Sources of uncertainty in a cosmogenic He study are random or systematic. Measurement uncertainties are random and are small when compared to systematic uncertainties. The primary control on uncertainty when deriving an absolute cosmogenic age are the uncertainties associated with production rates and scaling factors, which can be on the order of 20% (Niedermann 2002). These uncertainties are decreasing all the time with work to constrain these parameters (e.g. Masarik & Reedy 1994; 1995; 1996; Masarik & Beer 2009; Lal 1991; Stone 2000; Dunai 2000). There will be a time when measurement uncertainty is the primary control and high precision is required.

Once the HELIX-SFT performance has been improved to desired levels the main advantages it will provide will be in relative dating studies. These studies allow systematic uncertainties to be ignored. Utilisation of this instrument would be ideal in a study such as Foeken *et al.* (2009), which dated lavas from the same sequence. Reproducibility of measurements in this study averaged ~4.6%; a significant improvement would be expected in a repeat study that used the HELIX-SFT.

APPENDIX 1. Supplementary helium analysis data

Sample	Date	Weight (g)	Run	Mineral	^{3}He (at/g)	d ^{3}he (at/g)	^{3}He/^{4}He	d 3/4	R/Ra	d R/Ra	^{3}Hecos	d ^{3}Hcos
TS-1-1	12/09/12	0.1005	BU033	Ilmenite	2.28E+06	2.32E+05	116	12	0.28	0.04	3.2E+05	3.3E+04
TS-1-2	14/09/12	0.1050	BU054	Ilmenite	3.09E+06	2.59E+05	126	11	0.31	0.03	1.2E+06	9.7E+04
TS-1-3	18/09/12	0.0939	BU066	Ilmenite	1.89E+06	2.22E+05	140	24	0.35	0.05	4.2E+05	5.0E+04
TS-1-4	19/09/12	0.1216	BU072	Ilmenite	2.13E+06	1.84E+05	171	16	0.40	0.05	2.6E+05	2.2E+04
TS-1-1	12/09/12	0.1050	BU035	Olivine	3.52E+06	2.28E+05	202	10	0.48	0.05	2.0E+06	1.3E+05
TS-1-2	14/09/12	0.0951	BU053	Olivine	5.01E+06	2.99E+05	221	27	0.53	0.05	3.5E+06	2.1E+05
TS-1-3	19/09/12	0.1169	BU073	Olivine	2.81E+06	2.22E+05	182	45	0.52	0.06	1.3E+06	1.0E+05
TS-2-1	12/09/12	0.1040	BU034	Ilmenite	3.51E+06	2.14E+05	186	17	0.42	0.04	1.6E+06	9.6E+04
TS-2-2	13/09/12	0.0880	BU050	Ilmenite	3.42E+06	3.36E+05	202	21	0.50	0.06	1.4E+06	1.4E+05
TS-2-3	14/09/12	0.0910	BU056	Ilmenite	3.90E+06	2.41E+05	230	24	0.54	0.05	1.9E+06	1.2E+05
TS-2-4	18/09/12	0.0936	BU068	Ilmenite	3.70E+06	3.50E+05	234	24	0.57	0.07	1.7E+06	1.6E+05
TS-2-5	19/09/12	0.1400	BU076	Ilmenite	3.22E+06	2.10E+05	176	21	0.46	0.05	1.4E+06	9.1E+04
TS-2-1	14/09/12	0.0941	BU055	Olivine	5.14E+06	2.49E+05	394	17	0.96	0.08	3.6E+06	1.8E+05
TS-2-2	18/09/12	0.1043	BU067	Olivine	5.20E+06	3.16E+05	404	24	0.99	0.09	3.7E+06	2.2E+05
TS-2-3	19/09/12	0.1141	BU077	Olivine	4.98E+06	2.30E+05	380	15	0.93	0.08	3.5E+06	1.6E+05
TS-4-1	28/05/13	0.1978	BX023	Olivine	2.13E+06	1.26E+05	615	36	1.51	0.14	6.3E+05	3.7E+04
TS-4-2	28/05/13	0.1954	BX025	Olivine	2.35E+06	1.67E+05	642	52	1.66	0.17	8.5E+05	6.0E+04
TS-5-1	22/05/13	0.2421	BX009	Olivine	2.91E+06	2.14E+05	378	28	0.93	0.10	1.4E+06	1.0E+05
TS-5-2	28/05/13	0.2229	BX024	Olivine	2.42E+06	1.30E+05	376	19	0.93	0.08	9.2E+05	5.0E+04
TS-5-3	28/05/13	0.2020	BX022	Olivine	2.88E+06	2.09E+05	481	34	1.18	0.12	1.4E+06	1.0E+05
QR-1-1	22/05/13	0.2035	BX008	Olivine	1.53E+06	1.46E+05	305	30	0.75	0.09	-	-
QR-1-2	22/05/13	0.2165	BX010	Olivine	1.47E+06	1.94E+05	271	37	0.62	0.09	-	-
TS-1-1	18/10/12	0.4038	BU192	Plagioclase	3.61E+04	2.26E+04	436	273	1.08	0.68	-	-
TS-2-1	18/10/12	0.2581	BU194	Plagioclase	1.27E+04	9.11E+03	261	272	0.65	0.68	-	-

Table A1.1. Analysis data for all exposed samples collected from the Storr, Isle of Skye and shielded sample collected from the Quiraing, Isle of Skye. Sensitivity of ^{3}He and ^{4}He for analyses TS-1 through to TS-2 were; 2.27 e^4 a/cps and 7.63 e^{12} a/V respectively. Sensitivity of ^{3}He and ^{4}He for analyses TS-4 and TS-5 were; 2.22 e^4 a/cps and 7.63 e^{12} a/V respectively. Sensitivity of ^{3}He and ^{4}He for QR-1 were; 2.3 e^4 a/cps and 7.63 e^{12} a/V respectively.

APPENDIX 2. Detailed petrographic descriptions

A2.1 TS-1

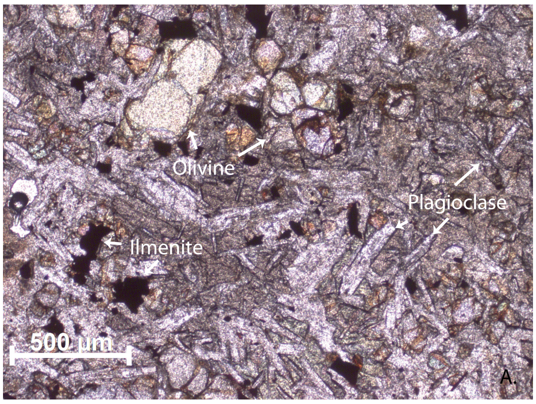

Figure A2.1. TS-1 in plane polarised light

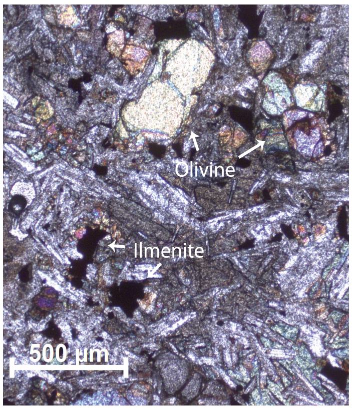

Figure A2.2. TS-1 in cross-pol

Mineral grain descriptions:

- Olivine – 100 – 750 µm, slightly altered, occasional intergr products, fractured, euhedral to sub-euhedral.
- Pyroxene – Extremely disseminated, ophitic texture, constitut groundmass.
- Plagioclase – 100 – 500 µm, lath shaped, mixed alteration, weak
- Ilmenite – 50 – 500 µm, cubic to euhedral, occur commonly as i
- Alteration products – Fibrous and brown, form from alteration olivine.

A2.2 TS-2

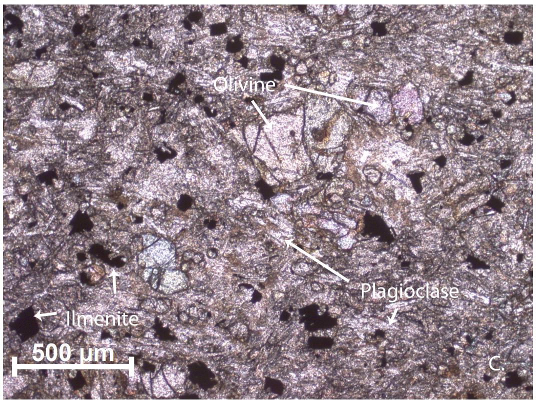

Figure A2.3. TS-2 in plane polarised light

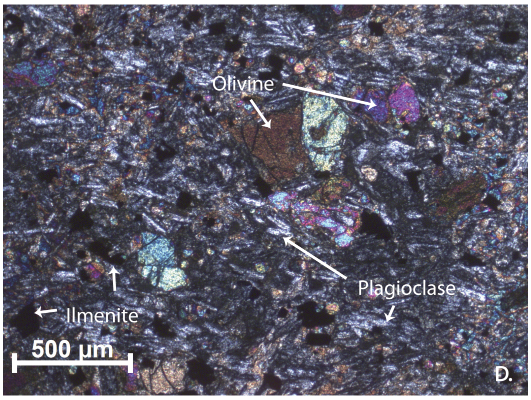

Figure A2.4 TS-2 in cross-polarised light

Mineral grain descriptions:

- Olivine – 100 – 1500 µm, slightly altered, occasional intergrowths of alteration products, fractured, euhedral to sub-euhedral.
- Pyroxene – heavily fractured with extensive intergrowths of plagioclase laths, opaques and olivines. Ophitic texture, very disseminated. Original grains ~1 – 5 mm.
- Plagioclase – 100 – 1000 µm, lath shaped, mixed alteration, weakly define a fabric.
- Ilmenite – 50 – 500 µm, cubic to euhedral, occur commonly as intergrowths.
- Alteration products – Fibrous and brown, form from alteration of plagioclase and olivine.

A2.3 TS-4

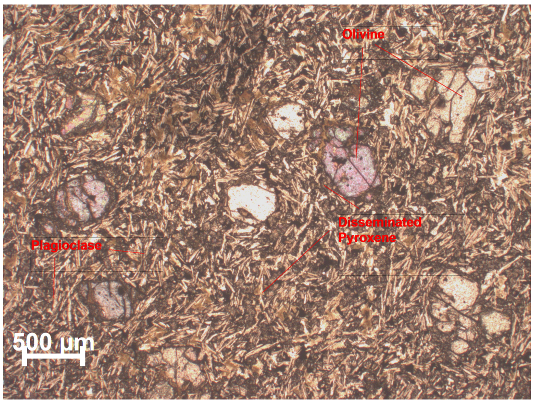

Figure A2.5. TS-4 in plane polarised light

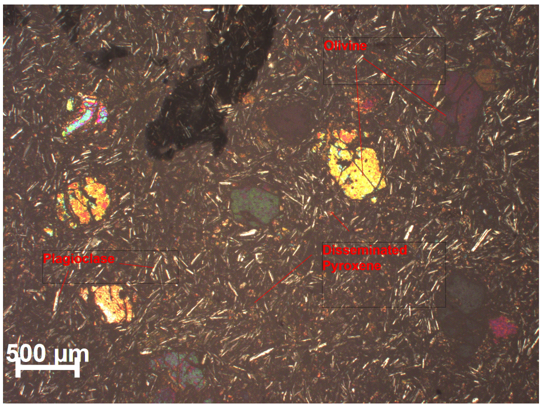

Figure A2.5. TS-4 in cross-polarised light

Mineral grain descriptions:

- Olivine – 100 – 500 µm, slightly altered, occasional intergrowths of alteration products, fractured, euhedral to sub-euhedral.
- Pyroxene – heavily fractured with extensive intergrowths of plagioclase laths, opaques and olivines. Ophitic texture, very disseminated. Original grains ~1 – 5 mm.
- Plagioclase – 50 - 500 µm, lath shaped, mixed degrees of alteration.

A2.4 TS-5

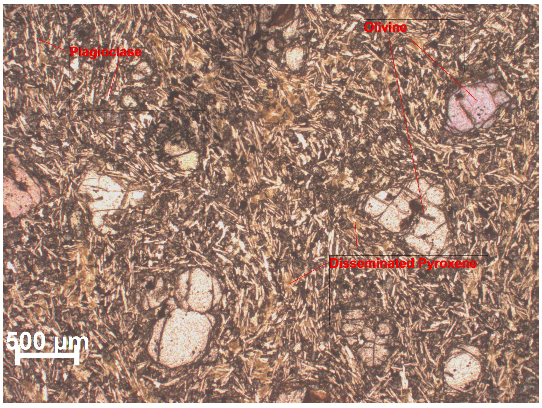

Figure A2.7. TS-5 in plane polarised light

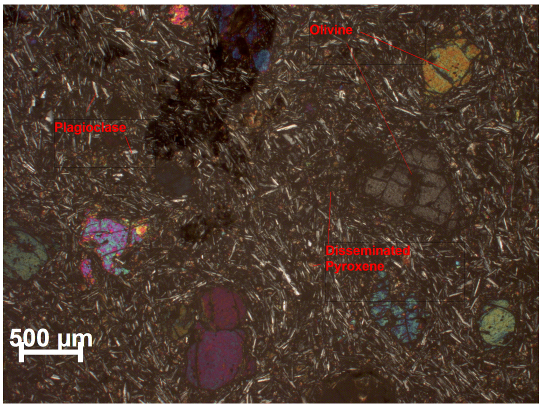

Figure A2.8. TS-5 in cross-polarised light

Mineral grain descriptions:

- Olivine – 100 – 500 µm, slightly altered, occasional intergrowths of alteration products, fractured, euhedral to sub-euhedral.
- Pyroxene – heavily fractured with extensive intergrowths of plagioclase laths, opaques and olivines. Ophitic texture, very disseminated. Original grains ~1 – 5 mm.
- Plagioclase – 50 - 500 µm, lath shaped, mixed degrees of alteration.

A2.5 QR-1

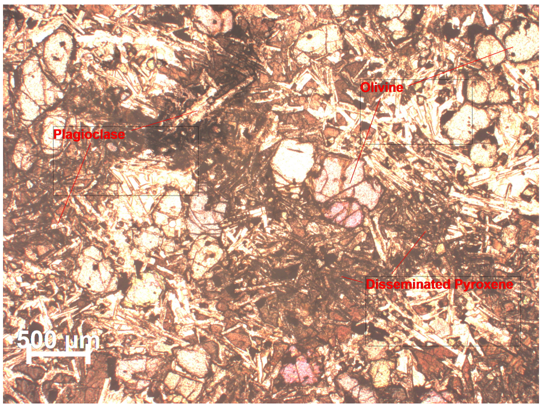

Figure A2.9. QR-1 in plane polarised light

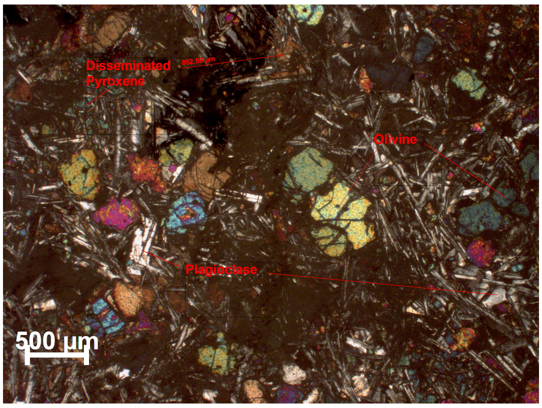

A2.10. QR-1 in cross-polarised light

Mineral grain descriptions:

- Olivine – 100 – 1500 µm, slightly altered, occasional intergrowths of alteration products, fractured, euhedral to sub-euhedral.
- Pyroxene – heavily fractured with extensive intergrowths of plagioclase laths, opaques and olivines. Ophitic texture, very disseminated. Original grains ~1 – 5 mm.
- Plagioclase – 100 - 1000 µm, lath shaped, mixed degrees of alteration.

APPENDIX 3 – Detailed calibration data; HELIX-SFT and MAP 215-50

A3.1 – HELIX-SFT data

Run Number	Integration Time (secs)	Data Cycles	^{4}He (fA)	± 2s	%	^{3}He (fA)	± 2s	%	^{3}He/^{4}He	± 2s	%
HC0017	67.11	20	2113.0	0.05	0.002%	4.58E-02	1.55E-04	0.34%	0.9992	0.0026	0.34%
HC0018	67.11	20	2102.7	0.34	0.016%	4.54E-02	2.84E-04	0.63%	0.9984	0.0057	0.75%
HC0019	67.11	20	2101.0	0.14	0.007%	4.62E-02	1.77E-04	0.38%	1.0003	0.0014	0.18%
HC0020	67.11	20	2099.3	0.17	0.008%	4.56E-02	1.83E-04	0.40%	0.9965	0.0042	0.56%
HC0021	67.11	20	2110.8	0.21	0.010%	4.61E-02	1.83E-04	0.40%	1.0038	0.0059	0.78%
HC0022	67.11	20	2101.1	0.25	0.012%	4.60E-02	1.28E-04	0.28%	1.0020	0.0038	0.50%
HC0023	67.11	20	2099.7	0.17	0.008%	4.61E-02	2.39E-04	0.52%	1.0055	0.0036	0.47%
HC0024	67.11	20	2110.4	0.13	0.006%	4.58E-02	1.99E-04	0.43%	0.9945	0.0014	0.19%
HC0025	67.11	20	2115.2	0.09	0.004%	4.57E-02	1.37E-04	0.30%	0.9963	0.0019	0.25%
HC0027	67.11	20	2105.4	0.12	0.006%	4.53E-02	1.62E-04	0.36%	0.9905	0.0029	0.39%
HC0028	67.11	20	2108.9	0.12	0.006%	4.56E-02	9.63E-05	0.21%	0.9980	0.0027	0.36%
HC0029	67.11	20	2113.9	0.08	0.004%	4.53E-02	1.04E-04	0.23%	0.9957	0.0030	0.40%
HC0030	67.11	20	2116.2	0.28	0.013%	4.64E-02	1.51E-04	0.33%	1.0032	0.0033	0.43%
HC0031	67.11	20	2106.0	0.11	0.005%	4.54E-02	1.93E-04	0.42%	0.9919	0.0037	0.49%
HC0032	67.11	20	2110.3	0.21	0.010%	4.60E-02	1.37E-04	0.30%	1.0054	0.0032	0.42%
HC0033	67.11	20	2102.9	0.29	0.014%	4.51E-02	1.69E-04	0.37%	1.0016	0.0074	0.97%
HC0034	67.11	20	2114.1	0.13	0.006%	4.65E-02	1.63E-04	0.35%	1.0065	0.0047	0.61%
HC0035	67.11	20	2119.7	0.06	0.003%	4.57E-02	1.18E-04	0.26%	0.9983	0.0035	0.46%
HC0037	67.11	20	2103.8	0.25	0.012%	4.63E-02	1.73E-04	0.37%	1.0055	0.0056	0.74%
HC0039	67.11	20	2108.6	0.23	0.011%	4.61E-02	2.06E-04	0.45%	1.0075	0.0060	0.79%
HC0040	67.11	20	2109.2	0.17	0.008%	4.58E-02	1.98E-04	0.43%	0.9997	0.0065	0.86%
HC0041	67.11	20	2109.7	0.18	0.009%	4.56E-02	1.49E-04	0.33%	1.0009	0.0036	0.47%
HC0042	67.11	20	2105.4	0.20	0.009%	4.57E-02	1.69E-04	0.37%	0.9986	0.0035	0.46%

Table A3.1. HELIX-SFT HESJ calibration data. ^{3}He/^{4}He has been normalised.

Run Number	Integration Time (secs)	Data Cycles	^{4}He (fA)	± 2s	%	^{3}He (fA)	± 2s	%	^{3}He/^{4}He	± 2s	%
HC0084	33.55	50	2129.00	0.95	0.0004	5.26E-02	4.31E-04	0.82%	0.9806	0.0084	0.86%
HC0086	33.55	50	2121.10	0.95	0.0004	5.28E-02	4.66E-04	0.88%	0.9883	0.0082	0.83%
HC0087	33.55	50	2130.00	0.82	0.0004	5.36E-02	4.94E-04	0.92%	0.9987	0.0098	0.98%
HC0088	33.55	50	2126.10	0.90	0.0004	5.36E-02	5.53E-04	1.03%	1.0015	0.0109	1.09%
HC0089	33.55	50	2115.90	0.83	0.0004	5.34E-02	5.37E-04	1.01%	1.0021	0.0107	1.07%
HC0090	33.55	50	2125.10	0.99	0.0005	5.32E-02	5.59E-04	1.05%	0.9935	0.0091	0.92%
HC0091	33.55	50	2120.30	0.83	0.0004	5.33E-02	5.04E-04	0.95%	0.9949	0.0089	0.89%
HC0092	33.55	50	2122.00	0.83	0.0004	5.37E-02	4.82E-04	0.90%	1.0039	0.0087	0.87%
HC0093	33.55	50	2123.10	0.87	0.0004	5.38E-02	4.95E-04	0.92%	1.0078	0.0102	1.01%
HC0094	33.55	50	2118.20	0.78	0.0004	5.38E-02	4.71E-04	0.88%	1.0070	0.0091	0.90%
HC0095	33.55	50	2116.70	0.82	0.0004	5.40E-02	5.59E-04	1.04%	1.0100	0.0099	0.98%
HC0096	33.55	50	2119.50	0.81	0.0004	5.40E-02	5.75E-04	1.06%	1.0118	0.0113	1.12%

Table A3.2. HELIX-SFT HESJ calibration data measured at 33.55-second integrations. Note the increased ^{3}He/^{4}He uncertainties associated with the shorter integration period compared with data in Table A1.1.

A3.2 MAP 215-50 data

Run Number	Integration Time (secs)	Data Cycles	4He (V)	± 2s	± %	3He (cps)	± 2s	± %	3He/4He	± 2s	± %
BU042	10 x 10	10	0.023301	0.000023	0.10%	241	6	2.49%	1.0026	0.0250	2.49%
BU052	10 x 10	10	0.022797	0.000026	0.11%	234	6	2.56%	1.0102	0.0259	2.57%
BU064	10 x 10	10	0.024427	0.000023	0.09%	232	3	1.29%	1.0918	0.0142	1.30%
BU070	10 x 10	10	0.022279	0.00004	0.18%	235	4	1.70%	0.9831	0.0168	1.71%
BU078	10 x 10	10	0.021791	0.000178	0.82%	233	4	1.72%	0.9698	0.0184	1.90%
BU079	10 x 10	10	0.024401	0.000229	0.94%	237	2	0.84%	1.0676	0.0135	1.26%
BU090	10 x 10	10	0.023601	0.000167	0.71%	249	8	3.21%	0.9829	0.0323	3.29%
BU115	10 x 10	10	0.023464	0.000146	0.62%	237	3	1.27%	1.0266	0.0145	1.41%
BU122	10 x 10	10	0.022226	0.000040	0.18%	226	7	3.10%	1.0198	0.0316	3.10%
BU123	10 x 10	10	0.023186	0.000031	0.13%	237	5	2.11%	1.0145	0.0214	2.11%
BU129	10 x 10	10	0.022523	0.000043	0.19%	247	5	2.02%	0.9456	0.0192	2.03%
BU130	10 x 10	10	0.023017	0.000223	0.97%	234	4	1.71%	1.0200	0.0200	1.96%
BU135	10 x 10	10	0.022811	0.000050	0.22%	242	4	1.65%	0.9774	0.0163	1.67%
BU136	10 x 10	10	0.022500	0.000074	0.33%	227	4	1.76%	1.0278	0.0184	1.79%
BU139	10 x 10	10	0.023466	0.000050	0.21%	233	6	2.58%	1.0443	0.0270	2.58%
BU141	10 x 10	10	0.023348	0.000030	0.13%	240	6	2.50%	1.0088	0.0253	2.50%

Table A3.3. MAP 215-50 HESJ calibration data. ^{3}He/^{4}He has been normalised.

References

Aciego, S. M., DePaolo, D. J., Kennedy, B. M., Lamb, M. P., Sim
Dietrich, W. E., 2007. Combining [^{3}He] cosmogenic dating wit
ages using olivine in basalt. *Earth and Planetary Science Letters*

Ackert Jr., R. P., Barclay, D. J., Borns Jr., H. W., Calkin, P. E., Kurz, M
and Steig, E. J., 1999. Measurements of past ice sheet elevatic
Antarctica. *Science* **286** 276-280.

Ackert Jr., R. P., Kurz, M. D., 1999. Age and uplift rates of Sirius Gro
Dominion Range, Antarctica, from surface exposure dating ar
Global and Planetary Change **42** 207-225.

Aldrich, L. T., and Nier, A. O., 1948b. The occurrence of ^{3}He in
helium. *Physical Review* **74**: 1500-94.

Allen, J. S., 1939. The detection of single positive ions, electrons
secondary electron multiplier. *Physical Review* **55** (10): 966.

Allen, J. S., 1947. An improved electron multiplier particle counter. *R*
(10): 739.

Allkofer, O. C. and Greider, P. K. F., 1984. Cosmic rays on Earth. *Phys*

Alpert, D., 1951. Vacuum valve for the handling of very pure gases. *R*
536.

Ammon, K., Dunai, T. J., Stuart, F. M., Meriaux, A.-S., and Gayer, E.,
^{3}He exposure ages and geochemistry of basalts from Ascensi
Ocean. *Quaternary Geochronology* **4** 525-532.

Anderson, F. W., and Dunham, K. C., 1966. The geology of northern S
Geological Survey of Great Britain. HMSO, Britain.

Andrews, J. N., 1985. The isotopic composition of radiogenic helium
groundwater movement in confined aquifers. *Chemical Geology*

Andrews, J. N. and Kay, R. L. F., 1982. Natural production of tritium in
rocks, *Nature* **298** 361–363.

Ballentine, C. J. and Burnard, P. G., 2002. Production, release and trans
in the continental crust. In: D. Porcelli, C. J. Ballentine and R. W
Gases in Geochemistry and Cosmochemistry, Reviews in
Geochemistry 47, Washington: The Mineralogical Society of
538.

Ballantyne, C. K., 1990. The late Quaternary glacial history
Escarpment, Isle of Skye, Scotland, and it's implications for ice-sl
Proceedings for the Geologists' Association **101** 171-86.

Ballantyne, C. K., McCarroll, D., Nesje, A., Dahl, S. O., Stone, J. O., 1998. The last ice sheet in NW Scotland: reconstruction and implications. *Quaternary Science Reviews* **17** 1149-1184.

Ballantyne, C., K., 2010. Extent and deglacial chronology of the last British-Irish Ice Sheet: implications of exposure dating using cosmogenic isotopes. *Journal of Quaternary Science* **25** (4) 515-534.

Balco, G. and Schaefer, J. M., 2006. Cosmogenic-nuclide and varve chronologies for the deglaciation of southern New England. *Quaternary Geochronology* **1** (1): 15-28.

Balco, G., Stone, J. O., Lifton, N. A. and Dunai, T. J., 2008. A complete and easily accessible means of calculating surface exposure ages or erosion rates from ^{10}Be and ^{26}Al measurements, *Quaternary Geochronology* **3** 174–195.

Barfod, D. N., Mark, D. F., Tait, A., Dymock, R. C., and Imlach, J., *In Press*. Argon extraction from geological samples by CO_2 scanning laser step-heating. *Geol. Soc. Spec. Ed. (Advances in Ar/Ar dating).*

Baur, H., 1980. Numerische simulation und praktische erprobung einer rotationssymmetrischen ionenquelle für gasmassenspektrometer. No. 6596. In Vol. ETH, Zürich

Blackburn, T. J., Stockli, D. F., and Walker, J. D., 2007. Magnetite (U-Th)/He dating and its application to the geochronology of intermediate to mafic volcanic rocks. *Earth and Planetary Science Letters* **259** 360-371.

Blackett, P. M. S., 1960. Charles Thomson Rees Wilson. *Biographical Memoirs of Fellows of the Royal Society* **6** 269-295.

Blard, P. H., Lave, J., Pik, R., Quindelleur, X., Bourles, D. L. and Kieffer, G., 2005. Fossil cosmogenic ^{3}He record from K–Ar dated basaltic flows of Mount Etna volcano (Sicily, 38^{o}N): Evaluation of a new paleoaltimeter, *Earth and Planetary Science Letters* **236** 613–631.

Blard, P. H., Pik, R., Lavé, J., Bourlès, D., Bunard, P.G., Yokochi, R., Marty, B. and Trusdell, F., 2006. Cosmogenic ^{3}He production rates revisited from evidence of grain size dependent release of matrix sited helium, *Earth and Planetary Science Letters* **247** 222–234.

Blard, P. H. and Farley, K. A., 2008. The influence of radiogenic ^{4}He on cosmogenic ^{3}He determinations in volcanic olivine and pyroxene. *Earth and Planetary Science Letters* **276** 20-29.

Blard, P. H., Puchol, N. and Farley, K. A., 2008. Constraints on the loss of matrix-sited helium during vacuum crushing of mafic phenocrysts. *Geochimica Et Cosmochimica Acta* **72** (15): 3788-3803.

Brook, E. J., Kurz, M.D., Ackert, R. P., Raisbeck, G.M. and Yiou, F., 1995b. Cosmogenic nuclide exposure ages and glacial history of late Quaternary Ross Sea drift in McMurdo Sound, Antarctica, *Earth and Planetary Science Letters* **131** 41–56.

Brook, E. J., Nesje, A., Lehman, S. J., Raisbeck, G. M., Yiou, F., 1996. Cosmogenic nuclide exposure ages along a vertical transect in western Norway: Implications for the height of the Fennoscandian ice sheet. *Geology.* **24** 207-210.

Brown, E.T., Trull, W.T., Jean-Baptiste, P., Raisbeck,G., Bourle` s, D., Yiou, F. and Marty, B., 2000. Determination of cosmogenic production rates of ^{10}Be, ^{3}He, and ^{3}H inwater, *Nucl. Inst. Meth. Phys. Res. B* **172** 873–883.

Bryce, J. G. and Farley, K. A., 2002. ^{3}He exposure dating of Magnetite. ,in: F.A. Podosek (Ed.), Goldschmidt Conference, *Geochim. Cosmochim. Acta,* **66** (15A) A108 Davos, Switzerland

Cerling, T. E. and Craig, H., 1994. Cosmogenic ^{3}He production rates from 39°N to 46°N latitude, western USA and France. *Geochimica Et Cosmochimica Acta* **58**(1): 249-255.

Coble, M. A., Grove, M., and Calvert, A. T., 2011. Calibration of Nu-Instruments Noblesse multicollector mass spectrometers for argon isotopic measurements using newly a developed reference gas. *Chemical Geology* **290** 75-87.

Colin, A., Burnard, P. and Marty, B., 2013. Mechanisms of magma degassing at mid-ocean ridges and the local volatile composition (^{4}He – ^{40}Ar – CO_2) of the mantle by laser ablation analysis of individual MORB vesicles. *Earth and Planetary Science Letters* **361** 183-194.

Dahl, S. O., Ballantyne, C. K., McCarroll, D., Nesje, A., 1996. Maximum altitude of Devensian glaciation on the Isle of Skye. *Scottish Journal of Geology.* **32** 107-115.

Davis, R., J. and Schaffer, O., A., 1955. Chlorine-36 in nature. *Annals New York Academy of Science* **62** 105-122.

Desilets, D. and Zreda, M., 2003. Spatial and temporal distribution of secondary cosmic-ray nucleon intensities and applications to in situ cosmogenic dating, *Earth and Planetary Science Letters* **206** 21–42.

Desilets, D., Zreda, M. and Prabu, T., 2006b. Extended scaling factors for in situ cosmogenic nuclides: New measurements at low latitude, *Earth and Planetary Science Letters* **246** 265–276.

Diehl, R., Halloin, H., Kretschmer, K., Lichti,G.G., Schönfelder, V., Strong, A.W., von Kienlin, A., Wang, W., Jean, P., Knödlseder, J., Roques, J. P., Weidenspointner,G., Schanne, S., Hartmann, D.H., Winkler, C. and Wunderer, C., 2006. Radioactive Al-26 from massive stars in the Galaxy, *Nature* **439** 45–47.

Dorman, L. I., Valde´s-Galicia, J. F. and Dorman, I. V., 1999. Numerical simulation and analytical description of solar neutron transport in the Earth's atmosphere, *J. Geophys. Res.* **104** 22417–22426.

Dunai, T. J., 2000. Scaling factors for production rates of in situ produced cosmogenic nuclides: a critical reevaluation, *Earth and Planetary Science Letters* **176** 157–169.

Dunai, T. J. and Wijbrans, J. R., 2000. Long-term cosmogenic ^{3}He production rates (152 - 1.35 Ma) from ^{40}Ar/^{39}Ar dated basalt flows at 29°N latitude. *Earth and Planetary Science Letters* **176** (1): 147-156.

Dunai, T. J., 2001. Influence of secular variation of the geomagnetic field on production rates of in situ produced cosmogenic nuclides. *Earth and Planetary Science Letters* **193** (1-2): 197-212.

Dunai, T. J. and Porcelli, D., 2002. Storage and transport of noble gases in the subcontinental lithosphere. In: D. Porcelli, C. Ballentine and R. Wieler, (Eds), Noble Gases in Cosmochemistry and Geochemistry, Reviews in Mineralogy and Geochemistry 47, Washington: The Mineralogical Society of America, pp. 371–410.

Dunai, T. J., Stuart, F. M., Pik, R., Burnard, P. G. and Gayer, E., 2007. Production of ^{3}He in crustal rocks by cosmogenic thermal neutrons. *Earth and Planetary Science Letters* **258** (1-2): 228-236.

Eidelman, S., Hayes, K. G., Olive, K. A., Aguilar-Benitez, M., Amsler, C., Asner, D., Babu, K. S., Barnett, R. M., Beringer, J., Burchat, P. R., Carone, C. D., Caso, C., Conforto, G., Dahl, O., D'Ambrosio, G., Doser, M., Feng, J. L., Gherghetta, T., Gibbons, L., Goodman, M., Grab, C., Groom, D. E., Gurtu, A., Hagiwara, K., Hernandez-Rey, J. J., Hikasa, K., Honscheid, K., Jawahery, H., Kolda, C., Kwon, Y., Mangano, M. L., Manohar, A. V., March-Russell, J. and Masoni, A., 2004. Review of particle physics, *Phys. Lett*. B **592** 1–1109.

Evans, J. M., Stone, J. O. H., Fifield, L. K. and Cresswell, R. G., 1997. Cosmogenic chlorine-36 production in K-feldspar, *Nucl. Instr. Meth. Phys. Res.* B **123** 334–340.

Evans, J.M., 2002. Calibration of the Production Rates of Cosmogenic ^{36}Cl from Potassium, Ph.D. dissertation, Australian National University.

Farley, K. A., Wolf, R. A. and Silver, L. T., 1996. The effects of long alpha-stopping distances on (U-Th)/He ages, *Geochim. Cosmochim. Acta* **60** 4223–4229.

Farley, K. A., Libarkin, J., Mukhopadhyay, S. and Amidon, W., 2006. Cosmogenic and nucleogenic ^{3}He in apatite, titanite, and zircon. *Earth and Planetary Science Letters* **248** 451-461.

Farley, K. A., 2007. He diffusion systematics in minerals: Evidence from synthetic monazite and zircon structure phosphates, *Geochim. Cosmochim. Acta* **71** 4015–4052.

Faure, G., 1986. Principles of isotope geology, John Wiley & sons.

Filges, D., Goldenbaum, F., Enke, M., Galin, J., Herbach, C.M., Hilscher, D., Jahnke, U., Letourneau, A., Lott, B., Neef, R.D., Nunighoff, K., Paul, N., Peghaire, A., Pienkowski, L., Schaal, H., Schroder, U., Sterzenbach, G., Tietze, A., Tishchenko, V., Toke, J. and Wohlmuther, M., 2001. Spallation neutron production and the current intra-nuclear cascade and transport codes. *Eur. Phys. J.* A **11** 467–490.

Fink, D., Vogt, S., Hotchkis, M., 2000. Cross-sections for ^{36}Cl from Ti at E_p = 35 - 150 MeV: applications to in-situ exposure dating. *Nuclear Instruments and Methods in Physics Research Section* **B 172**, 861-866.

Foeken, J. P. T., Stuart, F. M., Dobson, K. J., Persano, C., Vilbert, D., 2006. A diode laser system for heating minerals for (U-Th)/He chronometry. *Geochemistry, Geophysics, Geosystems* **7** (4).

Foeken, J. P. T., Day, S. J., Stuart, F. M., 2009. Cosmogenic ^{3}He exposure dating of the Quaternary basalts from Fogo, Cape Verdes: Implications for rift zone and magmatic reorganisation. *Quaternary Geochronology* **4** 37-49.

Foeken, J. P. T., Stuart, F. M., Mark, D. F., 2012. Long-term low latitude cosmogenic ^{3}He production rate determined from a 126 ka basalt from Fogo, Cape Verdes. *Earth and Planetary Science Letters* **359-360** 14-25.

Gayer, E., Mukhopadhyay, S., and Meade, B. J., 2008. Spatial variability of erosion rates inferred from the frequency distribution of cosmogenic ^{3}He in olivines from Hawaiian river sediments. *Earth and Planetary Science Letters* **266** 303-315.

Goehring, B. M., Kurz, M. D., Balco, G., Schaefer, J. M., Licciardi, J., Lifton, N., 2010. A reevaluation of cosmogenic ^{3}He production rates, *Quaternary Geochronology* **5** (4): 410-418.

Gosse, J. C. and Phillips, F. M., 2001. Terrestrial in situ cosmogenic nuclides: theory and application. *Quaternary Science Reviews* **20** (14): 1475-1560.

Graham, D. W., 2002. Noble gas isotopic geochemistry of mid-ocean ridge and ocean island basalts: Characterization of mantle source reservoirs. *Rev. Mineral. Geochem.* **47** 247–318.

Groom, D. E., Mokhov, N. V. and Striganov, S. I., 2001. Muon stopping-power and range tables, *Atom. Data Nucl. Data Tables* **78** 183–356.

Grosse, A., V., 1934. An unknown radioactivity. *J. Am. Chem. Soc.* **56** 1922-1924.

Hablanian, M. H., 1990. High-vacuum technology: A practical guide. Marcel Dekker, Inc.

Harris, N. S., 1997. Modern vacuum practice. McGraw-Hill, UK.

Harker, A., 1901. Ice erosion in the Cuillin Hills, Skye. *Trans. R. Soc. Edin.* **40** 76-99.

Heisinger, B., Lal, D., Jull, A. J. T., Kubik, P., Ivy-Ochs, S., Knie, K. and Nolte, E., 2002a. Production of selected cosmogenic radionuclides by muons: 2. Capture of negative muons. *Earth and Planetary Science Letters* **200** 357-369.

Heisinger, B., Lal, D., Jull, A. J. T., Kubik, P., Ivy-Ochs, S., Neumaier, S., Knie, K., Lazarev, V. and Nolte, E., 2002b. Production of selected cosmogenic radionuclides by muons 1. Fast muons, *Earth and Planetary Science Letters* **200** 345–355.

Herbert, C. G. and Johnstone, R. A. W., 2003. Mass spectrometry basics, CRC press

Hess, V., F., 1912. Über Beobachtungen der durchdringenden Strahlung bei sieben Freiballonfahrten. *Z. Phys.* 1084.

Hohenberg, C. M., (1980). High sensitivity pulse-counting mass spectrometer system for noble gas analysis. *Rev. Sci. Instrum.* **51** 1075-1082.

House, M. A., Farley, K. A., Stockli, D., 2000. Helium chronometry of apatite ant titanite using Nd-YAG laser heating. *Earth and Planetary Science Letters.* **183** (3-4): 365-368.

Inczédy, J., Lengyel, T., Ure, A. M., 1997. IUPAC. Analytical Division. Compendium of Analytical Nomenclature (the "Orange Book"). Definitive Rules, 1979. Blackwell Scientific Publications, Oxford.

Jicha, B., Sobol, P., and Signer, B., 2010. The UW-Madison 5 collector mass spectrometer for high precision ^{40}Ar/^{39}Ar geochronology. *American Geophysical Union fall meeting 2010, abstract #V31A-2299.*

Jull, A. J. T., Wilson, A. E., Donahue, D. J., Toolin, L. J. and Burr, G. S., 1992. Measurement of cosmogenic ^{14}C produced by spallation in high-altitude rocks, *Radiocarbon* **34** 737–744.

Klemen, J., and Borgström, I., 1990. The boulder fields of Mt Furufjället, west-central Sweden. *Geogr. Annlr.* **72A** 63-78.

Kober, F., Ivy-Ochs, S., Leya, I., Baur, H., Magna, T., Wieler, R. and Kubik, P. W., 2005. In situ cosmogenic ^{10}Be and ^{21}Ne in sanidine and in situ cosmogenic ^{3}He in Fe-Ti-oxide minerals, *Earth and Planetary Science Letters* **236** 404–418.

Kubik, P. W., Ivy-Ochs, S., Masarik, J., Frank, M. and Schlüchter, C., 1998. ^{10}Be and ^{26}Al production rates deduced from an instantaneous event within the dendro-calibration curve, the landslide of Köfels, Ötz Valley, Austria. *Earth and Planetary Science Letters* **161** 231-241.

Kurz, M. D., 1986. Cosmogenic helium in a terrestrial igneous rock. *Nature* **320** (6061): 435-439.

Kurz, M. D., Colodner, D., Trull, T. W., Moore, R. B. and O'Brien, K., 1990. Cosmic ray exposure dating with in situ produced cosmogenic ^{3}He: Results from young Hawaiian lava flows. *Earth and Planetary Science Letters* **97** (1-2): 177-189.

Lal, D. and Peters, B., 1967. Cosmic ray produced radioactivity on Earth. In: S. Flugg, (Ed), *Handbook of Physics* **46/2**, Berlin: Springer, 551–612.

Lal, D., 1987. Production of ^{3}He in terrestial rocks, *Chem. Geol.* **66** 89–98.

Lal, D., 1988. In situ-produced cosmogenic isotopes in terrestrial rocks, *Ann. Rev. Earth Planet. Sci.* **16** 355–388.

Lal, D., 1991. Cosmic ray labeling of erosion surfaces: in situ nuclide production rates and erosion models, *Earth and Planetary Science Letters* **104** 424–439.

Leya, I., Busemann, H., Baur, H., Wieler, R., Gloris, M., Neurmann, S., Michel, R., Sudbrock, F. and Herpers, U., 1998. Cross sections for the proton-induced production of He and Ne isotopes from magnesium, aluminum, and silicon. *Nuclear Instruments and Methods in Physics Research Section B: Beam Interactions with Materials and Atoms* **145** (3): 449-458.

Leya, I., Lange, H. J., Neumann, S., Wieler, R. and Michel, R., 2000. The production of cosmogenic nuclides in stony meteoroids by galactic cosmic-ray particles. *Meteoritics & Planetary Science* **35** (2): 259-286.

Libby, F., Anderson, E., C., Arnold, J., R., 1949. Age determination by radiocarbon content: World-wide assay of natural radiocarbon. *Science* **109** 227-228.

Licciardi, J. M., Kurz, M. D., Clark, P. U. and Brook, E. J., 1999. Calibration of cosmogenic ^{3}He production rates from Holocene lava flows in Oregon, USA, and effects of the Earth's magnetic field, *Earth and Planetary Science Letters* **172** 261–271.

Licciardi, J. M., Kurz, M. D., and Curtice, J. M., 2006. Cosmogenic ^{3}He production rates from holocene lava flows in Iceland. *Earth and Planetary Science Letters* **246** 251-264.

Lifton, N., Bieber, J. W., Clem, J. M., Duldig, M. L., Evenson, P., Humble, J. E. and Pyle, R., 2005. Addressing solar modulation and long-term uncertainties in scaling secondary cosmic rays for in situ cosmogenic nuclide applications, *Earth Planet. Sci. Lett.* **239** 140–161.

Lifton, N., 2008. In situ cosmogenic C-14 from surfaces at secular equilibrium, *Geochim. Cosmochim. Acta* **72** A552.

Lifton, N. A., Smart, D. F. and Shea, M. A., 2008. Scaling time-integrated in situ cosmogenic nuclide production rates using a continuous geomagnetic model, *Earth and Planetary Science Letters* **268** 190–201.

Lippolt, H. J. and Weigel, E., 1988. ^{4}He diffusion in ^{40}Ar-retentive minerals, *Geochim. Cosmochim. Acta* **52** 1449–1458.

Lucas. L, L. and Unterweger, M. P., 2000. Comprehensive review and critical re-evaluation of the half-life of Tritium, *J. Res. Natl. Inst. Stand. Technol.* **105** 541-549.

Lynch, M. C. F., and Kay, D. J., 1981. Methods of low-level counting and spectrometry. pp. 511-523, *Int. At. Energy Agency, Vienna.*

Mabry, J. C., Marty, B., Burnard, P. and Blard, P., 2010. Variation in atmospheric helium isotopes. *American Geophysical Union, Fall Meeting 2010, abstract #A41C-0091*

Mamyrin, B. A., Anufriyev, G. S., Kamensky, I.L. and Tolstikhin, I. N., 1970. Determination of the isotopic composition of helium, *Geochem. Int.* **7** 498–505.

Margerison, H. R., Phillips, W. M., Stuart, F. M. and Sugden, D. E., 2005. Cosmogenic ^{3}He concentrations in ancient flood deposits from the Coombs Hills, northern Dry

Valleys, East Anarctica: interpreting exposure ages and erosion rates. *Earth and Planetary Science Letters.* **230** 163-175.

Mark, D. F., Barfod, D. Stuart, F. M., and Imlach, J., 2009. The ARGUS multicollector noble gas mass spectrometer: Performance for ^{40}Ar/^{39}Ar geochronology. *Geochemistry, Geophysics, Geosystems.* **10** (2) 1-9.

Marrocchi, Y., Burnard, P. G., Hamilton, D., Colin, A., Pujol, M., Zimmermann, L., and Marty, B., 2009. Neon isotopic measurements using high-resolution, multicollector noble gas mass spectrometer: HELIX-MC. *Geochemistry, Geophysics, Geosystems.* **10** (4): 1-8.

Masarik, J., 2002. Numerical simulation of in situ production of cosmogenic nuclides, *Geochim. Cosmochim. Acta* **66** A491.

Masarik, J., Kim, K.J., Reedy, R.C., 2007. Numerical simulations of in situ production of terrestrial cosmogenic nuclides. *Nuclear Instruments and Methods in Physics Research Section B* **259**, 642–645.

Masarik, J. and Beer, J., 2009. An updated simulation of particle fluxes and cosmogenic nuclide production in the Earth's atmosphere. *J. Geophys. Res.* **114** (D11): D11103.

Masarik, J. and Reedy, R. C., 1994. Effects of bulk composition on nuclide production processes in meteorites. *Geochimica Et Cosmochimica Acta* **58** (3): 5307-5317.

Masarik, J. and Reedy, R. C., 1995. Terrestrial cosmogenic-nuclide production systematics calculated from numerical simulations. *Earth and Planetary Science Letters* **136** 381-395.

Masarik, J. and Reedy, R. C., 1996. Monte Carlo simulation of in situ produced cosmogenic nuclides. *Radiocarbon* **38** 163-164.

Matsuda, J., Matsumoto, T., Sumino, H., Nagao, K., Yamamoto, J., Miura, Y., Kaneoka, I., Takahata, N., Sano, Y., 2002. The ^{3}He/^{4}He ratio of new internal He Standard of Japan (HESJ). *Geochemical Journal* **36** (2): 191-195.

McDougall, I. and Harrison, T. M., 1999. *Geochronology and Thermochronology by the ^{40}Ar/^{39}Ar Method*, Oxford: Oxford University Press, 269 pp.

Michel, R., Leya, I. and Borges, L., 1996. Production of cosmogenic nuclides in meteoroids: accelerator experiments and model calculations to decipher the cosmic ray record in extraterrestrial matter, *Nucl. Inst. Meth. Phys. Res.* B 113 434–444.

Min, K., Reiners, P. W., Wolff, J. A., Mundil, R., and Winters, R. L., 2006. (U-Th)/He dating of volcanic phenocrysts with high-U-Th inclusions, Jemez Volcanic Field, New Mexico. *Chemical Geology* **227** 223-225.

Nier, A. O., 1947. A mass spectrometer for isotope and gas analysis. *Rev. Sci. Instrum.* **11** 211-216.

Niedermann, S., 2002. Cosmic-ray-produced noble gases in terrestrial rocks: dating tools for surface processes, *Rev. Mineral. Geochem.* **47** 731–784.

Nishiizumi, K., Winterer, E. L., Kohl, C. P., Klein, J., Middleton, R., Lal, D. and Arnold, J. R., 1989. Cosmic ray production rates of ^{10}Be and ^{26}Al in quartz from glacially polished rocks, *J. Geophys. Res.* **94** 17907–17915.

Nishiizumi, K., Welten, K. C., Matsumura, H., Caffee, M., Ninomiya, K., Omoto, T., Nakagaki, R., Shima, T., Takahasi, N., Sekimoto, S., Yashima, H., Shibata, S., Bajo, K., Nagao, K., Kinoshita, N., Imamura, M., Sisteron, J. M., Shinohara, A., 2009. Measurements of high-energy neutron cross sections for accurate cosmogenic nuclide production rates. *Geochim. Cosmochim. Acta.* **73** A945.

Ozima, M. and Podosek, F. A., 2002. Noble gas geochemistry. 2nd edition, Cambridge University Press, Cambridge.

Phillips, F. M., Stone, W. D. and Fabryka-Martin, J. T., 2001. An improved approach to calculating low-energy cosmic-ray neutron fluxes near the land/atmosphere interface. *Chemical Geology* **175** 689-701.

Porcelli, D., Ballentine, C. J. and Wieler, R., 2002. An overview of noble gas geochemistry and cosmochemistry. *Rev. Mineral. Geochem.* **47** 1–20.

Powell, C. F., Fowler, P. H. and Perkins, D. H., 1959. The Study of Elementary Particles by the Photographic Method, London: Pergamon, 669 pp.

Reynolds, J. H., 1956. High sensitivity mass spectrometers for noble gas analysis. *Rev. Sci. Instrum.* **27** 928-934

Robinson, J.W., Skelly-Frame, E.M. and Frame, G.M. 2005. Undergraduate instrumental analysis. 6th Edition, Marcel Dekker, New York.

Sano, Y., Tokutake, T., and Takahata, N., 2008. Accurate measurement of atmospheric helium isotopes. *Analytical Sciences* **24** (4): 521-525.

Sano, Y., and Wakita, H., 1987. Precise measurement of helium isotopes in terrestrial gases. *Bull. Chem. Soc. Jpn.* **61,** 1153-1157.

Scarsi, P., 2000. Fractional extraction of helium by crushing of olivine and clinopyroxene phenocrysts: Effects on the ^{3}He/^{4}He measured ratio. *Geochimica et Cosmochimica Acta* **64** (21): 3751-3762.

Schäfer, J. M., Ivy-Ochs, S., Wieler, R., Leya, I., Baur, H., Denton, G. H., Schlüchter, C., 1999. Cosmogenic noble gas studies in the oldest landscape on earth: surface exposure ages of the Dry Valleys, Antarctica. *Earth and Planetary Science Letters* **167** 215-226.

Schimmelpfennig, I., Benedetti, L., Finkel, R. C., Pik, R., Blard, P. H., Bourle` s, D., Burnard, P. G. and Williams, A. J., 2009. Sources of in-situ ^{36}Cl in basaltic rocks. Implications for calibration of production rates. *Quat. Geochronology doi:10.1016/j.quageo.2009.1004.1003.*

Schuster, D.L., Farley, K. A., Sisteron, J. M., Burnett, D. S., 2003. Quantifying the diffusion kinetics and spatial distributions of radiogenic ^{4}He in minerals containing proton-induced ^{3}He. *Earth and Planetary Science Letters* **217** 19-32.

Serber, R., 1947. Nuclear reactions at high energies, *Phys. Rev.* **72** 1114–1115.

Simpson, J. A., 1983. Elemental and isotopic composition of Galactic cosmic rays. *Annual review of nuclear and particle sciences* **33** 323 - 382.

Sisteron, J. M., 2005. Cross-section measurements for proton- and neutron- induced reactions needed to understand cosmic-ray interactions on Earth and in space. In: R. C. Haight, M. B. Chadwick, T. Kawano and P. Talou, (Eds), *International Conference on Nuclear Data for Science and Technology* **769**, Santa Fe: AIP Conference Proceedings, 1596 - 1599.

Smart, D. F., Shea, M., A. and Flückiger, E., O., 2000. Magnetospheric models and trajectory computations. *Space Sci. Rev.* **93** 305–333.

Staudacher, T., Kurz, M. D. and Allègre, C. J., 1986. New noble-gas data on glass samples from Loihi seamount and Hualalai and on dunite samples from Loihi and Réunion Island. *Chemical Geology* **56** 193-205.

Stone, J., Evans, J., Fifield, K., Cresswell, R. and Allan, G., 1996a. Cosmogenic chlorine-36 production rates from calcium and potassium. *Radiocarbon* **38** 170–171.

Stone, J. O., Ballantyne, C. K., Fifield, L. K., 1998. Exposure dating and validation of periglacial weathering limits, NW Scotland. *Geology.* **26** 587-590.

Stone, J. O. H., Evans, J. M., Fifield, L. K., Allan, G. L. and Cresswell, R. G., 1998. Cosmogenic Chlorine-36 Production in Calcite by Muons. *Geochimica Et Cosmochimica Acta* **62** (3): 433-454.

Stone, J. O., 2000. Air pressure and cosmogenic isotope production, *J. Geophys. Res.* **105** 23753–23759.

Stone, J. O., 2005. Terrestrial chlorine-36 production from spallation of iron. In: *Abstract of 10th international Conference on Accelerator Mass Spectrometry, Berkley, California, USA.*

Stuart, F. M., Burnard, P. G., Taylor, R. P. and Turner, G., 1995. Resolving mantle and crustal contributions to ancient hydrothermal fluids: He—Ar isotopes in fluid inclusions from Dae Hwa W—Mo mineralisation, South Korea. *Geochimica et Cosmochimica Acta* **59** (22): 4663-4673.

Stuart, F. M., Lass-Evans, S., Fitton, J. G. and Ellam, R. M., 2003. High ^{3}He/^{4}He ratios in picritic basalts from Baffin Island and the role of a mixed reservoir in mantle plumes. *Nature* **424** (6944): 57-59.

Swanson, T. W. and Caffee, M., 2001. Determination of ^{36}Cl production rates derived from the well-dated deglaciation surfaces of Whidbey and Fidalgo Islands, Washington, *Quat. Research* **56** 366–382.

Takaoka, N., 1976. A low-blank, metal system for rare-gas analysis. *Mass Spectroscopy* **24** (1): 73-86.

Thompson, R. N., Esson, J. and Dunham, A. C., 1972. Major element chemical variation in the Eocene lavas of the Isle of Skye, Scotland. *Journal of Petrology* **13** part 2, 219-253.

Trull, T. W., Kurz, M. D. and Jenkins, W. J., 1991. Diffusion of cosmogenic ^{3}He in olivine and quartz: implications for surface exposure dating, *Earth and Planetary Science Letters* **103** 241–256.

Usoskin, I. G., Alanko-Huotari, K., Kovaltsov, G. A. and Mursula, K., 2005. Heliosphericmodulation of cosmic rays: Monthly reconstruction for 1951–2004, *J. Geophys. Res.* **110** A12108.

Vermeesch, P., 2007. CosmoCalc: an excel add-in for cosmogenic nuclide calculations. *Geochemistry, Geophysics, Geosystems* **8** 1525-2027.

Vermeesch, P., Heber, V., Strasky, S., Kober, F., Schaefer, J. M., Baur, H., Schlüchter, C. and Wieler, R., 2008. Cosmogenic ^{3}He and ^{21}Ne measured in artificial quartz targets after one year of exposure in the Swiss Alps, *Geophys. Res. Abstr.* **10** 1607–7962/gra/EGU2008-A-08431.

Wiedenbeck, M. E., Davis, A. J., Leske, R. A., Binns, W. R., Cohen, C. M. S., Cummings, A. C., de Nolfo, G., Israel, M. H., Labrador, A. W., Mewaldt, R. A., Scott, L. M., Stone, E.C. and von Rosenvinge, T. T., 2005. The level of solar modulation of galactic cosmic rays from 1997 to 2005 as derived from ACE measurements of elemental energy spectra, Proceedings of the 29th International Cosmic Ray Conference, Prune, India, 03–10 August, 2005 2 Mumbai: Tata Institute of Fundamental Research, 277–280.

Wieler, R., 2002. Cosmic-ray-produced noble gases in meteorites. *Reviews in Mineralogy and Geochemistry* **47** 125–170.

Williams, A. J., Stuart, F. M., Day, S. J. and Phillips, W. M., 2005. Using pyroxene microphenocrysts to determine cosmogenic ^{3}He concentrations in old volcanic rocks: an example of landscape development in central Gran Canaria. *Quaternary Science Reviews* **24** 211-222.

Ziegler, J. F., Biersack, J. P. and Ziegler, M. D., 2008. *SRIM Stopping Ranges of Ions in Matter*, Morrisville: Lulu Press, 398 pp.

Zimmerman, L., Blard, P-H., Burnard, P., Medynski, S., Pik, R. and Puchol, N., 2012. A new single vacuum furnace design for cosmogenic ^{3}He dating. *Geostandards and Geoanalytical Research* **36** No. 2, 121-129.

Zreda, M.G., Phillips, F.M., Elmore, D., Kubik, P.W., Sharma, P., Dorn, R.I., 1991. Cosmogenic chlorine-36 production rates in terrestrial rocks. *Earth and Planetary Science Letters* **105**, 94–109.